REPORT DOCUMENTATION PAGE

1a. REPORT SECURITY CLASSIFICATION UNCLASSIFIED	1b. RESTRICTIVE MARKINGS None
2a. SECURITY CLASSIFICATION AUTHORITY	3. DISTRIBUTION/AVAILABILITY OF REPORT Approved for Public Release; Distribution Unlimited.
2b. DECLASSIFICATION/DOWNGRADING SCHEDULE	

4. PERFORMING ORGANIZATION REPORT NUMBER(S) MIT Gas Turbine Laboratory Report No.	5. MONITORING ORGANIZATION REPORT NUMBER(S) AFOSR-TR- 84-0859

6a. NAME OF PERFORMING ORGANIZATION MASSACHUSETTS INSTITUTE OF TECHNOLOGY	6b. OFFICE SYMBOL (If applicable) 31-264	7a. NAME OF MONITORING ORGANIZATION See #8
6c. ADDRESS (City, State and ZIP Code) DEPARTMENT OF AERONAUTICS & ASTRONAUTICS Cambridge, Massachusetts 02139		7b. ADDRESS (City, State and ZIP Code) See #8

8a. NAME OF FUNDING/SPONSORING ORGANIZATION AIR FORCE OFFICE OF SCIENTIFIC RESEARCH	8b. OFFICE SYMBOL (If applicable) AFOSR/NA	9. PROCUREMENT INSTRUMENT IDENTIFICATION NUMBER Contract No. F49620-82-K-0002

8c. ADDRESS (City, State and ZIP Code) AFOSR /NA Bolling Air Force Base, D.C. 20332	10. SOURCE OF FUNDING NOS.			
	PROGRAM ELEMENT NO. 61102F	PROJECT NO. 2307	TASK NO. A4	WORK UNIT NO.

11. TITLE (Include Security Classification) Current Problems in Turbomachinery Fluid Dynamics (UNCLASSIFIED)

12. PERSONAL AUTHOR(S) E.M. Greitzer, J.L. Kerrebrock, W.T. Thompkins, Jr., J.E. McCune, A.H. Epstein, W.R. Hawthorne, C.S. Tan

13a. TYPE OF REPORT Semi-annual Report	13b. TIME COVERED FROM 11/1/83 TO 4/30/84	14. DATE OF REPORT (Yr., Mo., Day) 7/16/84	15. PAGE COUNT 102

16. SUPPLEMENTARY NOTATION

17. COSATI CODES			18. SUBJECT TERMS (Continue on reverse if necessary and identify by block number)
FIELD	GROUP	SUB. GR.	Transonic Compressors, Compressor Stability, Casing Treatment, Inlet Vortex, Design, Heavily Loaded Compressors

19. ABSTRACT (Continue on reverse if necessary and identify by block number)

A multi-investigator program on problems of current interest in turbomachinery fluid dynamics is being conducted at the MIT Gas Turbine and Plasma Dynamics Lab. Within the scope of this effort, four different tasks, encompassing both design and off-design problems, have been identified. These are: 1)Investigation of fan and compressor design point fluid dynamics (including formation of design procedures using current three-dimensional transonic codes and development of advanced measurement techniques for use in transonic fans); 2)Studies of basic mechanisms of compressor stability enhancement using compressor casing/hub treatment; 3)Fluid mechanics of inlet vortex flow distortions in gas turbine engines; 4)Investigations of three-dimensional analytical and numerical computations of flows in highly loaded turbomachinery blading. In addition to these tasks, this multi-investigator effort also includes the Air Force Research in Aero Propulsion Technology (AFRAPT) Program. This document describes work carried out on this contract during the period 11/1/83 - 4/30/84.

20. DISTRIBUTION/AVAILABILITY OF ABSTRACT UNCLASSIFIED/UNLIMITED ☒ SAME AS RPT. ☐ DTIC USERS ☐	21. ABSTRACT SECURITY CLASSIFICATION UNCLASSIFIED	
22a. NAME OF RESPONSIBLE INDIVIDUAL James D Wilson	22b. TELEPHONE NUMBER (Include Area Code) 202/767-4935	22c. OFFICE SYMBOL AFOSR/NA

DD FORM 1473, 83 APR   EDITION OF 1 JAN 73 IS OBSOLETE.

GAS TURBINE AND PLASMA DYNAMICS LABORATORY
DEPARTMENT OF AERONAUTICS AND ASTRONAUTICS
MASSACHUSETTS INSTITUTE OF TECHNOLOGY
CAMBRIDGE, MA 02139

SEMI-ANNUAL REPORT

on

CONTRACT NO. F49620-82-K-0002

entitled

CURRENT PROBLEMS IN TURBOMACHINERY FLUID DYNAMICS

for the period

November 1, 1983 to April 30, 1984

submitted to

AIR FORCE OFFICE OF SCIENTIFIC RESEARCH

Attention: Major Michael S. Francis, Program Manager
      Directorate of Aerospace Sciences, AFOSR (AFSC)
      Bolling Air Force Base, DC 20332

Principal
Investigators: Edward M. Greitzer
      Jack L. Kerrebrock
      William T. Thompkins, Jr.
      James E. McCune

Co-Investigators: Alan H. Epstein
      Choon S. Tan

Collaborating
Investigators: Eugene E. Covert
      Sir William R. Hawthorne
      Wai K. Cheng
      Hyoun-Woo Shin
      Robert Haimes

June 1984

Accession For	
NTIS GRA&I	☒
DTIC TAB	☐
Unannounced	☐
Justification	
By	
Distribution/	
Availability Codes	
Dist	Avail and/or Special
A/1	

TABLE OF CONTENTS

1. INTRODUCTION AND RESEARCH OBJECTIVES

This report describes work carried out at the Gas Turbine and Plasma Dynamics Laboratory at MIT, as part of our multi-investigator effort on current problems in turbomachinery fluid dynamics. Support for this program is provided by the Air Force Office of Scientific Research under Contract Number F49620-82-K-0002, Major M.S. Francis and Dr. J. D. Wilson, Program Managers.

The present report gives a summary of the work for the period 11/1/83 - 4/30/84. For further details and background, the referenced reports, publications and previous reports (covering the period 10/1/79 - 5/31/83)[1,2,3,4] should be consulted.

Within the general topic, four separate tasks are specified. These have been described in detail in Reference 1, but they are, in brief:

1. Investigation of fan and compressor design point fluid dynamics,

2. Studies of compressor stability enhancements,

3. Fluid mechanics of gas turbine operation in inlet flow distortion,

4. Investigations of three-dimensional flows in highly loaded turbomachines.

In addition to these tasks, the multi-investigator contract also encompasses the Air Force Research in Aero Propulsion Technology program. The work carried out in each of the tasks will be described in the next section.

References

1. E.M. Greitzer, et al., AFOSR TR-82-0027, Final Report, 10/79 - 9/81, on "Current Problems in Turbomachinery Fluid Dynamics."

2. E.M. Greitzer, et al., Annual Report, 10/1/81 - 11/30/82, on "Current Problems in Turbomachinery Fluid Dynamics."

3. E.M. Greitzer, et al., Semi-Annual Report 12/1/82 - 5/31/83, on "Current Problems in Turbomachinery Fluid Dynamics."

4. E.M. Greitzer, et al., Annual Report, 12/1/82 - 10/31/83, on "Current Problems in Turbomachinery Fluid Dynamics."

TASK I: INVESTIGATION OF FAN AND COMPRESSOR DESIGN POINT FLUID DYNAMICS

TASK IA: INVERSE DESIGN TASK

During the last three years, efforts on the inverse design project
have been directed to finding an acceptable inverse method which was appli-
cable to the full Mach number range encountered in high speed axial
compressors. We have found one method, based on time marching solutions to
the Euler equations, which is accurate enough and could potentially be
extended to three dimensional geometries, see references [1.1], [1.2],
[1.3], [1.4]. This method operates in a mixed mode format in which either
blade pressure distributions or geometric constraints are specified. The
method is unfortunately far too slow, in terms of computer time usage, for
practical design work and in its present form does not properly adjust
solid wall positions in subsonic flow regions.

Work on the time marching like method is now considered complete with
the publication of a Ph.D. thesis on the method by Tong. This thesis
contains new information about sources of numerical errors in finite
difference solutions and artificial smoothing operators, a demonstration
that the simple inverse scheme would work in supersonic flow but not in
mixed subsonic-supersonic flows, and a survey and evaluation of existing
inverse and design methods.

A new direct or inverse method is now being developed which is many
times faster than the old time marching scheme, is easily coupled to
boundary layer solvers and is more accurate than the time marching style
solver. This new method appears to retain all the traditional advantages
of streamline curvature schemes while being useful for subsonic, supersonic,

transonic, and shocked flows. The scheme can be described as a conserva-tive finite volume scheme in streamline coordinates and has been applied to supersonic duct flows, subsonic and transonic duct flows, subsonic cascade flows, and viscous-inviscid interactions.

An AIAA paper, number 84-1643, was presented at the June 1984 Fluids meeting in Snowmass, CO. This paper presents theory, relaxation methods, and test examples for the inviscid applications. This paper is reproduced as Appendix 1. A paper on the viscous-invicid interaction aspects of the work has been accepted for the Third Symposium on Numerical and Physical Aspects of Aerodynamic Flows in Jan. 1985 at Long Beach, CA. An internal memo which shows the present state of the coupling work is included as Appendix 2.

AIAA'84

AIAA-84-1643
Conservative Streamtube Solution
of Steady-State Euler Equations
M. Drela, M. Giles and
W. T. Thompkins, Jr.,
Massachusetts Institute of
Technology, Cambridge, MA

AIAA 17th Fluid Dynamics, Plasma Dynamics, and Lasers Conference

June 25-27, 1984/Snowmass, Colorado

CONSERVATIVE STREAMTUBE SOLUTION OF STEADY-STATE EULER EQUATIONS

Mark Drela[*]
Massachusetts Institute of Technology
Cambridge, Massachusetts

Michael Giles[#]
Massachusetts Institute of Technology
Cambridge, Massachusetts

W. T. Thompkins, Jr.[@]
Massachusetts Institute of Technology
Cambridge, Massachusetts

Abstract

This paper presents a new method for solving the steady state Euler equations. The method is similar to streamline curvature methods but has a conservative finite volume formulation which ensures correct shock capturing. Either wall position or wall pressure may be prescribed as boundary conditions, permitting both direct and inverse calculations. In supersonic applications the solution is obtained by space-marching while in subsonic and transonic applications iterative relaxation methods are used. Numerical results are given for:

a) Supersonic diffuser with oblique shocks (Direct calculation)
b) Supersonic jet entering still reservoir (Inverse calculation)
c) Subsonic bump in a channel with 25% blockage (Direct and inverse)
d) Subsonic high-work turbine cascade (Direct)
e) Transonic bump in a channel with 12% blockage (Direct calculation)

Introduction

At present most methods for the numerical calculation of steady-state transonic solutions of the Euler equations are based upon a conservative finite volume approximation to the unsteady equations of motion [1]. This approach is conceptually straightforward since the unsteady equations are hyperbolic in time and so the same numerical procedure can be used in regions where the flow is locally subsonic or supersonic. Using a conservative finite volume formulation also guarantees the correct Rankine-Hugoniot shock jump relations regardless of the details of the shock calculation.

The principal disadvantage of this approach is that the convergence rate is limited by the relatively slow propagation of wavelike disturbances throughout the domain and their reflection at the boundaries of the computational domain. Current methods try to overcome this limitation by a variety of acceleration methods such as variable time steps, implicit operators with larger time steps, and multigrid with larger time steps on coarser grids, but computation times remain an order-of-magnitude larger than for the solution of the steady-state

[*]Research Assistant, Dept. of Aero and Astro

[#]Research Assistant, Dept. of Aero and Astro
 Student Member AIAA

[@]Associate Professor, Dept. of Aero and Astro
 Member AIAA

transonic full potential equation.

An older approach to solving the subsonic Euler equations is the streamline curvature method which can be considered to be an iterative relaxation solution to the equations of motion in intrinsic coordinates [2,3,4]. In one version [2] an initial set of streamlines is guessed and the steady-state normal momentum equation is integrated in the normal direction assuming known enthalpy and entropy variation along each streamtube. The resulting error in the continuity equation then drives a relaxation procedure to move streamlines towards their correct positions. Because it is based upon the steady state equations, the relaxation procedure in the hyperbolic supersonic region must be different from that in the elliptic subsonic region.

One main advantage of the streamline curvature method is that it is much faster than time-marching methods, and this makes it much more suitable for design applications in which many different geometries need to be analyzed. A secondary advantage is the simple inviscid treatment of adjacent streamtubes with differing stagnation properties. In time-marching calculations numerical dissipation smears the discontinuities.

The major disadvantages of the standard streamline curvature method are that the iterative solvers are unstable in the supersonic regions, and they do not conserve momentum globally, so that for example the lift on an airfoil may not equal the change in momentum of the fluid. In subsonic cases this momentum loss may be small, but in transonic cases there may be an appreciable momentum loss at the shock. Studies by Salas et al [5] of solutions to the full potential equation show that momentum loss even at relatively weak shocks can produce large errors in shock position.

The method we have developed is similar to the streamline curvature method, but has a conservative finite volume formulation which ensures the correct treatment of shocks. Like the streamline curvature method it solves the steady-state equations and so requires different solvers or solution algorithms for purely supersonic, purely subsonic or transonic problems. The supersonic solver marches in streamwise steps downstream from a known inlet flow. The subsonic solver starts from a guessed set of streamline positions, solves each streamtube problem as a separate quasi 1-D problem, and then relaxes all the streamline positions to satisfy pressure continuity across streamlines. The transonic solver is similar to the subsonic solver but requires numerical dissipation in the supersonic region, and

relaxes one streamline at a time instead of all simultaneously. At the present time the supersonic and subsonic solvers are both robust and very fast, but the transonic solver requires further improvement in calculation times.

Finite Volume Formulation for Euler Equations

The governing equations are derived from the integral form of the mass, momentum, and energy conservation laws.

$$\oint \vec{q} \cdot \vec{n} \, d\ell = 0 \tag{1a}$$

$$\oint \rho(\vec{q} \cdot \vec{n})\vec{q} + p\vec{n} \, d\ell = 0 \tag{1b}$$

$$\oint \rho(\vec{q} \cdot \vec{n})H_o \, d\ell = 0 \tag{1c}$$

where the integration is round a closed curve.

These conservation equations are applied to streamtube conservation cells which have the property that there is no convection across cell faces aligned with the flow (Figure 1). Density ρ and speed q are defined to be the average values on the faces at the two ends of the conservation cell. Also, the pressure in the cell is assumed to be linear and defined by the average values on the four faces. For clarity, the average pressures on the end faces are denoted by p, and on the streamline faces by Π.
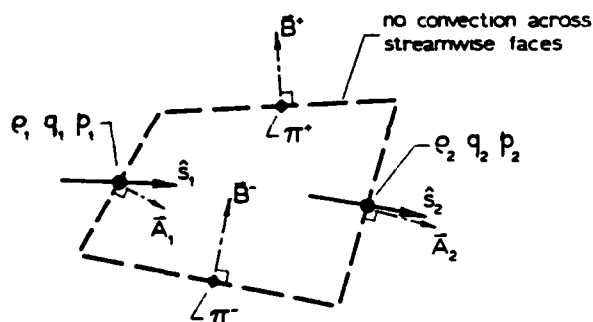

Figure 1. Typical conservation cell

The flow direction at the end faces is given by the unit vector $\hat{s}$ which is defined by the local geometry. The definition of $\hat{s}$ in terms of the local cell node positions will be given later. The vectors $\vec{A}$ and $\vec{B}$ in Figure 1 are the cell face area normal vectors.

With the simplification that there is no convection across the streamline faces, the discrete conservation equations for mass and momentum are:

$$\rho_1 q_1 \hat{s}_1 \cdot \vec{A}_1 = \rho_2 q_2 \hat{s}_2 \cdot \vec{A}_2 \tag{2a}$$

$$p_1 \vec{A}_1 + (\rho_1 q_1 \hat{s}_1 \cdot \vec{A}_1)q_1 \hat{s}_1 + \Pi^- \vec{B}^- =$$
$$p_2 \vec{A}_2 + (\rho_2 q_2 \hat{s}_2 \cdot \vec{A}_2)q_2 \hat{s}_2 + \Pi^+ \vec{B}^+ \tag{2b}$$

Since the mass flux is constant along the streamtube, the enthalpy conservation equation reduces to the simple statement that total enthalpy is constant along a streamtube.

$$\frac{\gamma}{\gamma-1} \frac{p_1}{\rho_1} + \frac{1}{2} q_1^2 = \frac{\gamma}{\gamma-1} \frac{p_2}{\rho_2} + \frac{1}{2} q_2^2 \tag{2c}$$

From the earlier assumption that the pressure is linear over the cell, it follows that the average pressures on the cell faces must be related by

$$p_1 + p_2 = \Pi^+ + \Pi^- \tag{2d}$$

The assumption of no convection across the streamline cell faces means that the grid is not known a priori. The grid geometry must then be treated as an unknown which is determined as part of the solution. This is a novel feature for a finite volume scheme, although it has long been used in streamline curvature schemes. This feature also makes the inverse and direct problems operationally equivalent. In the direct problem, a fixed wall position is imposed as a boundary condition and the wall pressure is obtained as a result. In the inverse problem, the wall pressure is prescribed as the boundary condition and the geometry is calculated as the result. Examples of both types of calculations will be given later.
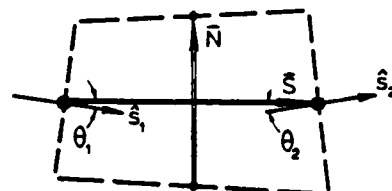

Figure 2. Geometry definitions for streamline curvature equations

The momentum equation (2b), which is a vector equation, will now be shown to reduce to the set of streamwise and normal momentum equations used by the streamline curvature methods, provided our coordinates, like the s-n coordinates, are orthogonal. More precisely, the vectors $\vec{S}$ and $\vec{N}$ joining the cell midpoints in Figure 2 must become perpendicular and the angles θ_1 and θ_2, between $\vec{S}$ and $\hat{s}_1$ and $\hat{s}_2$ respectively, must vanish as the grid is refined. By taking the dot product of (2b) in turn with $\vec{S}$ and $\vec{N}$ and using (2d), we obtain the following streamwise and normal momentum equations,

$$\rho_2 q_2^2 (\hat{s}_2 \cdot \vec{A}_2)(\hat{s}_2 \cdot \vec{S}) - \rho_1 q_1^2 (\hat{s}_1 \cdot \vec{A}_1)(\hat{s}_1 \cdot \vec{S}) =$$
$$- |\vec{N} \times \vec{S}| (p_2 - p_1) \tag{3a}$$

$$\rho_2 q_2^2 (\hat{s}_2 \cdot \vec{A}_2)(\hat{s}_2 \cdot \vec{N}) - \rho_1 q_1^2 (\hat{s}_1 \cdot \vec{A}_1)(\hat{s}_1 \cdot \vec{N}) =$$
$$- |\vec{N} \times \vec{S}| (\Pi^+ - \Pi^-) \tag{3b}$$

Now define $m = \rho_1 q_1 (\hat{s}_1 \cdot \vec{A}_1) = \rho_2 q_2 (\hat{s}_2 \cdot \vec{A}_2)$. With the condition that $\vec{S}$ and $\vec{N}$ are orthogonal, and with the small angle approximations $\sin \theta = \theta$ and $\cos \theta \approx 1$, equations (3a) and (3b) reduce to

$$\frac{m}{|N|} \frac{q_2 - q_1}{|S|} = - \frac{p_2 - p_1}{|S|} \tag{4a}$$

$$\frac{mq}{|N|} \frac{\theta_2 - \theta_1}{|S|} = - \frac{\Pi^+ - \Pi^-}{|N|} \qquad (4b)$$

In the limit as the grid is defined, these finite difference equations become the streamline curvature equations

$$\rho q \frac{\partial q}{\partial s} = - \frac{\partial p}{\partial s} \qquad (5a)$$

$$\rho q^2 \frac{\partial \theta}{\partial s} = - \frac{\partial p}{\partial n} \qquad (5b)$$

Thus our equations can be interpreted as discrete representations of the streamline curvature equations. The essential point however is that our conservation form ensures that shocks will be correctly captured. Since equation (2d) was necessary to obtain the above result, it is interpreted as a consistency condition on our finite volume equations.

Solution Procedure for Supersonic Flow

For flow which is known to be supersonic everywhere, a simple space-marching solution procedure may be used which takes full advantage of the hyperbolic character of the steady state equations. In this solver the unknown geometry variables x,y are located at the nodes of the conservation cell as shown in Figure 3a. The $\hat{s}$ unit vector giving the local flow direction is defined to be tangent to the circular arc passing through the three upstream midpoints as illustrated in Figure 3b. This definition was chosen so that $\hat{s}$ depends solely on upstream information, which is the correct domain of dependence for supersonic flow and allows a space-marching solution procedure.
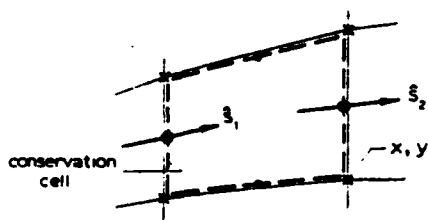

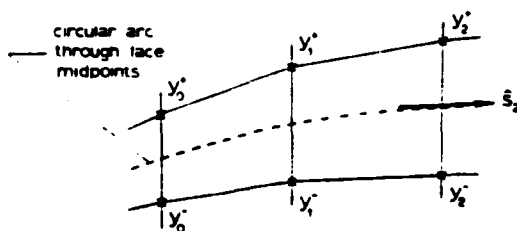Figure 3a. Geometry variable locations for supersonic solver

Figure 3b. $\hat{s}$ definition for supersonic solver

Since the streamwise position of the normal grid lines is arbitrary, some constraint on this streamwise position must be imposed. At present, the supersonic solver fixes the x positions for simplicity, leaving only the y's as geometric unknowns. A more general grid structure will be treated in the subsonic solver section.

At the inlet boundary all the variables are specified. At the top and bottom boundaries one boundary condition is specified. This boundary condition can be either a specified wall position (direct case) or a specified pressure (inverse case). With these prescribed boundary conditions the solver marches downstream from the inlet, solving all of the equations at each streamwise station by using an aprroximate Newton-Raphson linearization of the equations. This procedure is similar to Keller's Box Scheme [6] for the solution of the boundary layer equations.

To reduce the number of unknowns, ρ_2 and p_2 are eliminated using the enthalpy equation (2c) and the pressure relation (2d). With these substitutions the equations for mass and momentum conservation are,

Mass

$$R_m \equiv \frac{\gamma q_2 s_{2_x} (y_2^+ - y_2^-)(\Pi^+ + \Pi^- - p_1)}{(\gamma - 1)(H_o - q_2^2/2)} - m = 0 \qquad (6$$

x-momentum

$$R_x \equiv m(q_1 s_{1_x} - q_2 s_{2_x}) + p_1(y_1^+ - y_1^- + y_2^+ - y_2^-) +$$
$$\Pi^+(y_2^- - y_1^+) + \Pi^-(y_1^- - y_2^+) = 0 \qquad (6b)$$

y-momentum

$$R_y \equiv m(q_1 s_{1_y} - q_2 s_{2_y}) + (\Pi^- - \Pi^+)(x_2 - x_1) = 0 \qquad (6c)$$

In these equations m is the mass flux which is constant for a given streamtube. s_x and s_y are the components of the $\hat{s}$ vector. The equations are linearized to calculate the corrections needed to drive the residuals to zero.

Mass

$$\frac{\partial R_m}{\partial q_2} \delta q_2 + \frac{\partial R_m}{\partial \Pi^-} \delta \Pi^- + \frac{\partial R_m}{\partial \Pi^+} \delta \Pi^+$$
$$+ \frac{\partial R_m}{\partial y_2^-} \delta y_2^- + \frac{\partial R_m}{\partial y_2^+} \delta y_2^+ = - R_m \qquad (7a)$$

x-momentum

$$\frac{\partial R_x}{\partial q_2} \delta q_2 + \frac{\partial R_x}{\partial \Pi^-} \delta \Pi^- + \frac{\partial R_x}{\partial \Pi^+} \delta \Pi^+$$
$$+ \frac{\partial R_x}{\partial y_2^-} \delta y_2^- + \frac{\partial R_x}{\partial y_2^+} \delta y_2^+ = - R_x \qquad (7b)$$

y-momentum

$$\frac{\partial R_y}{\partial q_2} \delta q_2 + \frac{\partial R_y}{\partial \Pi^-} \delta \Pi^- + \frac{\partial R_y}{\partial \Pi^+} \delta \Pi^+$$

$$+ \frac{\partial R_y}{\partial y_2^-} \delta y_2^- + \frac{\partial R_y}{\partial y_2^+} \delta y_2^+ = - R_y \qquad (7c)$$

Equations (7a-c) for each streamtube cell are assembled in a 3x3 block tridiagonal form together with the two boundary conditions, and are solved by standard methods. Because the equations are fully linearized, this Newton-Raphson procedure requires only three or four iterations at each streamwise station to converge machine accuracy. ρ_2 and p_2 can then be calculated from the enthalpy and energy equations.

Figure 4 shows the final streamline grid and Mach number contour plot for a supersonic channel. The inlet flow is uniform and fixed geometry is specified on the top and bottom walls. The agreement with the exact shock and expansion fan positions is excellent. The shock has been correctly captured without the addition of any artificial dissipation.
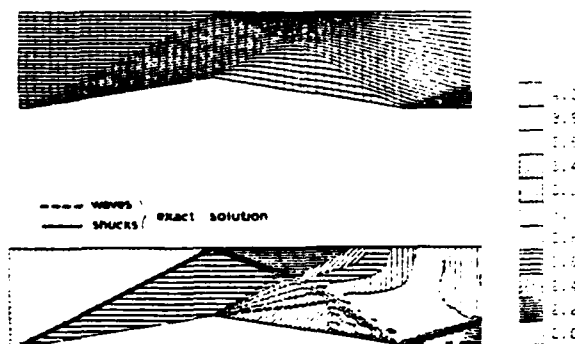

Figure 4. Final grid and Mach number contours for supersonic channel

Figure 5 shows the calculation of a 2-D supersonic jet entering a stagnant reservoir filled with a gas of higher static pressure. Before entering the reservoir the flow is parallel with specified top and bottom wall positions. After entering the reservoir the top and bottom streamlines have constant specified pressure. This case physically corresponds to the Mach diamond pattern produced by an overexpanded supersonic nozzle exhausting into a still atmosphere. Both the direct and the inverse calculations each used only 10 CPU seconds on a DEC PDP 11/70 computer.

Solution Procedure for Subsonic Flow

In subsonic flow, the steady state conservation equations are elliptic, since pressure signals can propagate both upstream and downstream. The space-marching solution procedure used in the supersonic
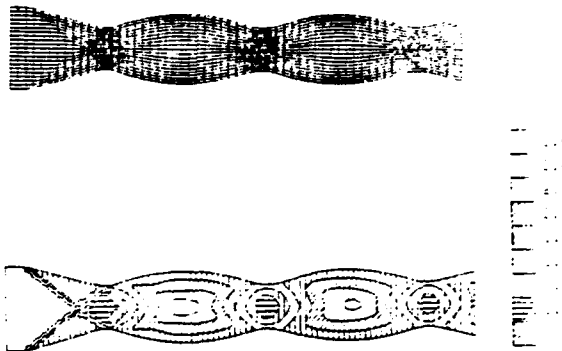

Figure 5. Final grid and Mach number contours for supersonic jet

solver cannot properly represent the downstream influence, and hence an iterative relaxation procedure, very similar to some streamline curvature solvers, is used in the subsonic solver. The conservation cell and $\hat{s}$ definitions are also different than those used in the supersonic solver. As shown in Figure 6, each conservation cell node is defined to be at the midpoint of a streamline segment. The $\hat{s}$ unit vector lies along the line connecting the midpoints of adjacent normal line segments. The boundary conditions are specified stagnation pressure, total enthalpy and flow angle at the inlet, and specified pressure and node position at the exit. This last condition is required to determine the fraction of the total mass flux which is in each streamtube.
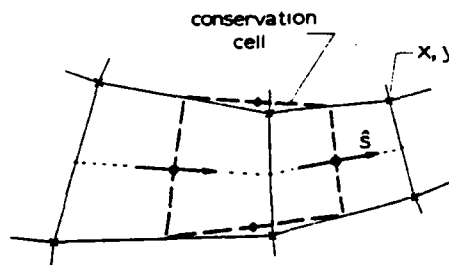
Figure 6. Geometry variable locations and $\hat{s}$ definition for subsonic solver

In the iterative relaxation procedure, an initial set of streamline positions is first chosen. Then each streamtube is treated separately as a quasi-1D problem with equations (2a), (2c), and (3a) being solved simultaneously at each streamwise station using a Newton-Raphson technique incorporating the boundary conditions. Equations (2d) and (3b) are then used to calculate the pressures Π^+, Π^- on the upper and lower surfaces of each streamtube. In the converged steady state these must match the corresponding pressures from neighboring streamtubes so the pressure jump $\Delta\Pi$ across each streamline is used to drive a relaxation of the streamline positions.

The approximate relationship between changes in the streamline positions and changes in the Π values

is obtained from the linearized isentropic pressure-area relation and the pressure-curvature relation.

$$\tilde{P}_1 = \frac{\gamma p}{A} \frac{M^2}{1-M^2} \tilde{A}_1 , \qquad \tilde{P}_2 = \frac{\gamma p}{A} \frac{\cdot^2}{1-M^2} \tilde{A}_2 \qquad (8a\text{-}b)$$

$$\tilde{\Pi}^+ - \tilde{\Pi}^- = -\rho q^2 \tilde{\kappa} = -\gamma p M^2 \tilde{\kappa} \qquad (9)$$

In these equations $\tilde{p}, \tilde{A}, \tilde{\Pi}, \tilde{\kappa}$ are the small changes in pressure, cross-sectional area, streamline pressure and curvature, and M is the local Mach number. After substituting the dependence of A and $\tilde{\kappa}$ on the changes in coordinate positions $\tilde{y}$ we find the equation for the $\tilde{y}$ required to eliminate the pressure mismatch $\Delta\Pi$ across the streamlines to be,

$$\left\{ (1-M^2) u_n^2 \delta_s^2 + u_s^2 \delta_n^2 \right\} \tilde{y} = -\frac{A}{\gamma p M^2} \Delta\Pi \qquad (10)$$

u_s^2 and δ_s^2 are difference operators defined by

$$u_s^2 \tilde{y}_{i,j} = (\tilde{y}_{i-1,j} + 2\tilde{y}_{i,j} + \tilde{y}_{i+1,j})/4 \qquad (11)$$

$$\delta_s^2 \tilde{y}_{i,j} = (\tilde{y}_{i-1,j} - 2\tilde{y}_{i,j} + \tilde{y}_{i+1,j})/\Delta s^2 \qquad (12)$$

u_n^2 and δ_n^2 are similarly defined operators in the normal direction. Equation (10) is similar to the streamline curvature relaxation method used by Keith et al [2], and the iterative equation in the solution of the potential equation [5]. The boundary conditions required for equation (10) are $\tilde{y}=0$ on the walls and at the exit, and $\delta_n\tilde{y}=0$ at the inlet. The latter corresponds to a fixed inlet flow angle. Equation (10) is solved using a standard SLOR technique, the streamline positions are updated with $\tilde{y}$, and the cycle repeated until $\tilde{y}$ and $\Delta\Pi$ become acceptably small. This SLOR relaxation technique limits the overall spectral radius of the scheme to $1-0(\Delta x^2, \Delta y^2)$.

A test example is a duct with a 25% blockage bump. The exit Mach number is approximately 0.45 with a maximum Mach number in the throat of approximately 0.87. Figure 7a shows the final streamline grid and Mach number contour plot. Because the equations are second-order accurate and no numerical dissipation has been needed to maintain stability, the stagnation pressure loss error is very small (Figure 7b). The observed terminal spectral radius for this 40x30 case was 0.96.

This test case has also been used to check the capabilities of the solver in its inverse mode. The pressure on the lower wall was set equal to the pressure computed by the direct method, and the initial grid was chosen to be the rectangular duct without the bump. In approximately the same number of iterations as the direct case, the streamlines and flow variables converged (to within machine roundoff) to the values computed by the direct method.

In the case above, the normal grid lines were held at fixed x values as in the supersonic case. Obviously, this is not adequate for duct flows with large turning angles or with airfoils with blunt leading edges. For the turbine cascade case shown in Figure 8 a more suitable constraint on the normal grid lines was used. During the streamline relaxation step, the nodes are moved parallel
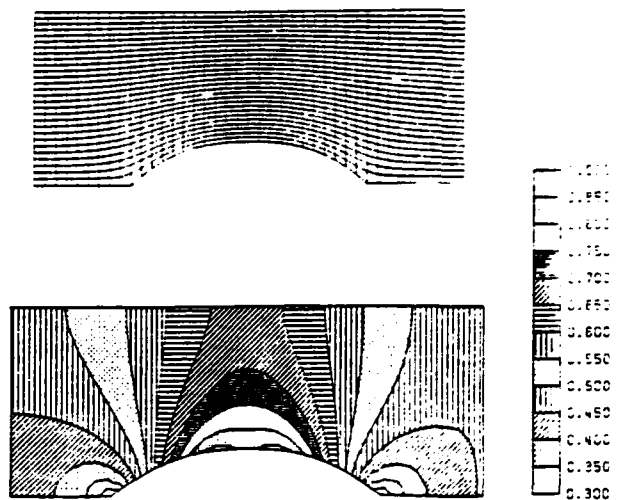

Figure 7a. Final grid and Mach number contours for subsonic bump
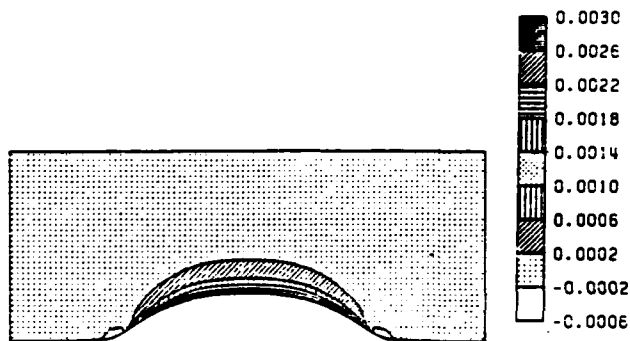

Figure 7b. Relative stagnation pressure loss for subsonic bump

to the local normal lines. Then the nodes are moved along the streamlines by an algorithm which minimizes the local shearing of the grid and variations in streamwise resolution. The Kutta condition is imposed by shifting the entire exit plane vertically until the values of Π on either side of the trailing edge are equal.

All the cases shown above have either hardwall (prescribed geometry) or freewall (prescribed pressure) boundary conditions. With our scheme, it is also possible to prescribe a "softwall" boundary condition where the wall is allowed to deform under the effect of the wall pressure according to some prescribed relationship. Because the displacement surface of a boundary layer can be described in this manner, the softwall boundary condition makes efficient and straightforward boundary layer coupling possible even in strongly coupled cases with separation bubbles. The details and numerical examples of the coupling between this Euler solver and a compressible boundary layer code [7] will be presented in a future paper.

Transonic Solver

The transonic solver is still under development. Currently it is not fast as the subsonic solver, but future planned changes, including multigrid, should greatly increase its speed. The conservation cell

$$\mu > \max\left(0, \frac{1}{\gamma+1} \frac{M^2 - 1}{M^2}\right) \tag{15}$$

The iterative solution procedure is to guess an initial streamline grid and then sweep up and down in the normal direction, relaxing each streamline by assuming neighboring streamlines are fixed and so solving the steady state equations for the two streamtubes on either side of the streamline using a Newton-Raphson procedure. Figure 9a shows the final grid and Mach number contour plot for a partially choked duct with a 12% blockage bump. Figure 9b gives the relative stagnation pressure losses.
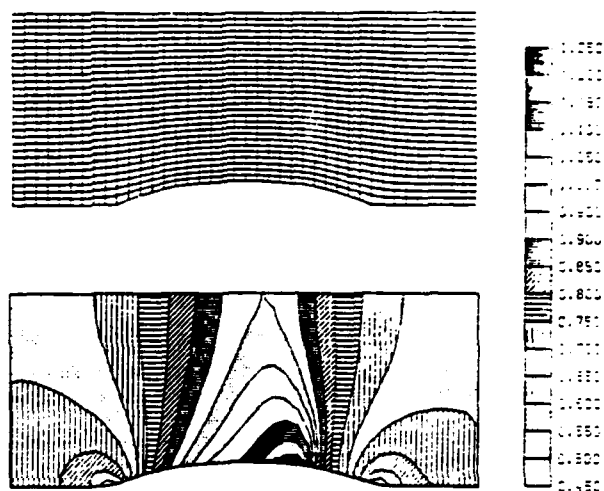
Figure 9a. Final grid and Mach number contours for transonic bump.
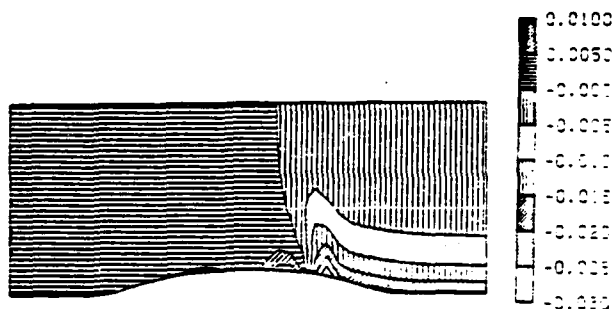
Figure 9b. Relative stagnation pressure loss for transonic bump

Conclusions

This paper has presented a new method for solving the steady-state Euler equations. The numerical examples presented show its capability to handle supersonic, subsonic and transonic flows with direct or inverse boundary conditions. In addition the cascade example shows the ability to determine the correct circulation around an airfoil by explicitly applying a Kutta condition at the trailing edge. Further work is required to improve the accuracy and speed of the transonic solver, and to formulate a transonic inverse procedure.
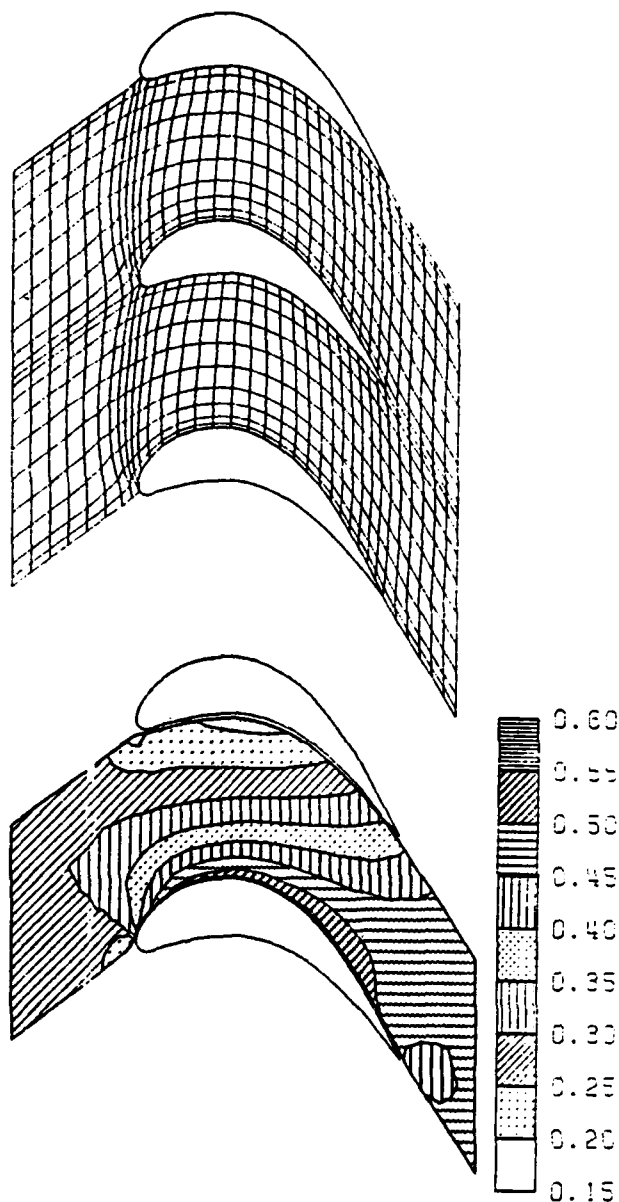

Figure 8. Final grid and Mach number contours for turbine case

and s definitions are the same as for the subsonic solver. To capture shocks, however, "artificial compressibility" is introduced in the mass continuity equation.

$$\bar{\rho}_1 q_1 (\hat{s}_1 \cdot \vec{A}_1) = \bar{\rho}_2 q_2 (\hat{s}_2 \cdot \vec{A}_2) \tag{13}$$

where

$$\bar{\rho}_2 = (1-\mu)\rho_2 + \mu\rho_1 \tag{14}$$

and $\bar{\rho}_1$ is similarly defined. This artificial compressibility was first used by A. Eberle [8] in solving the transonic full potential equation, and has been used more recently by Wornom [9] in solving the quasi 1-D Euler equations. μ is a function of the Mach number M and to ensure numerical stability must satisfy

References

[1] Thompkins, W.T. Jr., Tong, S.S., Bush, R.H., Usab, W.J. Jr., Norton, R.J.G., "Solution procedures for accurate numerical simulations of flow in turbomachinery cascades," AIAA-83-0257, January 1983.

[2] Keith, J.S., Ferguson, D.R., Merkle, C.L., Heck, P.H., Lahti, D.J., "Analytical method for predicting the pressure distribution about a nacelle at transonic speeds," NASA CR-2217, July 1973.

[3] Wennerstrom, A.J., "On the treatment of body forces in the radial equilibrium equation of turbomachinery," ARL 75-0052, Aerospace Research Laboratory, 1974.

[4] Novak, R.A., "Streamline curvature computing procedures for fluid-flow problems," paper 66-WA/GT-3 presented at ASME Winter Annual Meeting, 1966.

[5] Salas, M.D., Jameson, A., Melnik, R.E., "A comparative study of the nonuniqueness problem of the potential equation," AIAA 83-1888, July 1983

[6] Keller, H.B., "A new difference scheme for parabolic problems," in Numerical Solutions of Partial Differential Equations, Vol. II, Academic Press, New York, 1970.

[7] Drela, M., "A new transformation and integration scheme for the compressible boundary-layer equations, and solution behavior at separation," Report No. 172, MIT Gas Turbine and Plasma Dynamics Laboratory, 1983.

[8] Eberle, A., "A method of finite volumes for the calculation of transonic potential flow about wings using the minimum pressure integral," translation of MBB-Report UFE 1407(O), February 1978

[9] Wornom, S.F., "Application of two-point difference schemes to the conservative Euler equations for one-dimensional flows," NASA TM-83262, May 1982.

Acknowledgment

CONSERVATIVE STREAMTUBE SOLUTION
OF STEADY-STATE EULER EQUATIONS

by

M. Drela
M. Giles

CFDL-TR-83-6 November 1983

Department of Aeronautics and Astronautics
Massachusetts Institute of Technology
Cambridge, Massachusetts 02139

Abstract

This report presents preliminary results obtained using a new method for solving the steady state Euler equations. The method is similar to streamline curvature methods but has a conservative finite difference formulation which ensures correct shock capturing. In supersonic applications the solution is obtained by space-marching while in subsonic applications an iterative elliptic relaxation procedure, similar to potential methods, is used. Numerical results are given for;

a) Supersonic jet entering still reservoir (Inverse calculation)

b) Subsonic Ni's bump with 40% blockage (Direct and inverse)

c) Subsonic bump with boundary layer coupling to calculate a separation bubble

d) Transonic Ni's bump with 10% blockage (Direct calculation)

1) Introduction

At present most methods for the numerical calculation of steady-state transonic solutions of the Euler equations are based upon a conservative finite volume approximation to the unsteady equations of motion[2]. This approach has two good features. The first is that it is conceptually straightforward since the unsteady equations are hyperbolic in time and so the same numerical procedure can be used in both the subsonic and supersonic regions. The second is that the conservative finite volume formulation guarantees the correct Rankine-Hugoniot shock jump relations regardless of the details of the shock calculation. The principal disadvantage is that the convergence rate is limited by the relatively slow propagation of wavelike disturbances throughout the domain and their reflection at the boundaries of the computational domain. Current methods try to overcome this limitation by a variety of acceleration methods such as variable time steps, implicit operators with larger time steps, and multigrid with larger time steps on coarser grids, but computation times remain an order-of-magnitude larger than for the solution of the steady-state transonic full potential equation, using iterative relaxation methods, enhanced by multigrid.

An older approach is the Streamline Curvature method which is an iterative relaxation procedure which solves the equations of motion in intrinsic coordinates[1,5,6]. In one version[1] an initial set of streamlines is guessed, the steady-state normal momentum equation is

integrated in the normal direction assuming known enthalpy and entropy variation along each streamtube. The resulting error in the continuity equation then drives a relaxation procedure to move streamlines towards their correct positions. Because it is based upon the steady state equations, the relaxation procedure in the hyperbolic supersonic region is different from that in the elliptic subsonic region. The main advantage of the streamline curvature method is that it is much faster than time-marching methods, and this makes it much more suitable for industrial design applications in which many different geometries need to be analyzed. A secondary advantage is the simple inviscid treatment of adjacent streamtubes with differing stagnation properties. In time-marching calculations numerical dissipation smears the discontinuities. The disadvantages of the standard streamline relaxation method are that the iterative solvers have problems with numerical stability in the supersonic regions, and they do not conserve momentum globally, so that for example the lift on an airfoil may not equal the change in momentum of the fluid. In subsonic cases this momentum loss may be small, but in transonic cases there may be an appreciable momentum loss at the shock. Studies by Salas et al[4] of solutions to the full potential equation show that momentum loss even at relatively weak shocks can produce large errors in shock position.

The method we have developed is similar to the streamline curvature method, but has a conservative finite volume formulation which ensures the correct treatment of shocks. Like the streamline curvature method it solves the steady-state equations and so requires different solvers

or solution algorithms, for purely supersonic, purely subsonic, or transonic problems. The supersonic solver marches in streamwise steps downstream from a known inlet flow. The subsonic solver starts from a guessed set of streamline positions, solves each streamtube problem as a separate quasi 1-D problem, and then relaxes all the streamline positions to satisfy pressure continuity across streamlines. The transonic solver is similar to the subsonic solver but requires numerical dissipation in the supersonic region, and relaxes one streamline at a time instead of all simultaneously. At the present time the supersonic and subsonic solvers are both robust and very fast, but the transonic solver requires further improvement.

2) Supersonic Solver

The geometry and location of flow variables for a typical "cell" of a streamtube is shown in Figure 1. The geometry is defined at the corners of each cell. Density ρ, speed q, and pressure p are defined at the midpoints of the two ends of the cell and the auxiliary pressure Π is defined on the streamline faces of the cell. $\hat{s}$ is a unit vector in the direction of the velocity, and is defined to be tangent to the circular arc passing through the three upstream midpoints as illustrated in Figure 2. A_1, A_2, B^-, B^+ are area vectors normal to the cell faces.

The finite volume formulation of the steady equations is

Mass $\qquad \rho_1 q_1 \hat{s}_1 \cdot \vec{A}_1 = \rho_2 q_2 \hat{s}_2 \cdot \vec{A}_2$ $\qquad\qquad\qquad$ (1a)

Momentum $\quad p_1 \vec{A}_1 + (\rho_1 q_1 \hat{s}_1 \cdot \vec{A}_1) q_1 \hat{s}_1 + \Pi^- \vec{B}^- =$ $\qquad$ (1b)

$$p_2 \vec{A}_2 + (\rho_2 q_2 \hat{s}_2 \cdot \vec{A}_2) q_2 \hat{s}_2 + \Pi^+ \vec{B}^+$$

Enthalpy $\quad \dfrac{\gamma}{\gamma-1} \dfrac{p_1}{\rho_1} + \dfrac{1}{2} q_1^2 = \dfrac{\gamma}{\gamma-1} \dfrac{p_2}{\rho_2} + \dfrac{1}{2} q_2^2$ $\qquad$ (1c)

In addition there is an auxiliary pressure equation which constrains the average of the pressures on the two pairs of opposing faces to be equal.

$$p_1 + p_2 = \Pi^+ + \Pi^- \qquad \text{(1d)}$$

At the inlet boundary all the variables need to be specified. At the top and bottom boundaries one boundary condition needs to be specified, and at present the code accepts either a specified wall position (direct case) or a specified pressure (inverse case). With these prescribed boundary conditions the solver marches downstream from the inlet, solving all of the equations at each streamwise station by using an approximate Newton-Raphson linearization of the equations, which requires typically about four iterations at each station. The process is similar to Keller's box method for the solution of the boundary layer equations.

Figure 3 shows a Mach number contour plot, and the final streamline grid for a 2-D supersonic jet entering a stagnant reservoir filled with a gas of higher static pressure. Before entering the reservoir the flow is parallel with specified top and bottom walls. After entering the reservoir the top and bottom streamlines have constant specified

pressure. This case physically corresponds to the Mach diamond pattern produced by a supersonic nozzle exhausting into a still atmosphere and took only 10s on a PDP11/70 to achieve convergence to machine roundoff.

3) Subsonic Solver

Initially our subsonic solver used the same geometry and location of flow variables as the supersonic solver. Unfortunately there were problems with numerical stability and unacceptably high errors. These problems were overcome by going to the slightly different geometry shown in Figure 4, without needing to resort to numerical dissipation. There are now two grid structures, a relaxation grid with coordinates defined at its nodes, and a conservation grid with its corner nodes defined to be the midpoint of the corresponding streamline faces on the relaxation grid. The $\hat{s}$ unit vector in the direction of the velocity is defined to be parallel to a line connecting midpoint of normal faces on the relaxation grid as shown in Figure 5. The steady state conservation equations are exactly the same as for the supersonic solver but the solution procedure is totally different. Since the equations are elliptic, an iterative relaxation procedure, very similar to some streamtube curvature solvers, is required. First an initial set of streamline positions is chosen. Then each streamtube is treated separately and Equations (1a-1d) are solved simultaneously at each streamwise station using a Newton-Raphson technique incorporating the boundary conditions, specified stagnation pressure total enthalpy and exit pressure. These calculations produce pressures Π^+, Π^- on the

upper and lower surfaces of each streamtube. In the converged steady state these must match the corresponding pressures from neighboring streamtubes so the pressure jump $\Delta\Pi$ across the streamline drives a relaxation of the streamline positions. Assuming locally isentropic behavior, influence coefficients are calculated for the effect of geometry changes on the local streamtube areas and curvature, and hence on the Π values. The resultant relaxation equation for the case in which the "normal" lines are orthogonal is

$$(1-M^2)\delta_s^2 + \delta_n^2 \quad \tilde{y} = -\frac{1}{\rho u^2 A} \Delta\Pi \tag{2}$$

In this equation M is the Mach number, $\tilde{y}$ is the normal correction in the streamline position, A is the streamtube area and $\Delta\Pi$ is the forcing pressure mismatch across the streamline. δ_s^2 and δ_n^2 are finite difference approximations to second derivatives in the streamwise and normal directions. Thus this equation is very similar to both the transonic small disturbance equation and the streamtube curvature relaxation method used by Keith et al. We solve (2) using a standard SLOR technique, update the streamline positions and then repeat the cycle until $\tilde{y}$ and $\Delta\Pi$ become acceptably small.

The test example is a duct with a 40% blockage bump. The inlet Mach number is approximately 0.27 with a maximum Mach number in the throat of approximately 0.52. Figure 6 shows the initial and final streamline grids. To increase the resolution at the stagnation points two narrow streamtubes are used next to the lower wall and there are

additional normal lines at the front and back of the bump. The only

discernable difference between the initial and final grid is a

thickening of the streamtubes near the stagnation point. Contour plots

of the Mach number and relative stagnation pressure loss are shown in

Figure 7. Because the equations are second-order accurate and no

numerical dissipation has been needed to maintain stability, the

stagnation pressure loss is much lower than for time-marching codes[2].

This test case has also been used to check the capabilities of the

solver in its inverse mode. The pressure on the lower wall was set

equal to the pressure computed by the direct method, and the initial

grid was chosen to be the rectangular duct without the bump. In approx-

imately 50 iterations the streamlines and flow variables converged (to

within machine roundoff) to the values computed by the direct method.

The ability to prescribe wall position and/or wall pressure in our

formulation makes efficient boundary layer (BL) coupling possible even

in strongly coupled cases with separation bubbles (Figures 8, 9a,b).

For this example, a finite difference BL code using a Shifted Box

Scheme[8] was used. Simultaneous BL calculations and downstream relax-

ation sweeps are used to drive the Euler and BL edge velocities together

at the displacement surface. During the relaxation of the inviscid

flow, a hybrid boundary condition prescribing a linear combination of

edge pressure and position simultaneously drives these quantities

towards the matching condition. The behavior of the BL is locally

modeled by a $u_e - \delta^*$ influence coefficient which is a byproduct of the

BL calculation.

The coupled solution in Figures 9a,b required 120 relaxation sweeps and 12 BL calculations to fully converge. The purely inviscid case in Figure 8 required 50 relaxation sweeps. This preliminary coupling case indicates that coupled calculations will not require drastically more computation time than purely inviscid calculations.

4) Transonic Solver

The transonic solver is still under development. The current solver is not very fast or robust but is sufficient to demonstrate the feasibility of this approach for transonic cases. The grid geometry is the same as the supersonic solver. At supersonic points the supersonic $\tilde{s}$ definition is used. At subsonic points $\tilde{s}$ is defined to be tangent to the circle passing through the neighboring midpoints as shown in Figure 1. The main feature of the transonic steady state equations is the introduction of an "artificial compressibility" term in the continuity equation. The mass conservation equation is

$$\bar{\rho}_1 q_1 (\hat{s}_1 \cdot \vec{A}_1) = \bar{\rho}_2 q_2 (\hat{s}_2 \cdot \vec{A}_2)$$

where

$$\bar{\rho}_2 = (1-\mu)\rho_2 + \mu \, \rho_1$$

and $\bar{\rho}_1$ is similarly defined.

This artificial compressibility was first used by A. Eberle[7] in solving the transonic full potential equation, and has been used more recently by Wornom [3] in solving the quasi 1-D Euler equations. μ is

a function of the Mach number M and to ensure numerical stability must satisfy

$$\mu > \max \left[0, \; \frac{1}{\gamma+1} \frac{M^2-1}{M^2} \right]$$

The iterative solution procedure is to guess an initial streamline grid and then sweep from side to side in the normal direction, relaxing each streamline by assuming neighboring streamlines are fixed and so solving the steady state equations for the two streamtubes on either side of the streamline using a Newton-Raphson procedure.

Figure 10 shows the final grid and Mach number contour plot for a fully choked duct with a 25% blockage bump.

REFERENCES

1. Keith, J.S., Ferguson, D.R., Merkle, C.L., Heck, P.H., Lahti, D.J., "Analytical method for predicting the pressure distribution about a nacelle at transonic speeds," NASA CR-2217, July 1973.

2. Thompkins, W.T. Jr., Tong, S.S., Bush, R.H., Usab, W.J. Jr., Norton, R.J.G., "Solution procedures for accurate numerical simulations of flow in turbomachinery cascades,"AIAA-83-0257, January 1983.

3. Wornom, S.F., "Application of two-point difference schemes to the conservative Euler equations for one-dimensional flows," NASA TM-83262, May 1982.

4. Salas, M.D., Jameson, A., Melnik, R.E., "A comparative study of the nonuniqueness problem of the potential equation," AIAA 83-1888, July 1983.

5. Wennerstrom, A.J., "On the treatment of body forces in the radial equilibrium equation of turbomachinery," ARL 75-0052, Aerospace Research Laboratory, 1974.

6. Novak, R.A., "Streamline curvature computing procedures for fluid-flow problems," paper 66-WA/GT-3 presented at ASME Winter Annual Meeting, 1966.

7. Eberle, A., "A method of finite volumes for the calculation of transonic potential flow about wings using the minimum pressure integral," translation of MBB-Report UFE 1407(0), Feburary 1978.

8. Drela, M., "A new transformation and integration scheme for the compressible boundary-layer equations, and solution behavior at separation," Report No. 172. MIT Gas Turbine and Plasma Dynamics Laboratory, 1983.

FIGURE 1.   Finite Volume Geometry for Supersonic Solver.
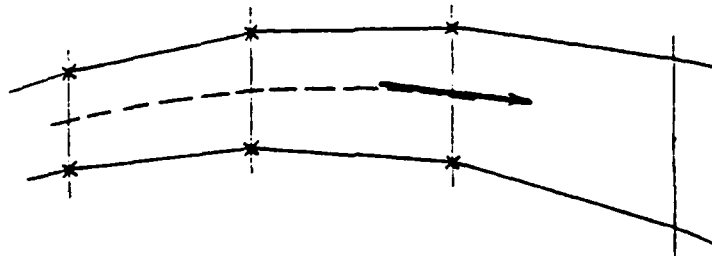
FIGURE 2.   Definition of Supersonic Unit Velocity Vector $\hat{s}$.

2.800
2.600
2.400
2.200
2.000
1.800
1.600
1.400
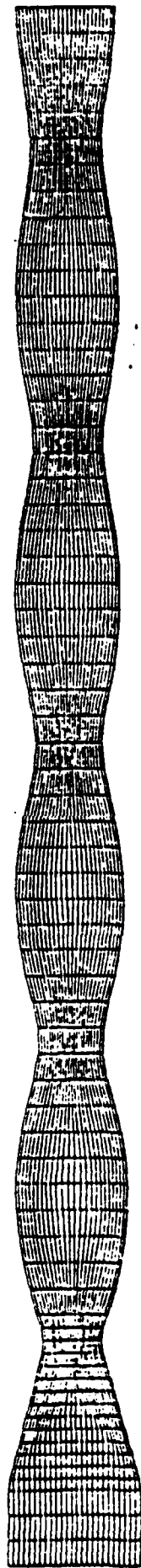
FIGURE 3a. Streamline positions for supersonic jet inverse calculation

streamline position specified

Static pressure specified

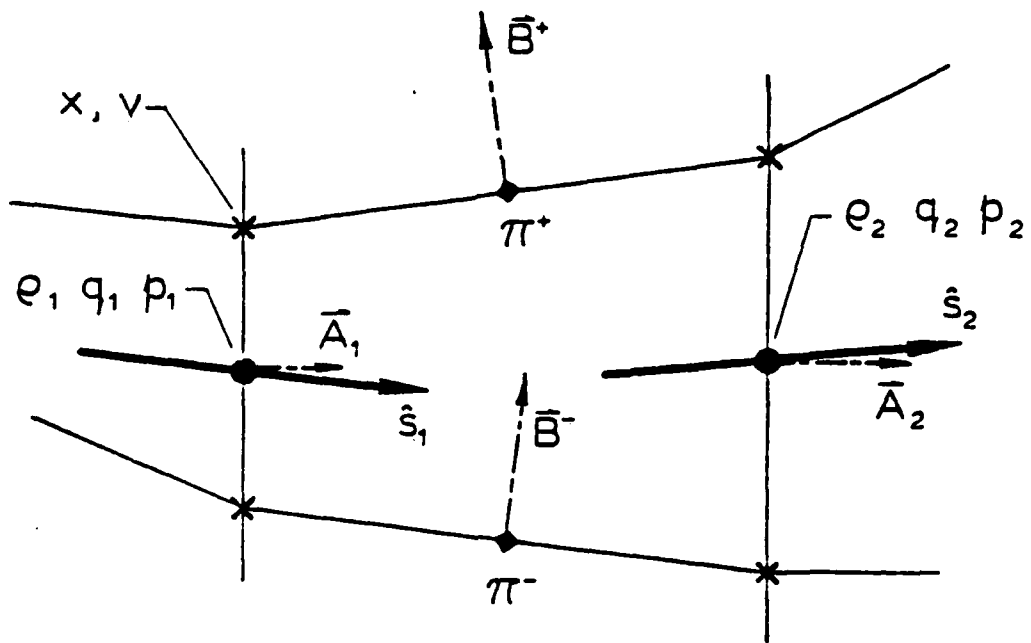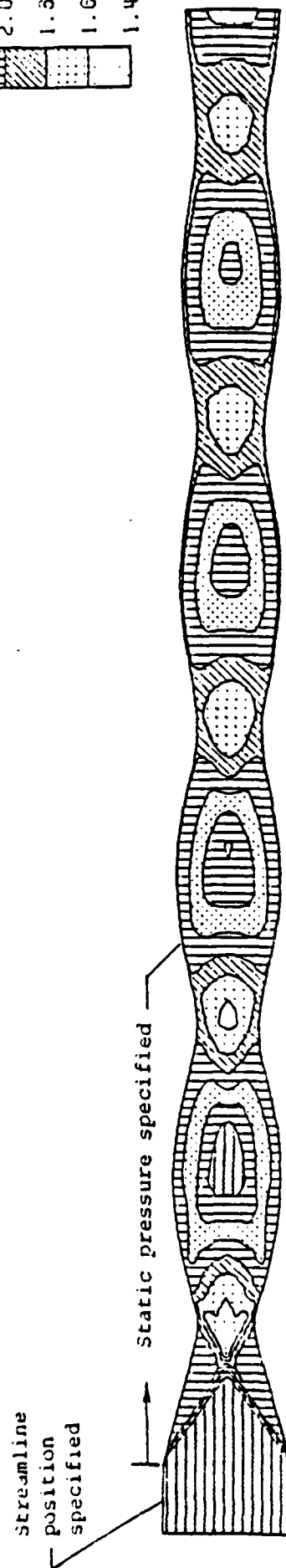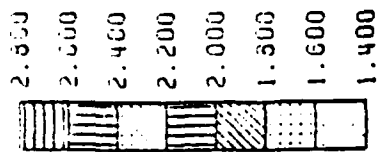FIGURE 3b. Mach number contours for supersonic jet inverse calculation
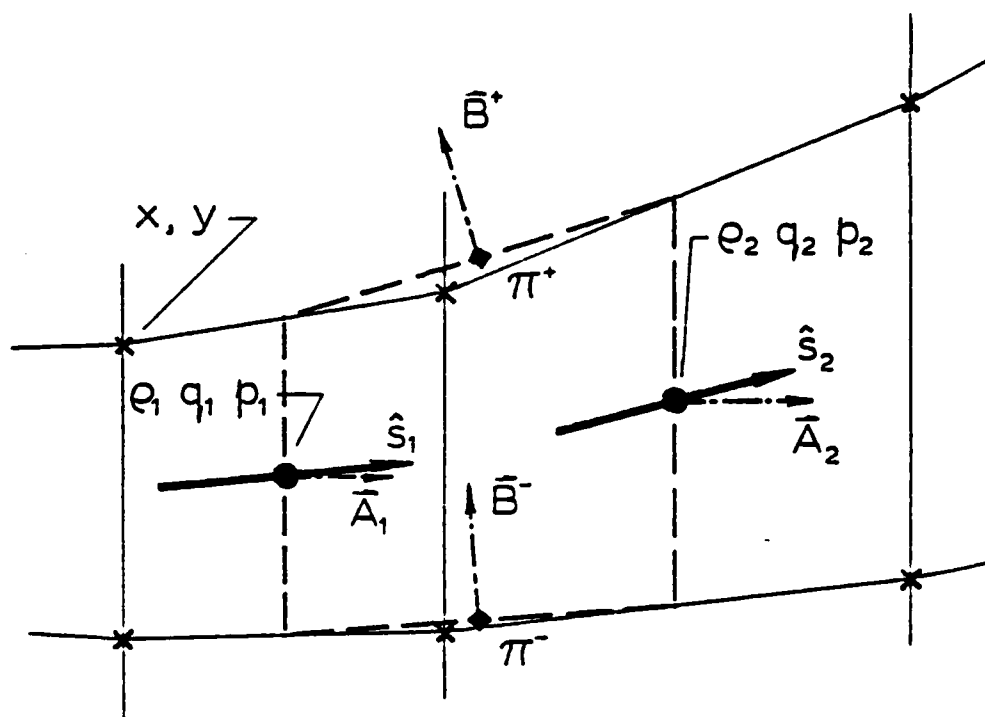
FIGURE 4.   Finite Volume Geometry for Subsonic Solver.
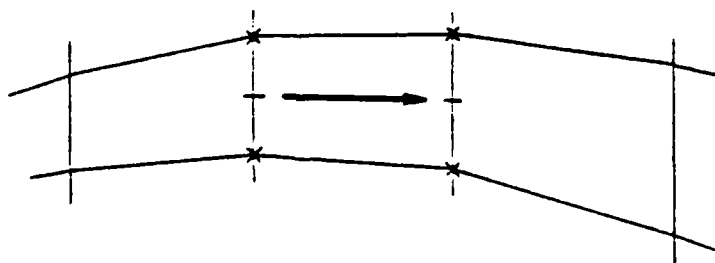
FIGURE 5.   Definition of Subsonic Unit Velocity Vector $\hat{s}$.
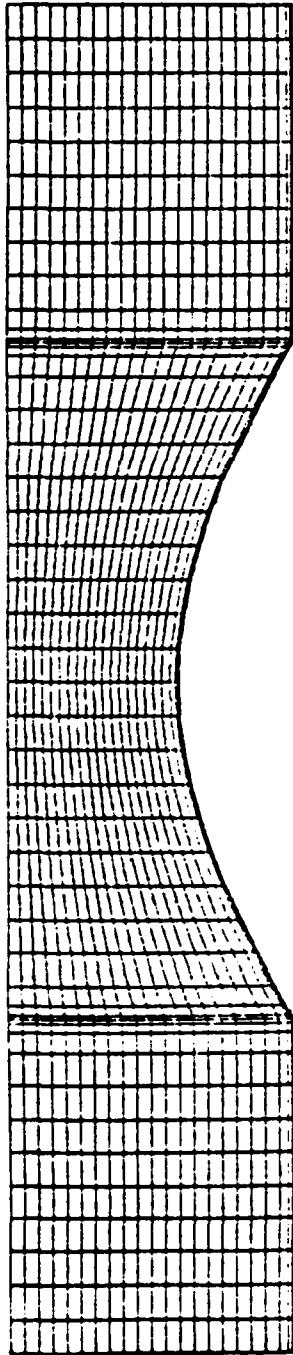
FIGURE 6a. Initial Grid, Subsonic Direct Calculation.
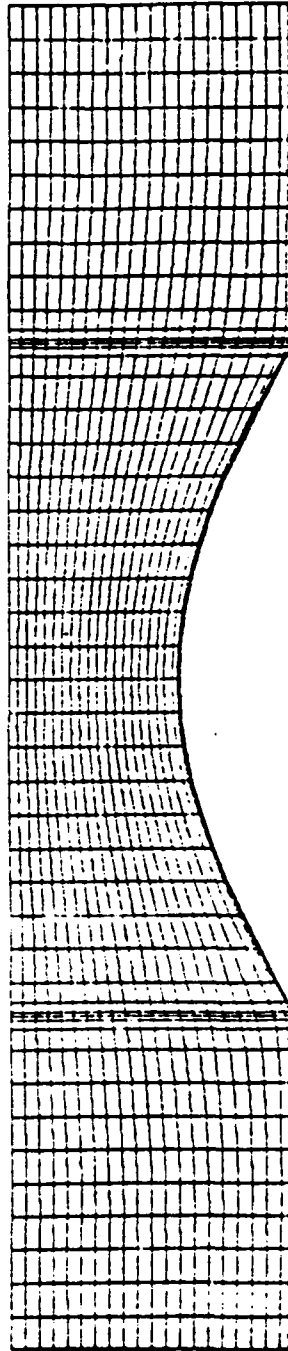
FIGURE 6b. Final Grid, Subsonic Direct Calculation.

0.550
0.500
0.450
0.400
0.350
0.300
0.250
0.200
0.150
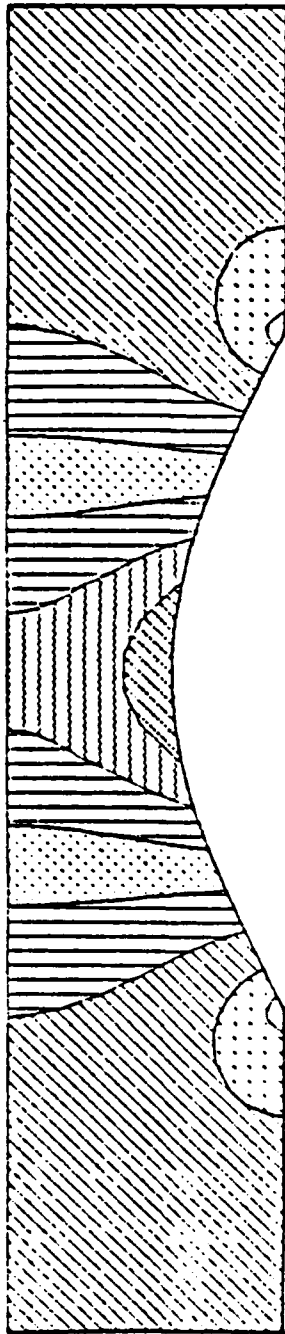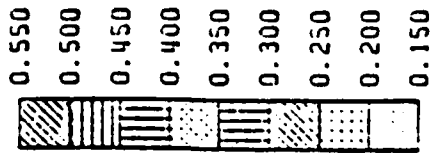
FIGURE 7a. Mach Number Contour Plot, Subsonic Direct Calculation.

0.0006
0.0005
0.0004
0.0003
0.0002
0.0001
-0.0000
-0.0001
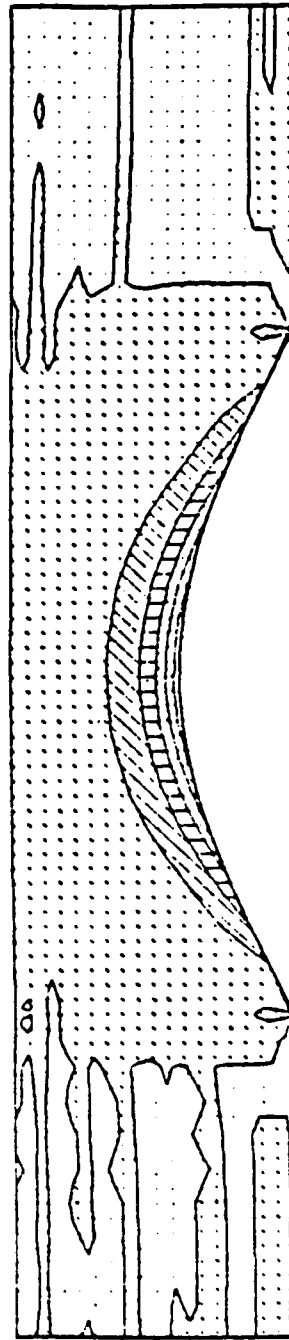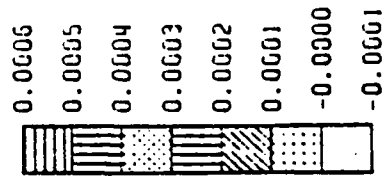
FIGURE 7b. Relative Stagnation Pressure Error, Subsonic Direct Calculation.
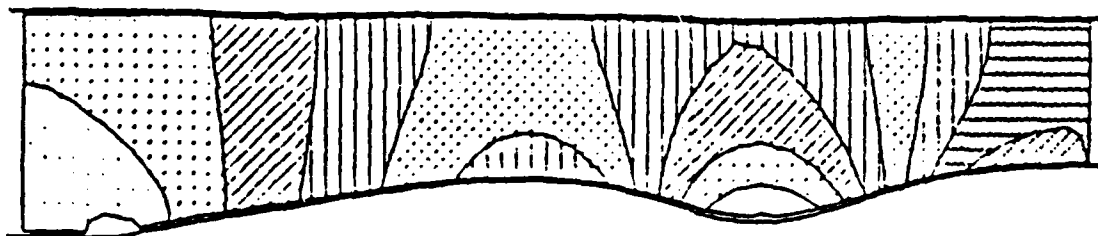
FIGURE 8. Mach number contour plot without boundary layer interaction

$Re = 10^4$
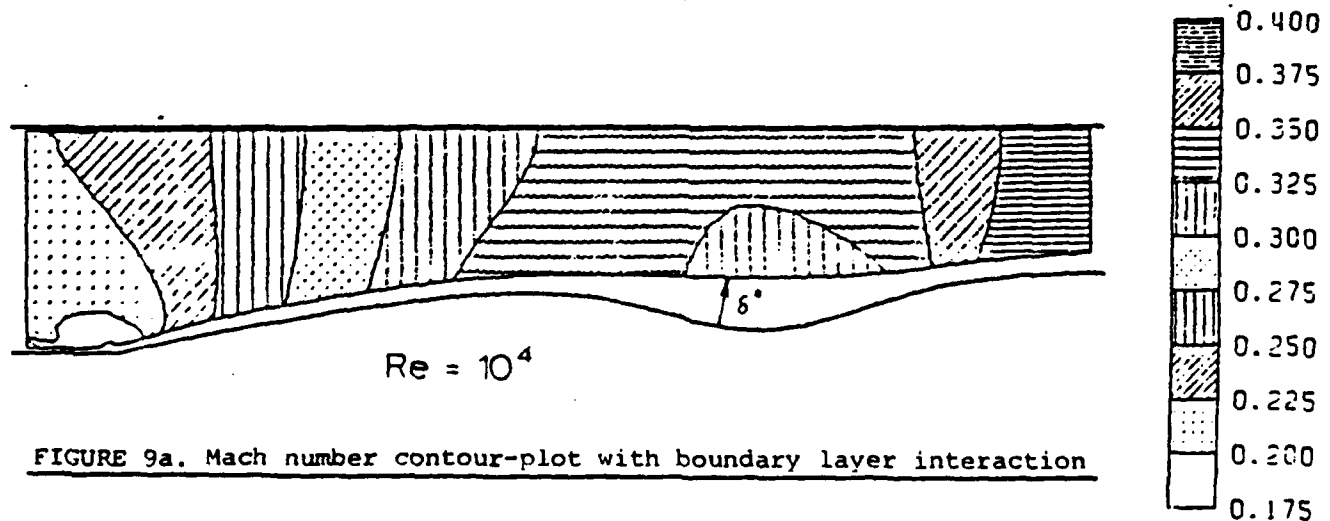
FIGURE 9a. Mach number contour-plot with boundary layer interaction

△ 10.000 X EDGE MACH NUMBER
◇ 1.000 X DISPLACEMENT THICKNESS
Z 10.000 X WALL SHEAR
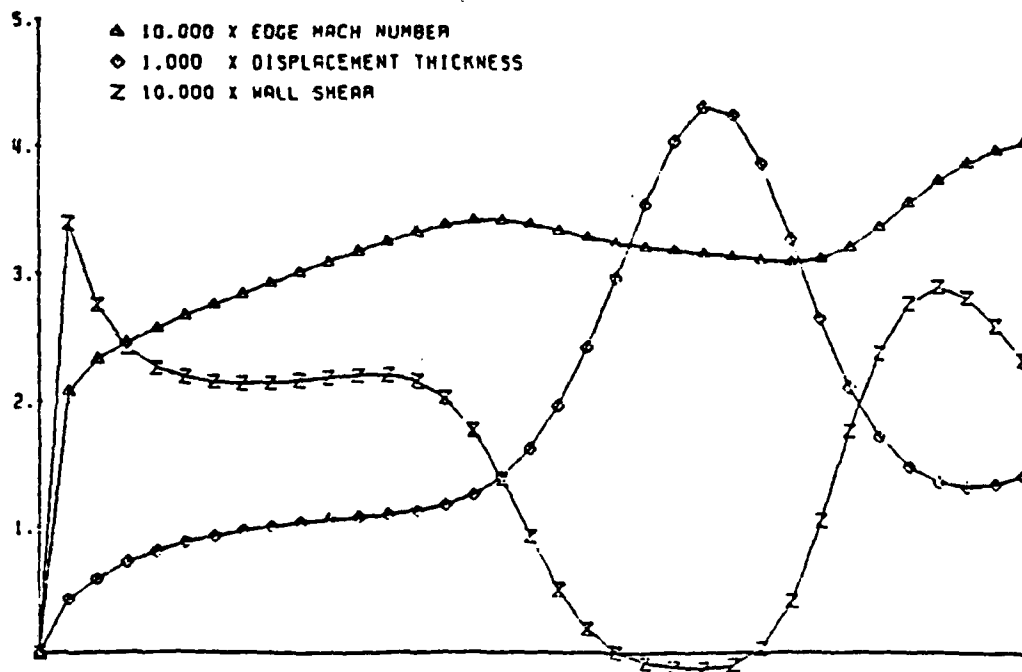
FIGURE 9b. Boundary layer parameters for interaction calculation
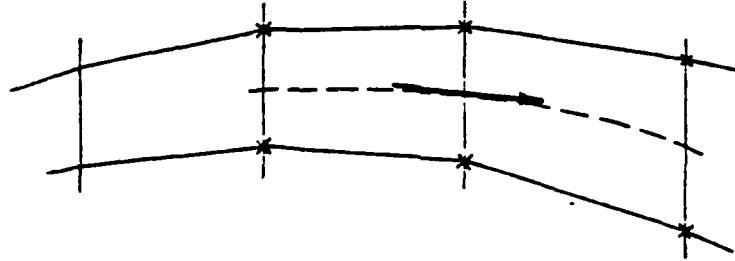
FIGURE 10. Unit Velocity Vector Definition in Subsonic Regions of Transonic Calculation.
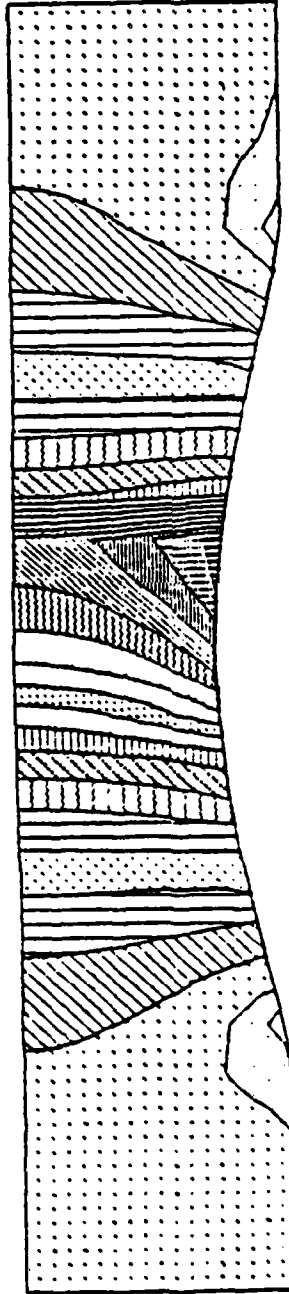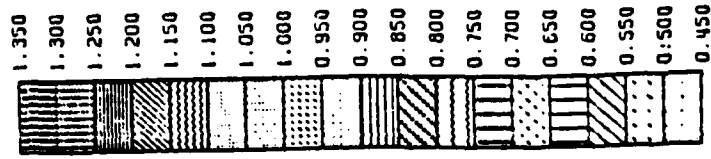
Figure 11. Mach number contour plot for transonic bump calculation with normal shock

TASK IB: LOSS MECHANISMS AND LOSS MIGRATION IN TRANSONIC COMPRESSORS

Introduction

The objective of this study is to quantify the understanding of loss production versus loss migration by detailed time-resolved radial streamline/pathline measurements in the AFAPL High Through Flow Compressor, a transonic compressor stage, in the MIT Blowdown Compressor.

Streamline tracing in a transonic, unsteady compressor flow requires that streamlines or pathlines be identified in the presence of simultaneous first order nonperiodic changes in total pressure and temperature.

The basic technique is to inject a thin ring of the tracer gas upstream of the compressor rotor and then survey with a concentration probe at the rotor exit to map the radial transport of the tracer gas. The injection ring is then moved radially and the experiment repeated. In this manner the time-dependent radial transport within a transonic compressor rotor can be mapped simultaneously with a timeresolved measurement of rotor loss (from a cotemperal and pressure measurement).

The dual wire aspirating probe will be used for the simultaneous measurement of time-resolved concentration, temperature, and pressure possible at frequencies up to 20 KHz. The probe consists of two constant temperature hot wires operated at different overheat ratios in a channel with a choked exit. Thus the flow past the wires is at constant Mach number. The heat flux (and thus the electrical signal) from the wires is a function only of freestream total pressure and temperature and gas composition. Previously, the probe was used in a flow of constant composition.

Thus, the signals from the two wires were sufficient to permit calculation of the two unknowns, total pressure and temperature. A piggyback total pressure sensor was used as a redundant check. In this investigation, the pressure sensor is used to provide the third signal to allow the three independent variables (concentration, temperature, and pressure) to be derived at each instant in time.

Progress to Date

Work to date has concentrated on tracer gas selection, probe calibration, and injector design. The selection of the proper tracer gas is important. Ideally, the tracer should have the same density as the main flow while differing in those fluid properties important to the probe operation: thermal conductivity, viscosity, ratio of specific heats, and molecular weight. We have examined the suitability of several gases and gas mixtures in regard to the above criteria and concluded that the two most promising for use in the Argon-Freon-12 atmosphere of the MIT Blowdown Compressor are carbon dioxide and Freon 153A. Krypton is also suitable but quite expensive. Figure 1 illustrates the calculated voltage output from the aspirating probe as a function of gas temperature and CO_2 fractional concentration in the Argon-Freon mixture used in the MIT Blowdown Compressor Facility.

It is clear from the analysis that the success of the experiment hinges on the overall stability of the aspirating probe since the variations due to concentration changes are relatively small, representing the difference between two large numbers. Preliminary laboratory calibration tests with CO_2 look promising. These tests are continuing, to both

establish the calibration and data reduction procedures and to assess the long term probe stability.

The gas injector has been designed and is now being fabricated. The design goal is the injection of a 1 mm thick sheet of tracer gas with the same velocity and static pressure as the main flow in order to minimize the turbulent mixing of this sheet as gas propagates downstream. The injector (figure 2) consists of a NACA 65_4-021 airfoil limited to two blade passages in circumferential extent in order to reduce the amount of injection gas required. The hollow airfoil contains a plenum (instrumented with a pressure transducer) feeding a 0.8 mm wide slot at the trailing edge. The injector is supported by two radial struts of similar cross-section which carry the injection gas. The entire assembly is mounted through the tip casing which permits the radial position to be varied. O-rings provide the seal at this point. The vibrational frequencies of the injector assembly has been calculated to insure that no resonances lie within the range that can be forced by the rotor.

An attempt was made to calculate the extent of the radial mixing due to turbulent shear as the injectant sheet is convected downstream. Because this is such a strong function of the precise pressure and velocity match at the injector trailing edge and because various models give such disparate results, the only believable figures will be those from measurements. These will be done by surveying across the compressor annulus at the rotor exit station with the blade rows removed, thus establishing a baseline for comparison with the rotor exit measurements.

It is anticipated that most of the calibration work will be completed by the time the injector assembly is fabricated. The baseline measurements described above will then begin.
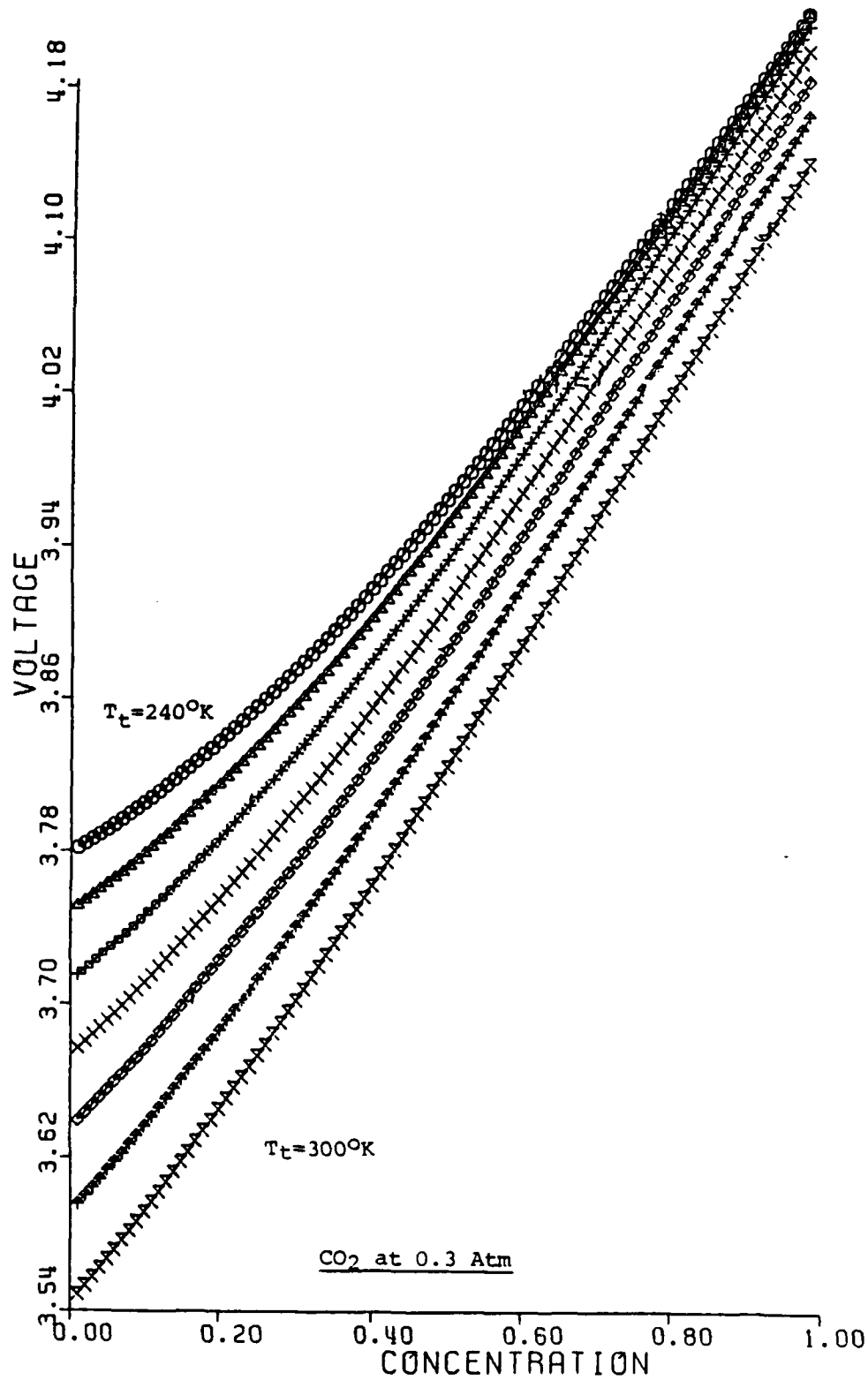
Fig. 1

Aspirating probe output voltage as a function of CO_2 concentration at different freestream total temperatures. The total pressure is 0.3 atm.

USAF HIGH THROUGH FLOW COMPRESSOR

Instrumentation Stations

Probe Survey Plane

Stator

Rotor
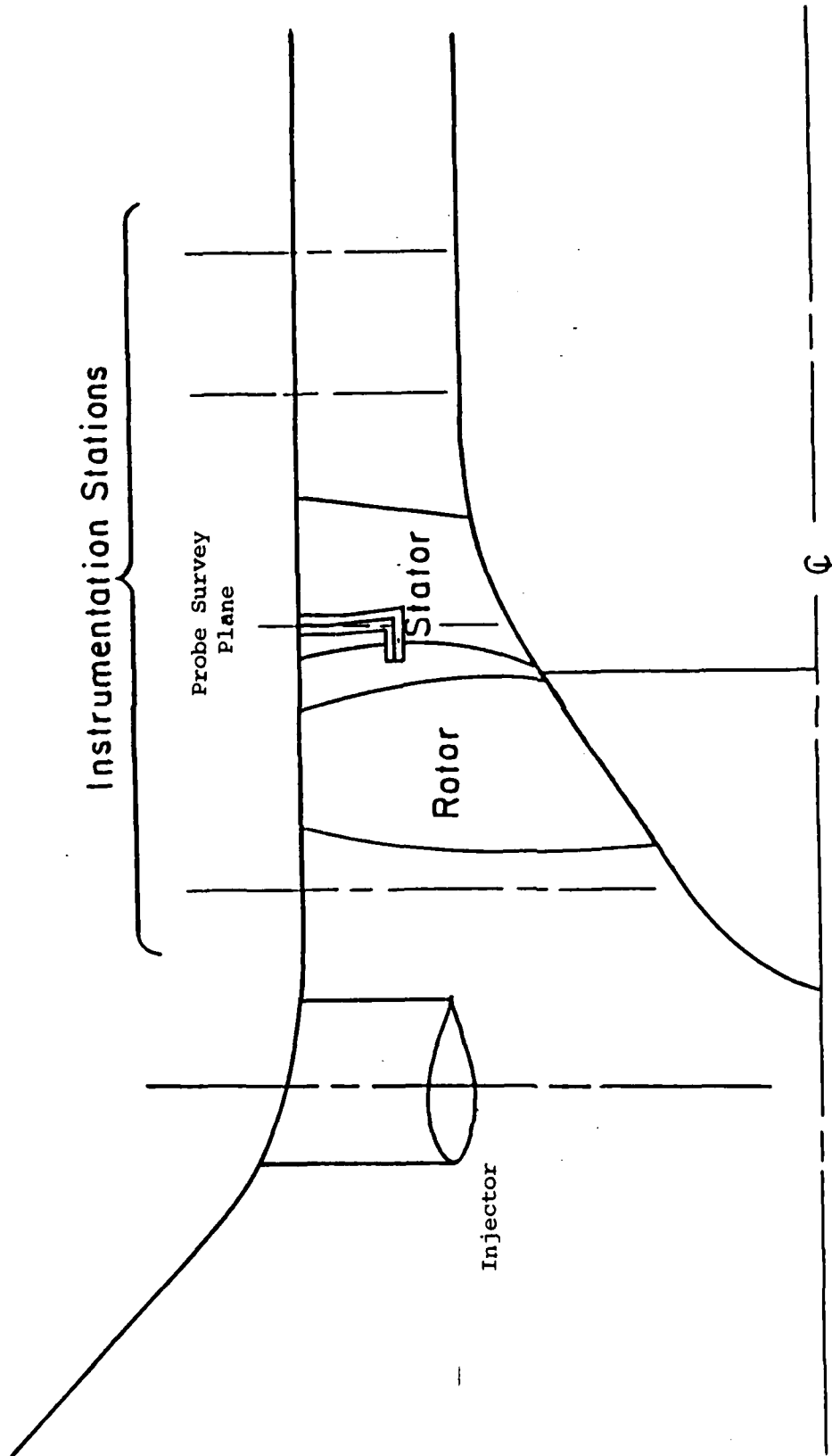
Injector

Design Point: $\dot{m}$ = 28.6 kg/sec

PR = 2.06

η = .882

Figure 2A: Scale Drawing of Injector Mounted in Blowdown Compressor Facility, side view

Injector   Rotor   Stator
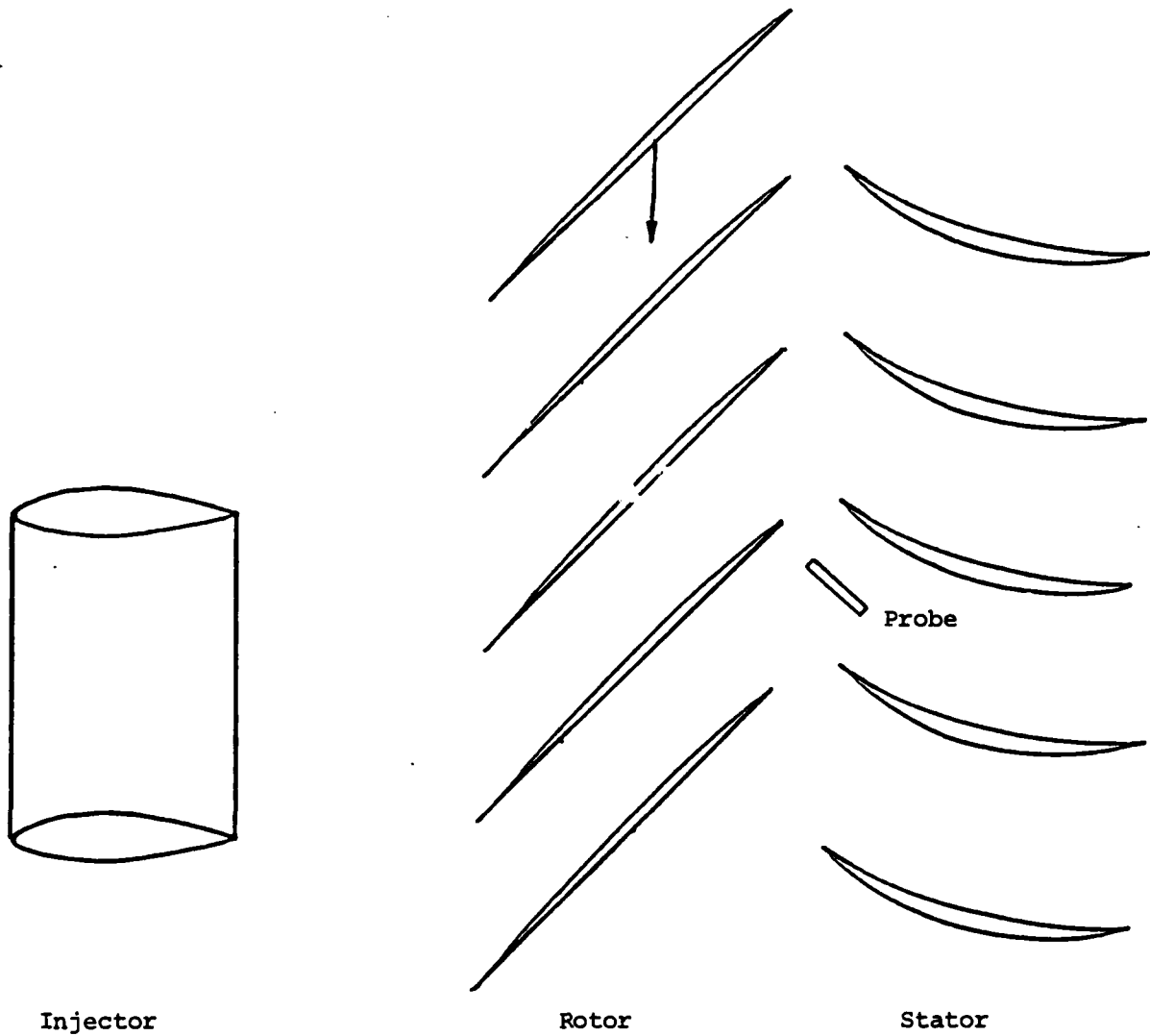
Figure 2B: Scale Drawing of Compressor Mounted in
Blowdown Compressor Facility, radial view

TASK II: COMPRESSOR STABILITY ENHANCEMENT USING HUB/CASING TREATMENT

The overall goal of this study is the understanding of the basic mechanism(s) by which a grooved casing or hub is able to significantly extend the stable flow range of a turbomachine. A key concept in this is, in our view, a quantitative appreciation for the fluid mechanics of the interchange of momentum between the casing and the flow in the endwall region of the blade passage.

In our first series of experiments, carried out over the past several years, we showed that a moving grooved hub could have a very potent effect on stator stall margin and pressure rise [2.1]. (This was the first time this had been demonstrated.) This result meant that we could examine the relevant phenomena using the stator passage/moving hub configuration. The present series of experiments are aimed much more at the basic phenomena associated with hub and casing treatment, and involve a detailed examination of the three-dimensional, unsteady flow within the blade passage. This work will form part of the M.S. Thesis of Mr. Mark Johnson, who is in the AFRAPT Program.

In previous progress reports, we mentioned the design, development, and fabrication of the instrumentation and the necessary software to enable us to examine in detail the unsteady flow in the stator passage. We also mentioned the design of an optical detector system to interact with our LSI 11/23 microcomputer to monitor the relative position of the grooves accurately during the experiment. In the 6-month period following that progress report, we have essentially completed the tasks mentioned above. In addition, we have also accomplished the following tasks:

(1) With the newly designed and built inlet contraction section mounted on, measurements of the inlet velocity profile upstream of the single stage low speed compressor were taken to compare with the previous results as a check. No substantial difference in the results was observed except that, as might be expected because of the longer flow path, the boundary layer on the casing is thicker than before (i.e., with the old inlet section on).

(2) The compressor characteristics, pressure rise versus flow, were retaken both for the cases of smooth hub and treated hub to compare with previous results as a check. This data is shown as Figure 2.1. The large differences between the smooth wall and the grooved wall pressure rise as well as stall onset points (essentially at the peaks of the curves) are evident. Although the relative positions of the curves are close to those measured previously, there is a difference (of about 5%) in the absolute levels of flow and pressure from previous measurement for both smooth wall and hub treatment. This may be due to the larger inlet boundary layer resulting in a changed profile presented to the stator. However, because of the departure of Mr. Johnson for Garrett (where he is working for the summer, as part of the AFRAPT program) we have not resolved this with any degree of precision.

(3) Preliminary experiments were carried out to validate and test the overall data acquisition system. This includes the traverse system for probe (hot wire or pressure) with three degrees of freedom (linear translation, angular motion in a radial axial plane in the stator blade passage, and rotation on its own axis) and the optical detector system, for

monitoring the groove position.

An inclined hot-wire probe was used to obtain high response data at a particular point in the blade passage from which the three velocity components at that point can be reduced. This probe had been separately calibrated in a GTL jet facility. The spatial resolution achievable with this _current_ hot wire probe is 2 to 3 mm.

The data matrix grid can be described by a three-dimensional co-ordinate system (I,J,K) fixed to the laboratory frame. Each I refers to a plane concentric with the hub surface (for instance I = 1 refers to a plane 2.25 mm from the hub, I = 2 to that 12.25 mm from the hub, etc.). Each J refers to a plane parallel to a mean-chord plane with J = 1 plane being closest to the blade suction surface. Finally, each K refers to a plane parallel to the leading end trailing edge plane with K = 1 plane being the leading edge plane.

For this set of preliminary experiments, the data matrix chosen is such that on each I plane (I varies from 1 to 5, I = 5 is roughly the mid-span plane) there is a 4 by 7 grid (i.e., J = 1 to 4 while K = 1 to 7). A separate set of data was taken at grid points outside the above data matrix grid for ascertaining the periodicity of the flow from passage to passage. In the preliminary experiments, hot wire data were acquired for runs with smooth hub wall as well as groove-treated hub wall, with the compressor operating at 2600 rpm and at flow coefficients varying from 0.24 to 0.37. The hot wire data have not yet been reduced to yield the three-dimensional flow field in the blade passage region close to the smooth and treated hub surfaces. However, it does appear from this set of experi-

ments, that the overall data acquisition system performs satisfactorily. We do not as yet rule out any future modifications and refinements to the data-acquisition system if we find it necessary to do so.

We hope that, in the next few months, efforts will be expended to obtain the three-dimensional velocity field in the passage from this hot-wire data, and to examine possible three-dimensional presentations of this information. Such a presentation would enhance our ability to view the results in a more interpretative and constructive way. This preliminary set of experiments should also enable us to refine and to plan our measurements of the flow in the next set of experiments. When this set of measurements has been carried, out, we also hope to take up again our theoretical (modelling) work on this problem. This is an area which we have not had time to pursue over the past year but one that is a crucial part of a balanced research effort on this topic.

Reference

2.1 Cheng, P., Drell, M.E., Greitzer, E.M. and Tan, C.S., "Effects of Compressor Hub Treatment on Stator Stall and Pressure Rise," J. Aircraft, 21, 469-476.

STATØR STATIC TØ STATIC PRESSURE RISE
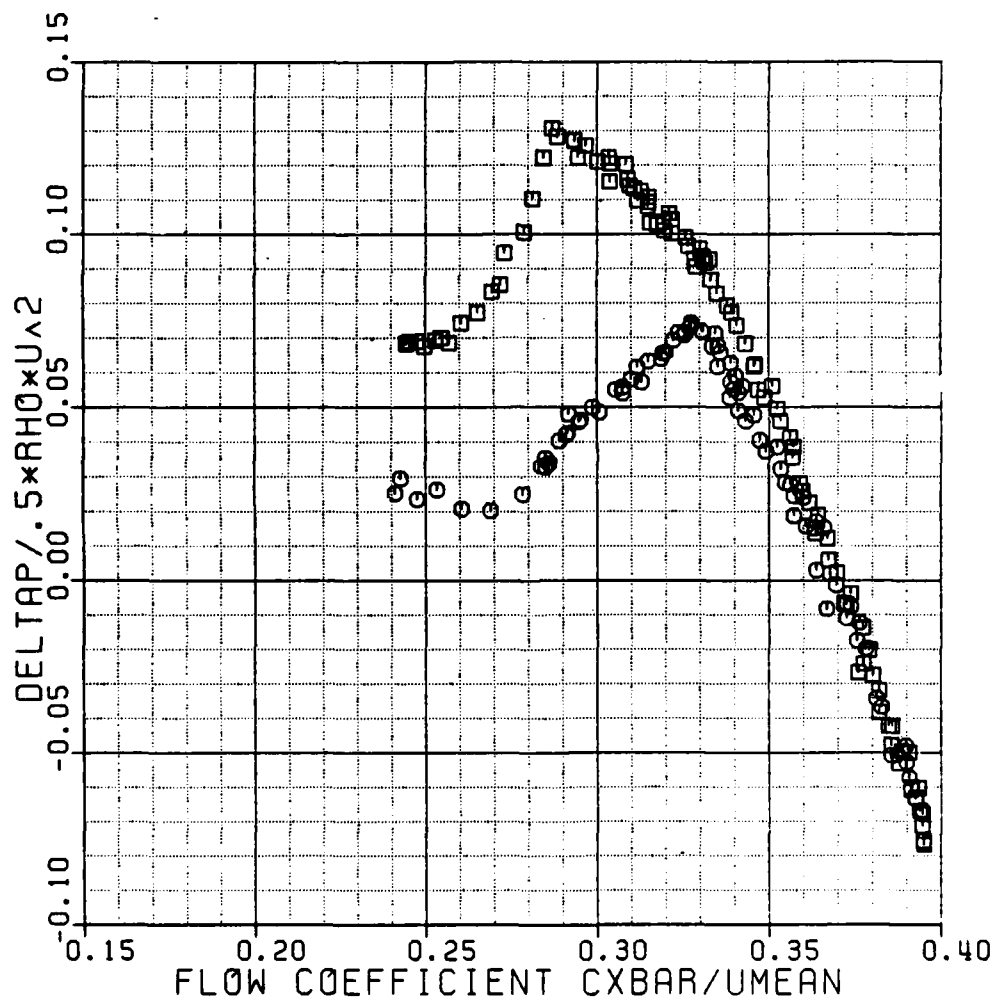
Figure 2.1

TASK III: INLET VORTEX FLOW DISTORTIONS IN GAS TURBINE ENGINES

During the past six months, we have nearly completed the experimental part of our investigations of this phenomenon (at least the first phase - the vortex formation process). These have provided not only quantitative information on vortex strength, but also insight into the basic vortex structure associated with this type of flow. A paper on this work is currently being prepared for submission. A draft of this paper is presented below.

INTRODUCTION

Gas turbine engine operation near the ground is often associated with the presence of a strong vortex which stretches between the ground and the engine inlet. This "inlet vortex" (or ground vortex) can be of concern because of the effects it can have on the engine. These include foreign object damage, increased blade erosion due to dirt ingestion [1], and compressor surge [2].

Investigations of the inlet vortex have identified two basic mechanisms that are responsible for its formation [3]. The first is the amplification of the vertical component of ambient vorticity, i.e., vorticity created far ustream of the inlet, as the vortex lines are convected into the inlet. A detailed description of this process, including calculations of the drift of these vertical vortex lines in the three-dimensional flow produced by an inlet near a ground plane, is given in [3].

The second mechanism for vortex formation, however, does not depend on the presence of ambient vorticity. This process can occur in a flow that is irrotational far upstream, for an inlet in crosswind. In this situation, because of the variation in circulation along the inlet, a trailing vortex (from the rear side of the inlet) is also present. It is this second mechanism, which appears to be less well understood, that forms the focus of the present paper.

In previous investigations, the flow regimes encountered with an inlet/ground plane configuration were found to depend strongly on two parameters: 1) the ratio of inlet (average) velocity to upstream velocity, U_i/U_e, and 2) the ratio of inlet centerline height to inlet inside diameter, H/D. For an inlet in crosswind in an upstream irrotational flow, at low values of velocity ratio, U_i/U_e, and/or high values of H/D, two counter-rotating vortices trailed from the rear of the inlet. These are depicted in Figure 1(a), which is taken from the hydrogen bubble flow visualization studies in [3]. When H/D was fixed and the velocity ratio was increased, or H/D decreased for a fixed velocity ratio, an inlet vortex/trailing vortex system was formed, as indicated in Figure 1(b).

As described in [3], the presence of this trailing vortex is associated with the variation in circulation (i.e., circulation round the inlet) along the axial length of the inlet. A schematic of the location of the vortex lines in the flow shown in Figure 1(b), which indicates this, is given in Figure 2. The circulation around curve C_2, which is just forward of the inlet lip and encloses the inlet vortex, is Γ_2. Far from the lip, around curve C_1, it is argued that the circulation is small. If this is so, there must be a trailing vortex with circulation of strength approximately $-\Gamma_2$, as indicated in the figure. It should be emphasized that Figure 2 is a very simplified picture, and that we will examine the vorticity field in more detail below.

The previous investigations, which were carried out in a water tunnel, were only qualitative in nature. In particular, they provided only very rough estimates of the key fluid mechanic parameters: vortex strength and position. These are required for the determination of the velocity non-uniformity presented to the engine or the degree to which particles are ingested. The present study was thus undertaken to quantify the observed phenomena; more precisely, to provide quantitative measurements of the three-dimensional vortex flow. As reported in [4], a facility for making these measurements has been designed, built, and calibrated. Some initial measurements were also reported, from which the overall structure of the flow field could be inferred, and this was found to agree with the conceptual picture developed from our water tunnel observations.

This paper presents the first detailed measurements of the three-dimensional flow associated with the inlet vortex. There are two main points that are addressed. The first is to show quantitatively that the circulation of the inlet and trailing vortices are (as hypothesized in [3]) essentially equal and opposite. The second is to define the circulation and the location (inside the inlet) of the inlet vortex for values of the pertinent nondimensional parameters which are representative of those occurring for actual aircraft, since this is a situation of strong practical interest. In addition to these points, further information about the vortical structure of these flows, obtained from water tunnel flow visualization, will also be described.

EXPERIMENTAL FACILITY AND EXPERIMENT DESIGN

All of the quantitative measurements reported were conducted in the M.I.T. Wright Brothers Wind Tunnel. A layout of the tunnel is shown in Figure 3. The tunnel is closed circuit, with an elliptical test section 3.05 m wide, 2.3 m high and 4.6 m long. During this investigation a 2.4 m wide ground plane was mounted 0.46 m above the bottom of the test section. The leading edge of this ground plane was rounded and drooped to avoid flow separation.

The mean velocity in the test section is controlled by either a variable pitch propeller, which can induce velocities up to 80 m/s, or an auxiliary fan (a large attic fan), which is suitable for speeds up to roughly 3 m/s. The propeller and fan controls, and the data acquisition system, are located in a control room adjacent to the test section. Further information is given by Markham [5].

The flow through the inlet was created by a three-stage centrifugal blower located outside the tunnel. This was designed with backward leaning blades so as to obtain as large a stable flow range as possible, in order to have flexibility in the carrying out of parametric studies. The inlet face average velocity, an important parameter of the experiment, was calculated from the measured pressure drop across a calibrated perforated plate in the inlet blower/duct system. In the experiments, the maximum

inlet velocity was 135 m/s, so that compressibility effects were not important. Further details of the construction and calibration of the facility for inlet vortex flow measurements are given in [4] and [6].

The inlet model used is a circular cylinder with no centerbody. The inside diameter was 0.15 m and the outside diameter was 0.2 m. The inlet lip was designed to have no separation over the range of conditions of interest, using the procedure developed by Stockman and Boles [7],[8], which yielded an inlet lip geometry composed of elliptical segments.

The nomenclature used to describe positions on and inside the inlet is that the theta (θ) coordinate refers to angular position around the inlet. In the crosswind configuration used, the inlet is at ninety degrees to the mean flow, $\theta = 0$ is upstream (at the "leading edge"), $\theta = 90$ is on the top of the inlet, $\theta = 180$ is at the rear, and $\theta = 270$ is at the bottom. These conventions apply for measurements on both the inner and outer surface of the inlet. The axial coordinate is measured along the inlet axis, with the zero location being at the inlet lip, and the radial coordinate is the radial distance from the axis of the inlet.

Although there is no difficulty in obtaining kinematic similarity between the parameters in the model test and in the actual situation, this is not so for dynamic similarity. In particular, the large size of an actual aircraft engine precludes exact Reynolds number scaling for practical model tests. For this reason, the inlet models were equipped with 1.5 mm diameter "trip wires", at ± 67 degrees. These prevented laminar separation or operation in the transition regime between subcritical and supercritical operation, where the flow depended strongly on small surface finish irregularities. When the model was operated with no flow through the inlet, the use of the trip wires produced static pressure distributions similar to those round a circular cylinder at the actual (full-scale) Reynolds numbers of interest. Description of the considerations associated with the use of the trip wires can be found in [4] and [6].

Two models were machined for the experiments, one of plexiglas and the other of aluminum. The former was used for flow visualization, and the latter for the quantitative measurements. It was constructed with an array of forty static pressure taps on its surface, as well as with other locations for instrumentation and traverse inside the inlet. Figure 4 shows the aluminum model on its stand, with the locations of the static pressure taps along the inlet. There are four taps at each location, equally spaced around the circumference. During testing, as will be described below, the inlet is rotated around its axis, so that detailed resolution of the flow can be achieved. The range of H/D covered by the measurements reported was from 1.0 to 2.0.

The measurements of inlet vortex strength for the inlet in crosswind in an upstream irrotational freestream were, in fact, made inside the

inlet. There were two reasons for doing this. First, if viscous effects are small, the circulation around the inlet vortex will be constant, not only outside, but also for some distance inside the inlet. More precisely, if there is a region in which the vortex core is surrounded by fluid which has the freestream stagnation pressure, and if the circulation is measured in this region, it will be the same no matter where one measures it. It was more convenient, therefore, to carry out the measurements inside the inlet, as described below. Several checks were made on whether the basic assumptions did in fact hold, including one measurement of the circulation around the inlet vortex at a location just below the inlet. These show that the measurements within the inlet were adequate. The second reason for taking measurements inside the inlet, which is a quite different one, is that this is the station where one really wishes to have the velocity data.

Several types of flow measuring probes were used in these experiments. In the crosswind tests, three-hole and five-hole probes were used inside the inlet to determine the magnitude of the velocity component needed to establish the circulation around the inlet vortex. The positions of these probes are shown in Figure 4. The measurements were made by rotating the inlet through 360 degrees in 11.25 degree increments. This yielded three-hole probe, Kiel probe, and wall static pressure data at 64 evenly spaced positions around the circumference. In order to calibrate the three-hole probe offset angle (the angle between axial and the probe normal), the inlet was run: 1) facing directly upstream, 2) at an H/D = 6 so that ground effects are negligible, and 3) at a low velocity ratio.

Five-hole probes were used to determine the velocity in regions of significant pitch angle. A prism five-hole probe was used to make nearly diametric traverses across the inlet, along the path indicated in Figure 4.

Measurements of the trailing vortex flow field were made at points on a grid, 3.3 (inside) diameters downstream of the inlet, using a hemispherical five-hole probe. Motorized horizontal and vertical traversers were used to position the probe at the desired points. The probe traverse set up in the wind tunnel is shown in Figure 5. This probe could be rotated in yaw and in pitch so that it could be maintained within the ± 30 degree

range of calibration.

The circulation measurements that were carried out on the inlet vortex at the locations beneath the inlet, were also done using a single slanted hot wire, rotated to the three different orientations. This probe was traversed in a contour to enclose the inlet vortex. Before carrying out the measurements, smoke flow visualization was used to determine that the flow angles incident on the probe were within an acceptable range.

Finally, the position of the core of the inlet vortex was obtained from smoke flow visualization also. A plane of laser light was used to illuminate the desired location in the (plexiglas) inlet. Significant scattering occurs only in regions of smoke concentration, so that the vortex core could be plainly seen. Since the vortex tended to wander slightly, the technique used to establish the position was to take a number of pictures (a dozen, say) and average the location.

REGIMES OF VORTEX FORMATION

Before describing the detailed velocity measurements, it is useful to give some description of the regimes in which the inlet vortex is present. Liu et al., [3], presented some initial measurements of this, but in Figure 6 we show not only further measurements done within the scope of the present investigation, but data of several other studies of this phenomenon. The points taken using the present facility (with two different ground plane configurations) are plotted as solid. The dashed line between the "Vortex" and "No Vortex" regimes has been drawn, somewhat arbitrarily, through these points.

Supplementary information about the particular experimental configurations used is given in Table I, but several points should be noted. First, the data from the P&WA and the GE test was obtained using scale models of aircraft engine inlets. Second, the angles between the mean flow and the inlet axis vary from 55 to 135 degrees. Third, the inlet model sizes did not vary by more than 50% from that used in the present study, so the Reynolds numbers were roughly comparable. None of the other tests made use of a boundary layer trip, however. Fourth, out of the available data, only that which is reported to have low values of velocity shear is plotted. Finally, the GE tests were done using an axial flow fan to induce the flow through the inlet, so the configuration was one with a turbomachine and with a centerbody.

In spite of these differences, it can be seen that all the data fall closely into a pattern. (The last point would not, in any case, be expected to make a difference.) The presence or absence of the boundary layer trip does not appear to make much difference as far as the vortex formation boundary is concerned. This was also found in tests with the cylindrical inlet [4], although it does not seem evident that the strength of the vortex is also independent of this feature. Within the data given,

TABLE I – STUDIES OF BOUNDARIES OF INLET VORTEX FORMATION

Symbol	Source	Conditions
▲	[4]	0.15 m cylindrical inlet, 90° yaw, thick ground boundary layer
●	present paper	same as above except thin ground boundary layer
△	P+WA Tests (Motycka et al, P+WA TDM 2414)	1/11 engine scale model, 135° crosswind, $Ro^* = 250$
▽	P+WA Tests	as above, $Ro > 100$
○	NGTE experiments Glenny ARC R+M 1114	0.15 m and 0.3 m, inlets, 55° crosswind provided by fan
◻	GE Tests	1/16 engine scale model, 60° crosswind provided by fan, turbofan inside engine model

$*Ro = \dfrac{Ue}{D} \dfrac{1}{\frac{\partial U}{\partial n}}$ is a measure of inlet shear, where n is normal to freestream

for the various angles, it also appears that angular orientation is not a strong influence, although it should be clear that this conclusion cannot hold all the way to angles close to zero (inlet pointing nearly straight into the flow). The general trend is that low values of H/D and high values of U_i/U_e tend to promote vortex formation. Although, again, this will not extrapolate all the way to zero free stream velocity, the limited data the authors have seen suggests that the velocity ratios at which the tendency for vortex formation again decreases (as U_i/U_e is increased) are too high to be of great relevance to the practical aspects of this problem.

The central point to be seen, then, is that the present set of experiments, although carried out on a simple inlet geometry at one value of inlet yaw angle, gives overall flow regimes that are in accord with experiments conducted with more complex (and more realistic) geometries and different angles of yaw. Hence it is felt that the results that appear below will not only be useful as far as shedding light on mechanisms, but also as far as providing information on the magnitudes of vortices to be expected in situations of practical concern.

VELOCITY MEASUREMENTS IN AN INLET IN CROSSWIND (Upstream Irrotational Flow)

As stated in the introduction, the features of the vortex system associated with an inlet in a crosswind have previously only been determined qualitatively, and the purpose of this study was to obtain quantitative data on this topic. Specific points to be addressed are the correspondence between the circulation around the inlet vortex and that around the trailing vortex, and the dependence of vortex circulation and position on the overall flow parameters, U_i/U_e, and H/D.

The measure of the vortex strength is the circulation. This can be obtained by (numerically) integrating the velocity around a closed contour enclosing the vortex. Flow visualization showed that the vortex core was located near the bottom of the inlet. A possible path that could be used was therefore a "D" shaped one, comprising a segment at constant radius, near the wall, and an approximately diametrical part, as shown in Figure 4.

The location for the measurements was chosen with several constraints in mind. These were: 1) to enclose only the vorticity of the inlet vortex (in particular, to avoid the streamwise vorticity which results from secondary flow in the boundary layer), 2) to position the probes for the circumferential part of the traverse close enough to the wall so that pitch angles are small (less than five degrees) and three-hole probes can be used, and 3) to avoid measuring at an axial location where circumferential

velocities due to potential flow effects in the inlet are significant*.
The axial location chosen was two diameters (0.3 m) from the lip, since at
this distance the potential flow effects would be negligible. A turbulent
boundary layer calculation gives a (conservative) estimate of the boundary
layer thickness to be 6 mm at this location (displacement thickness 0.7
mm). Potential flow calculations of the flow due to a vortex in an inlet
using the estimates of vortex strength developed in [4] suggested that at
this radial position the pitch angles would be within the desired range.
Therefore, for the circumferential measurements the three-hole and Kiel
probes were positioned at this location. The contour used was thus 174
degrees of a circular arc, with a radius of 0.92 of the inlet inner radius.

To show the main features of the circumferential velocity due to the
inlet vortex, the non-dimensional circumferential velocity, U_c/U_i,
along this contour is shown in Figure 7 for a condition of H/D = 1.5 and
U_i/U_e = 45. Although, as stated, it is only the circumferential
velocity between the angles of 191 and 17 degrees that is necessary for the
circulation calculation, the velocity field over the rest of the circumfer-
ence is of interest in developing a picture of the general flow field in
the inlet. The plot in Figure 7 represents the average of three runs at
this condition. Experimental uncertainty for this and other circulation
measurements was estimated at ± 10 percent.

A striking result is the existence of two areas of high circumferen-
tial velocity, indicating two vortical regions. One vortex, centered
roughly about 280 degrees, is the inlet vortex. Another vortex, however,
which has not been previously observed, and which has a circulation
opposite to that of the inlet vortex, is centered at approximately 135
degrees.

To complement these velocity measurements, lampblack flow visualiza-
tion was used on the inside surface of the plexiglas inlet. The results
are shown as Figures 8(a) and 8(b). As can be seen in the former, the
lampblack streaks originating at 270 degrees near the lip shift to roughly
300 degrees at two diameters from the lip so that the lower vortex moves in
a clockwise direction as it proceeds into the inlet. This is due to the
interaction of the vortex with the inlet wall, and can be thought of as
resulting from the velocity field of an image vortex. The lampblack traces

---

* Near the inlet lip, the flow has to turn into the inlet. The
streamline curvature brings with it a consequent cross-stream pressure
gradient and hence velocity non-uniformity (from 0 to 180 degrees). At
locations away from the lip inside the inlet, however, the velocity is
constant over the annulus (or would be, if there were no inlet vortex). As
one moves into the inlet from the lip, therefore, there must be significant
circumferential velocities associated with the redistribution of flow over
the annulus. Trying to measure the circulation in the presence of such
effects essentially means trying to take the difference of two large
numbers, and it is desirable to avoid such a situation.

due to the second vortex are shown in Figure 8(b). The streaks originate at about 150 degrees at the lip and move in a counterclockwise direction to about 145 degrees at the two-diameter location, so that this vortex has a smaller induced effect than the lower one.

A plot of the velocity components along the contour of integration is shown in Figure 9. The figure is a view looking into the inlet, with the freestream velocity coming from the right. The groundplane is not shown but it is below the inlet. It can be seen that by far the more important part of the circulation integration is from the circumferential velocity along the circular arc. This is in fact what one should expect from carrying out simple potential flow calculations of a vortex (or two vortices) in a circular cylinder, since the vortices are close to the boundaries and the region over which the velocities are large will be of the scale of the separation distance, and hence rather localized.

The validity about the assumptions concerning probe position can also be examined. The requirement that the probes be out of the boundary layer and at a location where the potential flow effects of the inlet have decayed correspond to a situation in which the stagnation pressure is constant and the static pressure shows only a small local depression due to the presence of the vortex. Figure 10 shows representative pressure distributions around the inside of the inlet (the conditions are $H/D = 1.5$, $U_i/U_e = 45$). The static pressure can be seen to be as desired; however, there are two regions of stagnation pressure defect. One region is near 100 degrees, outside the contour used for the circulation measurement, and is thus not of concern for these types of measurements. The other region, however, is near 300 degrees, and therefore does affect the circulation measurements.

The potential flow calculations imply, and flow visualization bears out, that these regions of lower stagnation pressure are due to the local radial velocities induced by the vortex. In other words, the radial flow induced by the vortices causes the boundary layer to accumulate on one side of the vortices; displaced in the clockwise direction for the lower vortex, and in the counterclockwise direction for the upper vortex, in accordance with the respective circulations of each.

After observing this type of behavior, some investigation was made of the situation at different radial positions. It was concluded that the 6 mm location would be adequate. The measured circulation of the vortex will, of course, be affected due to the influx of vortical fluid from the boundary layer into the inside of the contour. One can, however, make a crude estimate of the influx of vorticity and this leads to the conclusion that the effect is small. In addition, a stronger demonstration can be made by carrying out the measurements at a different axial location. This was done at a station two-thirds of a diameter upstream. While the measured circulation at this upstream location was slightly larger (7 percent), the differences were less than the estimated experimental

uncertainty. Hence, on both counts, this effect is not significant for the conclusions of the present study.

There was, however, a marked difference in one aspect of the velocity measurements at the two axial locations. This was a clockwise shift in the angular position of the peak circumferential velocity, of about twelve degrees for the lower vortex. The shift was less, about five degrees, and clockwise for the upper vortex. Both of these are consistent with the pattern seen during flow visualization as well as with potential flow estimation of the lateral drift of a vortex near a wall. The other aspect of the measurements at the upstream location was that the stagnation pressure defects were less, as one would expect, since the radial transport has had less time to act and the boundary layers are thinner at this location.

Although some parametric information will be given subsequently about the inlet vortex circulation, at this point, we wish to pursue only the verification of the hypothesis concerning the inlet vortex and trailing vortex circulation. We thus confine the present comments about inlet vortex circulation to stating that for the case at which we measured the trailing vortex (as described in the next section) the non-dimensional circulation was $\Gamma/U_e D = 7$.

We have discussed the rationale behind making the measurements of vortex strength inside the inlet. As a further check on the utility of this procedure, the circulation around the vortex was also measured outside of the inlet. The measurements were carried out at $H/D = 1.5$, $U_i/U_e = 45$ at two heights above the ground: 0.33D and 0.5D. The probe used was a slanted hot wire, operated at three orientations.

The flow in the area of interest is very strongly three-dimensional. To ensure that probe self-interference would not occur, smoke flow visualization was first used to give an indication of the velocity direction. The circulation contour was then traversed in three sections using an appropriate probe axis.

The results of the traverse showed that the circulation round the vortex was approximately 0.8 of that measured inside the inlet. There are several possible reasons for this, such as (small) background shear in the tunnel and experimental uncertainty involved in the measurement, and these are currently under investigation. The central point, however, is that to quite a good approximation the basic concept of measuring the vortex strength at the location of interest in the inlet does give direct information on the strength of the vortex between the ground and the inlet.

TRAILING VORTEX MEASUREMENT

The trailing vortex circulation was measured at a condition where a

strong inlet vortex was present; $H/D = 1.5$, and $U_i/U_e = 45$. The trailing vortex circulation was calculated from a velocity map taken at a plane downstream of the inlet, perpendicular to the direction of the mean flow. Smoke flow visualization showed that a plane approximately three outer diameters (four inner diameters) from the inlet axis was suitable for this. Again there were several conflicting constraints. It was desired to have a region of "freestream" flow between the trailing vortex and the ground boundary layer; this limited how far back the traverse plane could be. Against this, however, we wished to have a clearly defined trailing vortex for ease of measurement, and the rolling up of this structure took several diameters. After considerable trial and error, the three diameter location was established as the optimum choice.

The measurements were taken using a five-hole hemispherical probe. They represent a twelve second average of the measurements. This was necessary since time resolved measurements in the trailing vortex/wake region showed a low frequency oscillation of approximately 1/6 Hz. A repeatability study was therefore carried out using averaging times of six, twelve, eighteen, and twenty-four seconds. From this it was determined that twelve seconds would be adequate.

The cross flow velocity vectors obtained are shown in Figure 11. The velocity vectors are shown as seen looking upstream (towards the inlet). The trace of the inlet is also given in the figure. The region in the middle of the figure was not measured, but it is only the velocity vectors on a contour enclosing the vortex that is needed.

The circulation round the trailing vortex obtained from these measurements is very close to the same magnitude as that found for the inlet vortex, namely $\Gamma/U_e D = 7$. In addition, as can be seen from a comparison of Figures 9 and 11, the sense of the inlet vortex and trailing vortex circulations is opposite. Thus, as hypothesized, the inlet and trailing vortex are opposite in sign and closely equal in magnitude.

INLET CIRCULATION FAR FROM THE LIP

A central point of the above hypothesis is that the circulation round the inlet at locations far from the inlet lip would be small. This is certainly plausible, since the velocities on the outer surface of the inlet are on the order of U_e there. However, we can make the statement more quantitative using data on the static pressure distribution round the inlet. This is plotted in Figure 12, which shows curves of static pressure coefficient, C_p ($C_p = (P-P_{ref})/(P_t-P_{ref})$) on the inlet outer surface versus circumferential position, for axial locations ranging from 2.5 diameters to 0.17 diameters from the inlet lip. The conditions are the same as those for the inlet vortex and trailing vortex measurements, namely $H/D = 1.5$, $U_i/U_e = 45$. Figure 12 can be regarded as an extension of the data given by Liu et al. [3], to a substantially higher velocity ratio.

It is not the intent of this paper to present a general discussion of the features of the static pressure distribution. These have been examined in [3], where it was shown that the static pressure distribution at both high (as pictured here) and low values of velocity ratio could be interpreted quite well in terms of the interaction between an overall flow into the inlet and the inlet/trailing vortex system.

This applies to Figure 12 as well, but that is not the main reason for including the figure. We do this to show the contrast between the distributions near the lip and those at axial locations away from the lip, in particular the last two locations at 2.0 and 2.5 D. At these locations the static pressure coefficient has a magnitude of order unity and is roughly symmetric about $\theta = 0$. (This can perhaps be seen only crudely due to the scale in the figure; it does become apparent when one plots the data on an expanded scale.)

These two features of the static pressure distribution imply that the circulation is quite small. We can estimate the circulation at these axial locations using the measured static pressure distribution and neglecting the fact that there is a small component of flow along the inlet. (This will lead to an overestimate of the circulation, so our results will be in fact conservative.) In carrying out this calculation one also has to estimate where the flow separates at the rear of the inlet, but: 1) the static pressure distribution is such that one can make this estimate with a reasonable degree of confidence, and 2) the conclusion about the magnitude of the circulation is unchanged using any plausible estimate of separation location. Since the location of the minimum velocity is very close to $\theta = 0$, the non-dimensional (clockwise) circulation can thus be estimated as:

$$\Gamma/U_e D = \frac{1}{2}\left\{\int_0^{\theta_{sep+}} \overline{\sqrt{1 - C_p}}\, d\theta - \int_0^{\theta_{sep-}} \overline{\sqrt{1 - C_p}}\, d\theta\right\}$$

where the notation θ_{sep+}, θ_{sep-} denotes the estimated upper and lower separation locations at the rear of the inlet. For reference, at the 2.5 D axial station these are at $\theta = 101$ degrees and 237 degrees respectively-- the static pressure coefficient is virtually flat between these locations, varying by less than ± 0.02.

The result of this rough calculation is that the circulation round the inlet at a location far from the inlet is less than 0.2 $U_e D$. In other words, the circulation at these locations is almost two orders of magnitude less than that of the inlet vortex (or the trailing vortex), confirming another "piece" of the conceptual picture that we had developed of this phenomenon.

EFFECTS OF VELOCITY RATIO AND H/D ON VORTEX STRENGTH AND POSITION

To investigate the influence of velocity ratio, U_i, and inlet height to diameter ratio, H/D, on vortex strength and position, a limited

parametric study was done of the velocity field in the inlet. To show the influence of the height to diameter ratio, tests were carried out at H/D = 1.0, 1.25, 1.5, 1.75, 1.91 and 2.0, keeping a constant value of U_i/U_e = 45. To examine the effects of velocity ratio, tests were carried out at U_i/U_e = 4, 17 and 45, at a value of H/D of 1.0. (The velocity ratios of 4 and 17 were chosen since data had been previously taken [3] on the inlet surface static pressure distributions at these values.) The velocity measurements were made in the inlet at the axial station two diameters from the inlet lip.

Figure 13 shows the tangential velocity as a function of circumferential position for five different values of H/D: 1.0, 1.5, 1.75, 1.91, 2.0. To help figure clarity, the curve for H/D = 1.25 is not plotted, but it is virtually the same as that for H/D = 1.0. (This curve, as well as other data that is only referred to here, can be found in [9].) The figure clearly indicates that the circulation of the inlet vortex decreases in strength as the height to diameter ratio is increased. The change in shape of the curve also implies a qualitative change in the position of the vortex; this will indeed be seen below to be the case. What has in fact occurred, as can be seen by the broadening of the velocity distribution, is that the vortex at the higher values of H/D has moved away from the inlet wall.

The effect of decreasing the velocity ratio (at constant H/D) is shown in Figure 14. Decreasing the velocity ratio reduces the inlet vortex strength (this trend is similar to that observed with increasing H/D) but resulted in a shift of the position of maximum circumferential velocity in the opposite direction from that seen with increasing H/D.

The overall effect of these parametric changes on the vortex circulation is shown in Figure 15. This is a plot of the non-dimensional circulation, Γ/U_eD, obtained by numerically integrating the circumferential velocity component and the relevant velocity component along the diametral traverse, for all of the points at which data was obtained. The points for velocity ratio of 45 are shown as circles, those for ratios of 17 and 4 as a square and a triangle respectively.

The non-dimensionalization used in the figure is not the only one that could have been adopted. There are other possibilities using the inlet velocity and/or the inlet height. These were explored, and, when no clear advantage was seen, the parameter used in the figure was adopted because this is similar to the type of parameter that one would use to characterize the circulation about a wing, for example.[*] (There is, of course, the same information in any of the non-dimensionalizing schemes, because one

---

[*]It is not quite the same since the diameter used would be the outer diameter. However, since much of the data on inlet vortices has been reported using the inner diameter, we have kept this format. The ratio of inner diameter to outer diameter here is .75.

can go from one to the other if the values of H/D and U_i/U_e are given.)

The location of the core of the inlet vortex inside the inlet was determined using smoke introduced into the vortex near the ground. The results, based on the photographs that were taken, are presented in Figure 16. The location of the center of the core is felt to be depicted fairly accurately, however. The results for core size are likely to be somewhat of an overestimate because the larger of the smoke particles do not follow the streamlines very accurately and tend to move out of the core. An obvious feature is the large change in the position of the vortex between H/D = 2.0 and the other values of H/D for a velocity ratio of 45. This is consistent with the qualitative change in the nature of the circumferential velocity profile.

STRUCTURE OF THE VORTICITY FIELD

It is clear that the inlet vortex flow field is quite complex. Because of this, it appears to be helpful to try to infer some of the overall features of the vortical structure that is associated with this flow field. In doing this, we emphasize that we are not concerned here with a detailed description of the structure of the turbulence or of the flow in the vortex core. What we mean, rather, is the vorticity field that is associated with the mean flow. It is an appreciation of this latter that is the first step to an understanding of the general phenomena of interest. The description that follows has been obtained not only from the velocity measurements that have been presented, but also from some flow visualization experiments that were carried out in a water tunnel, and these will be discussed where appropriate.

Effect of Velocity Ratio on Vorticity Field

As a framework for describing the vorticity field, let us consider the flow regimes encountered with an inlet operating near a groundplane as the ratio of inlet velocity to upstream velocity is increased. The inlet is in crosswind in a flow that is uniform far upstream.

With no inlet velocity, $U_i/U_e = 0$, the inlet is essentially a semi-infinite cylinder. There are vortex layers shed from the top and bottom of the inlet and from the end of the inlet. The vortex filaments in these layers are shown schematically in Figure 17(a). They are depicted as straight for simplicity, although it is recognized that this will not be the case in the actual situation, where there could be significant deformation and thus formation of streamwise vorticity.

As the velocity ratio is increased to a low value (between one and ten, say, for typical aircraft inlet H/D), the situation will change. There will be two trailing vortices. The vorticity in these trailing vortices is produced in the boundary layers on the outside of the cylinder. Flow visualization shows that, near the inlet lip, the fluid in the

boundary layers on the top and bottom of the inlet is sucked into the inlet. Since the fluid particles go into the inlet, and since vortex lines are never cut, the vortex lines must be as shown, going into the inlet.

The streamlines are sketched at the left. The upstream motion in this regime is very localized near the lip, and is not shown.

As the velocity ratio increases, the trailing vortex system shifts counterclockwise, as indicated in Figure 17(c). The upper vortex also increases in diameter and the lower one decreases. The circulation around each vortex also increases.

As the velocity ratio is increased still further, the lower vortex shifts abruptly to attach to the ground, forming the inlet vortex (Figure 17(d)).

This shift was examined in detail in water tunnel experiments. The actual circumstances were that as the velocity ratio was very gradually increased, the two trailing vortex structures would become increasingly unsteady and the lower vortex would intermittently attach to the ground. Then, as the velocity ratio was increased slightly more, a strong, stable, inlet vortex system would suddenly appear. Increasing the velocity ratio still more resulted mainly in a decrease in the core size, as might be expected from consideration of the balance between convection and diffusion that occurs in the core.

The abruptness of the transition between the two states was in fact suggested by Marble [10] from consideration of the kinematics of trailing vortices in an inviscid fluid. His basic argument was that the lower trailing vortex cannot simply shift downwards until it touched the ground at some far downstream location, with the point at which it touched then moving gradually upstream as velocity ratio increased. Rather, once it had touched the ground, the high (infinite for a line vortex!) induced velocities would result in a very rapid motion of this point, initially at right angles to the upstream flow and then upstream, leading to the formation of the inlet vortex configuration.

As stated previously, although Figure 17 has been drawn from the flow visualization experiments, it is to be regarded only as a schematic, and there is one point which should be mentioned in this context. The streamlines in Figure 17(d), for example, are shown as implying particle motion downstream, but this is not true for all the flow in the trailing vortex. At the high velocity ratios, the low stagnation pressure flow in the center of the core of the trailing vortex flows upstream and into the inlet over a distance that is an appreciable fraction of the inlet diameter. This strong upstream flow again emphasizes that the vortex filaments must thread inside the inlet, and it is consistent with the existence of the second region of high circumferential velocity that was found inside the inlet.

The transition from an inlet vortex to the two trailing vortices when the velocity ratio was decreased also occurred quite abruptly. Waves first appeared on the core of the inlet vortex and then, as the velocity ratio was lowered past a critical point, the vortex was shed downstream and the two trailing vortex systems appeared.

Some Comments on the Topology of the Vortex Lines

In Figure 2 we presented a very simplified picture of the connection between the inlet vortex and the trailing vortex. This was developed from arguments about the solenoidality of the vorticity field. We now return to this point and describe, in somewhat more detail, the overall pattern of the vortex lines inside of and on the inlet.

To do this, we refer to Figure 18. The segments of the vortex lines at A form the inlet vortex, with a sense of rotation as indicated. These vortex filaments thread into the inlet (as at B) where they induce the region of high circumferential velocity near the bottom, inside the inlet (e.g., near 300 degrees in Figure 7).

The vortex filaments near C, also inside the inlet, are those which induce the high circumferential velocities near the rear, inside the inlet (e.g., near 140 degrees in Figure 7). Vortex lines cannot end in the fluid or on a solid stationary surface and they must thus either go to infinity or join up at some downstream location. For purposes of this discussion, it does not really matter which, and we have thus not shown this aspect of the flow. The central point is that these are regarded as having essentially equal and opposite circulations.*

The vortex lines from C must come out the front of the inlet. (Note that when we state that the vortex lines "come out" of the inlet, the reference is to the sense of the vorticity vector and not to the fluid velocities. The latter are, in fact, into the inlet in the region that we are describing.) This is shown near D in the figure. The origin of this vorticity must be in the boundary layer on the inlet, since this is the only place in which viscous forces are acting. The vortex filaments are therefore shown lying along the inlet. The flow visualization studies show that the flow separates from the rear of the inlet [6], and that it

---

*It is clear that because of the no-slip condition, the net (area integral) component of vorticity in the axial direction inside the inlet must be zero. This is not, however, what we mean. We are referring to the vorticity that is convected into the inlet (or produced during the convection), rather than that produced very near the walls by viscous forces acting within the inlet. For example, the net axial vorticity in the boundary layer between 5 and 190 degrees is closely equal and opposite to that in the inlet vortex, but it is only the latter that we are discussing here.

is this separated flow that is associated with the trailing vortex. In addition, the static pressure distribution shown in Figure 12 implies that the circulation around the inlet increases over a distance on the order of one to several outer diameters - in other words not abruptly on the length scale of a diameter. These two ideas lead one to draw the trailing vortex structure as a distribution of vorticity rather than a concentrated vortex line. This is shown schematically in the Figure at E, for the vortex filaments on the rear surface of the inlet and at F for the trailing vortex, although there will be a strong tendency for the latter to wrap roll up as one proceeds in a downstream direction.

Figure 17 does show the answers to several questions concerning the topology of the vortex lines in and on the inlet. However, it by no means resolves all the features of this complicated flow. For example, we have only shown the trailing vortex filaments that are associated with the net circulation about the trailing vortex. On a more detailed level, there should also be trailing vorticity, not only from the separation line at the rear of the inlet, but also from the separation line that is present near the bottom of the inlet. The trailing vorticity at the shed into the flow at this latter position will be of opposite sign than that shed at the former, and the details of the interaction between this vorticity and that shed from the upper part of the inlet have not at all been addressed here.

SUMMARY AND CONCLUSIONS

1. Detailed measurements and flow visualization have been carried out for an inlet operating in crosswind. The purpose was to obtain quantitative information on the structure of the three-dimensional flow field associated with an inlet vortex.

2. The studies were made over a range of height to diameter ratio, H/D, and velocity ratio, U_i/U_e, so that the flow regimes encountered varied from those in which a strong inlet vortex and a trailing vortex were present, to those in which no inlet vortex existed, but two counter-rotating vorticies trailed from the inlet.

3. For a condition where a strong vortex was present, measurements were made of the circulation around the inlet and the trailing vortices. It was found that their circulations were approximately equal and opposite. This had been hypothesized previously based on a conceptual picture of the inlet vortex/trailing vortex system.

4. Also for this condition, the velocity measurements and the flow visualization both showed that there was a second region of high vorticity inside the inlet (in addition to the inlet vortex). This was located at roughly "two o'clock" looking into the inlet.

5. It appears that the axial vortex filaments in this region of high

vorticity are a continuation of the vortex lines that are associated with the trailing vortex. The vortex lines in this region thus come out of the inlet, around the lip, and trail downstream.

6. Flow visualization studies were also made of the transition between the inlet vortex/trailing vortex configuration and the flow regime with two trailing counter-rotating vortices. It was found that this transition is not gradual (as a function of U_i/U_e, say) but occurs abruptly at a critical value of this parameteer. During the transition, the lower counter-rotating or trailing vortex moves downward to become the inlet vortex.

7. A limited parametric study was carried out to quantitatively define the changes in vortex strength and position as H/D and velocity ratio U_i/U_e are varied. Increasing H/D has a qualitatively, but not quantitatively, similar effect to decreasing U_i/U_e.

REFERENCES

1. Younghans, J.L. and Paul, D.L., "Considerations in Inlet/Engine Integration," ch. 13 in The Aerothermodynamics of Aircraft Gas Turbine Engines, edited by G.C. Oates, AFAPL-TR-78-52, Air Force Aero Propulsion Laboratory, 1978.

2. Motycka, D.L., "Ground Vortex Limit to Engine/Reverser Operation," ASME Journal of Engineering for Power, Vol. 98, 1976, pp. 258-266.

3. De Siervi, F., et al., "Mechanisms of Inlet Vortex Formation," Journal of Fluid Mechanics, Vol. 124, 1982, pp. 173-207.

4. Liu, W., Greitzer, E.M., Tan, C.S., "Surface Static Pressures in an Inlet Vortex Flow Field," ASME Paper 84-GT-201.

5. Markham, J.R., "The MIT Wright Brothers Wind Tunnel and Its Operating Equipment," SAE Journal (Trans.), September 1941.

6. Shin, H.W. and Shippee, C., "Quantitative Investigation of Inlet Vortex Flow Field," MIT Gas Turbine and Plasma Dynamics Laboratory Report No. 109, to be published 1984.

7. Boles, M.A. and Stockman, N.O., "Use of Experimental Separation Limits in the Theoretical Design of V/STOL Inlets," AIAA Paper No. 77-878, 1977.

8. Stockman, N.O. and Farrell, C.A., "Improved Computer Programs for Calculating Potential Flow in Propulsion System Inlets," NASA TM-73728, 1977.
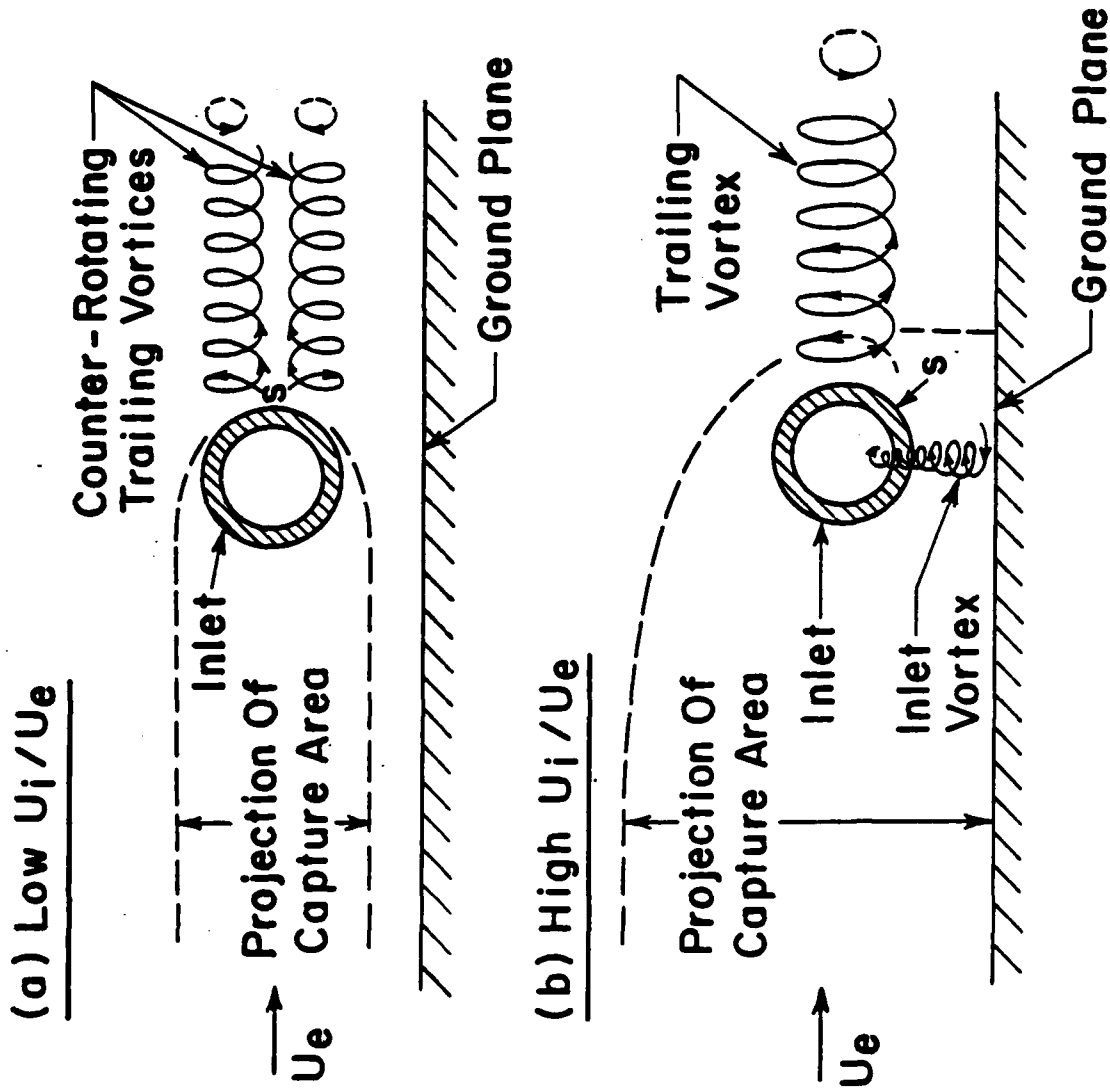
9. Marble, F.E., Personal Communication, 1983.

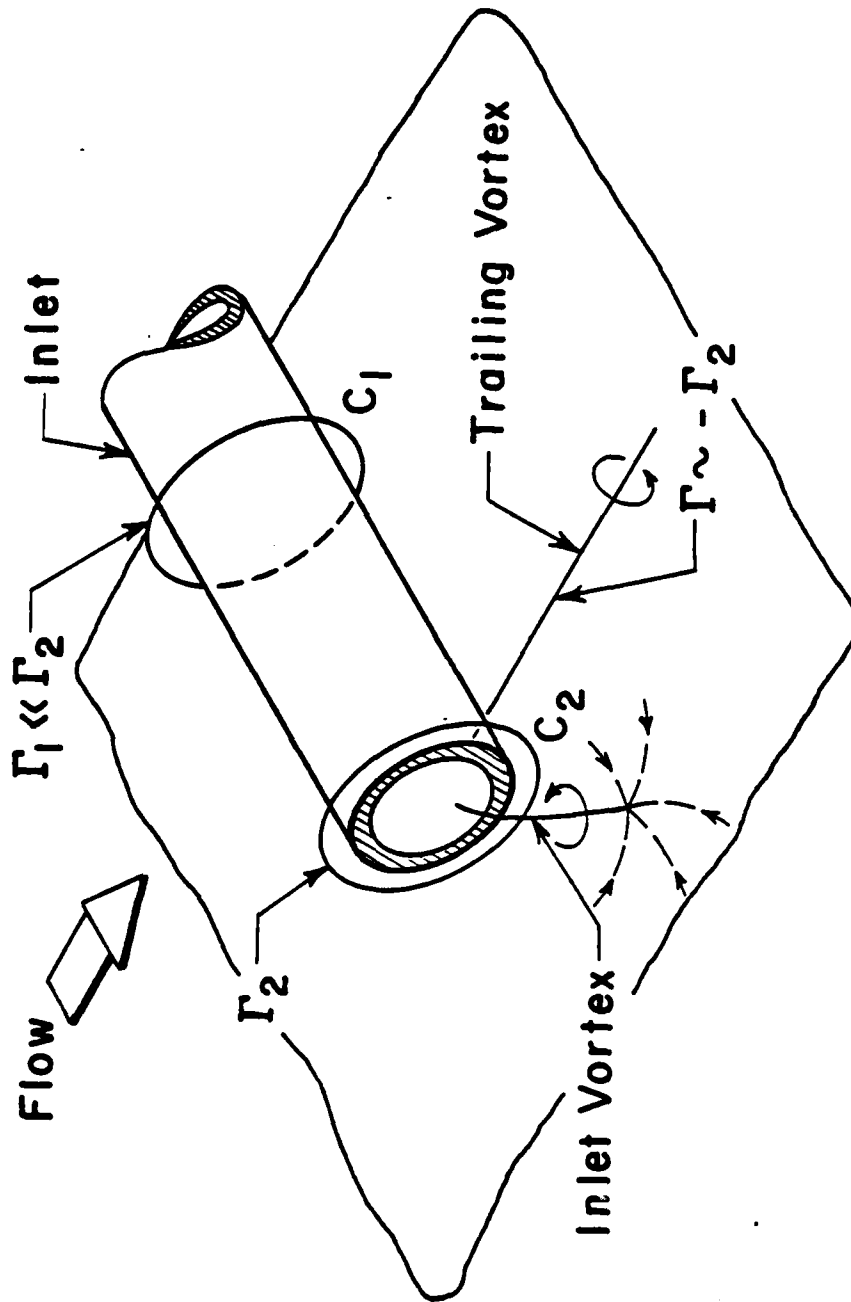Figure 1: Flow Regimes as a Function of Velocity Ratio

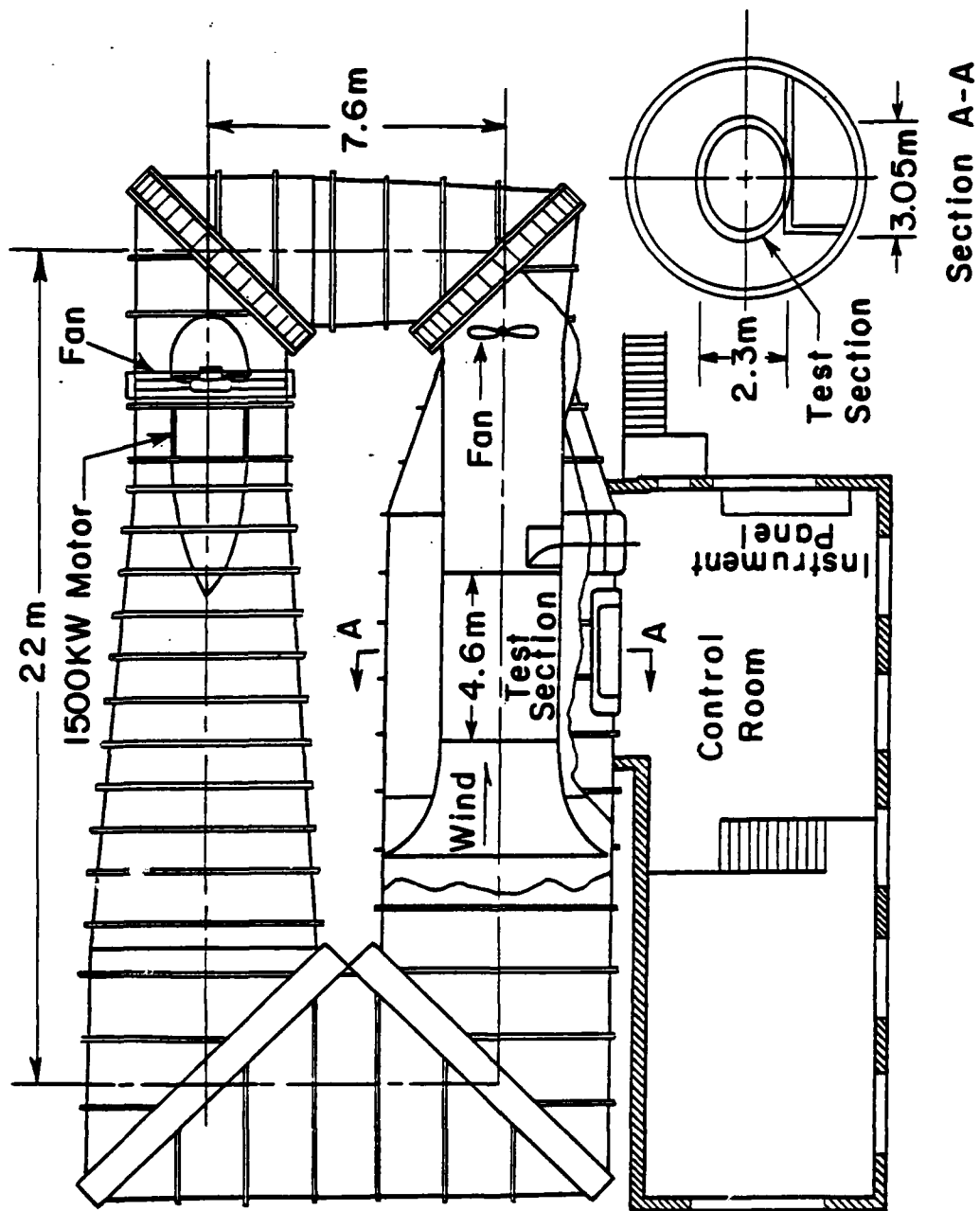Figure 2: Schematic of Vortex Lines in Inlet and Trailing Vortices

65

Figure 3: Layout of MIT Wright Brothers Wind Tunnel

Pressure Tap
Locations (9)

A ← 30cm From Inlet Tip

8 6

9 7 5 4 3 2 1

H

A ←

Inside Circulation
Measurement Station

Cylindrical
Stands

Inlet And Support

D; 15cm Inside Diameter

Path Used For
Circulation
Measurement

Five Hole Probe
Traversing Probe

T ; Three Hole Probe
K ; Kiel Probe
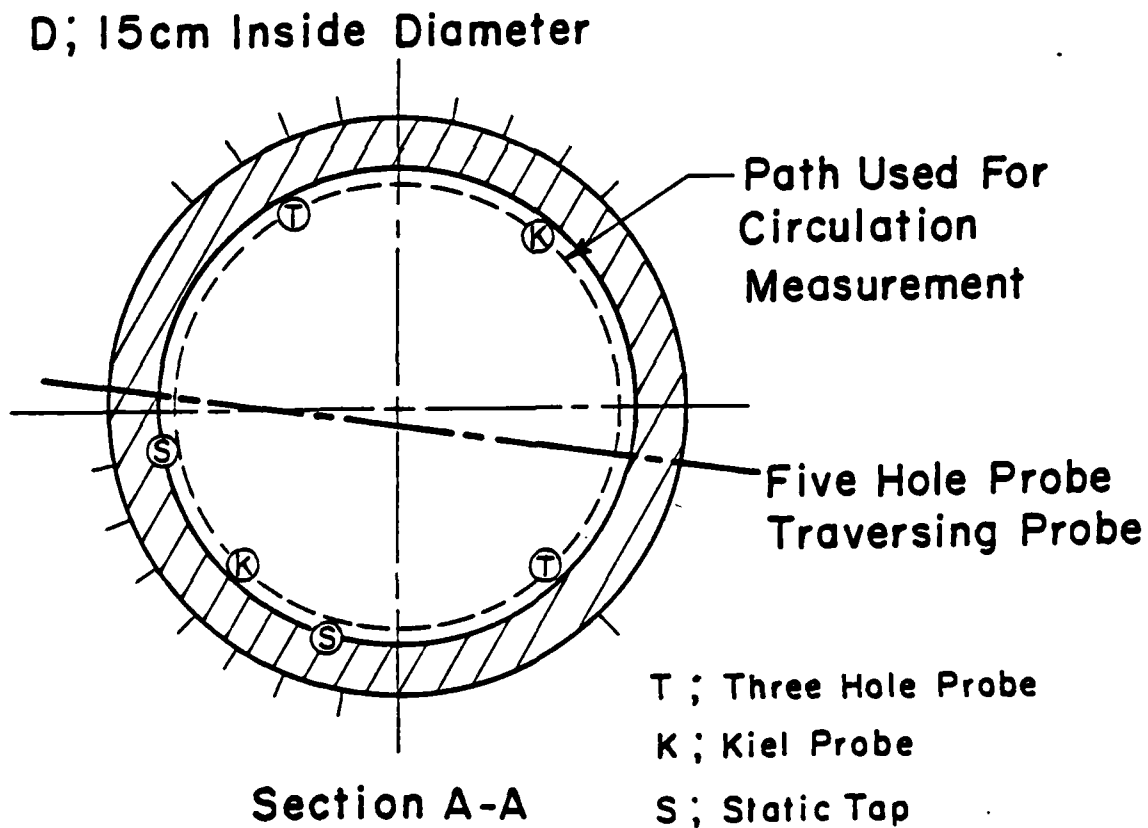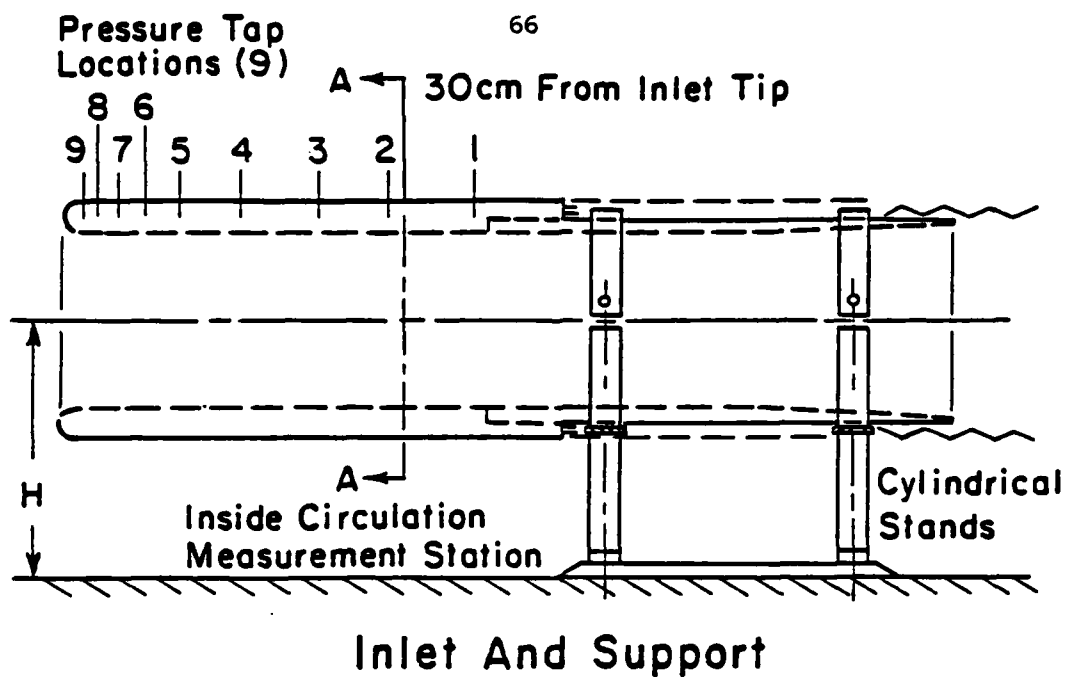
Section A-A

S ; Static Tap

Figure 4: Inlet Model (with measurement stations shown) and Location of
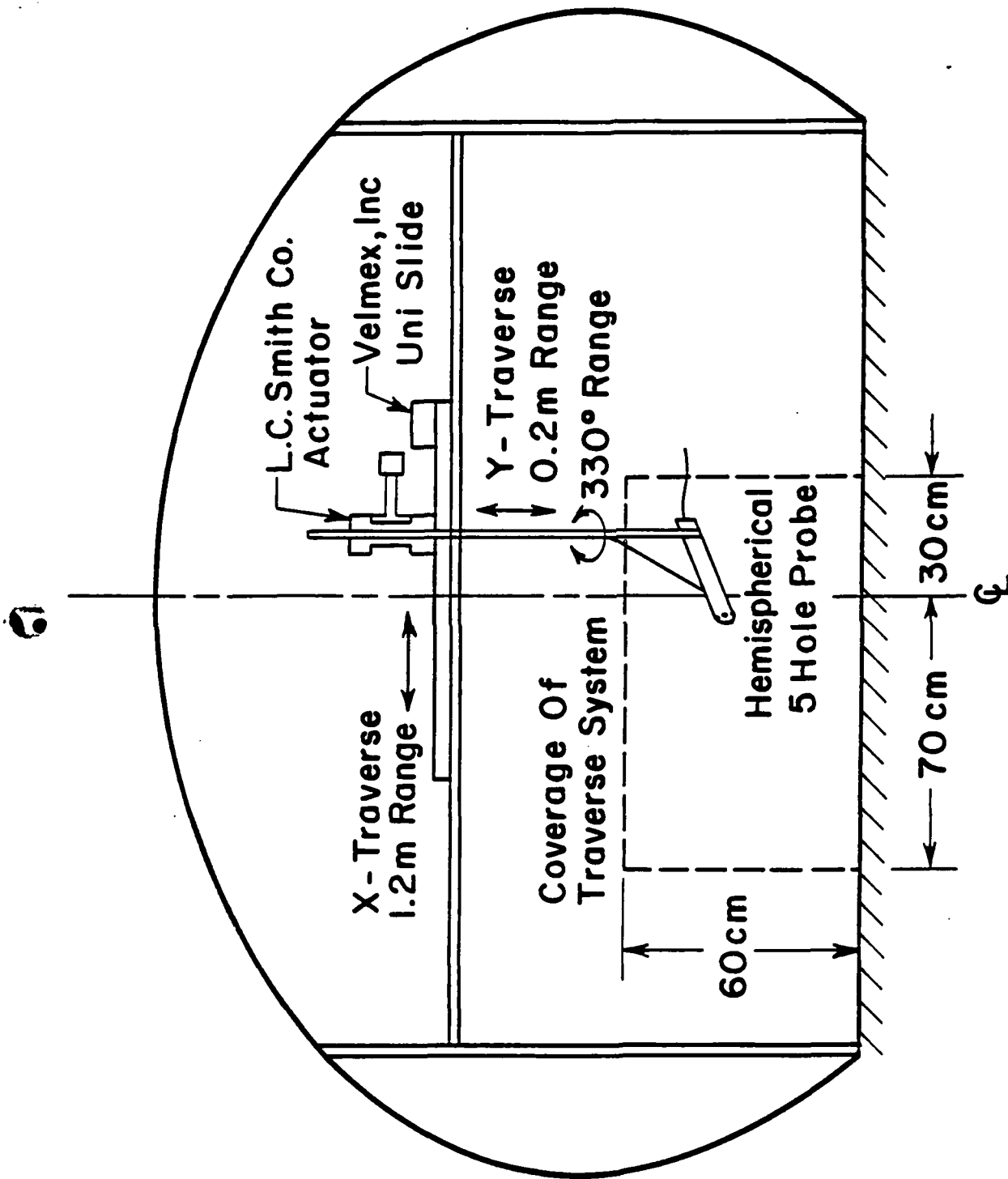Path Used for Circulation Measurement
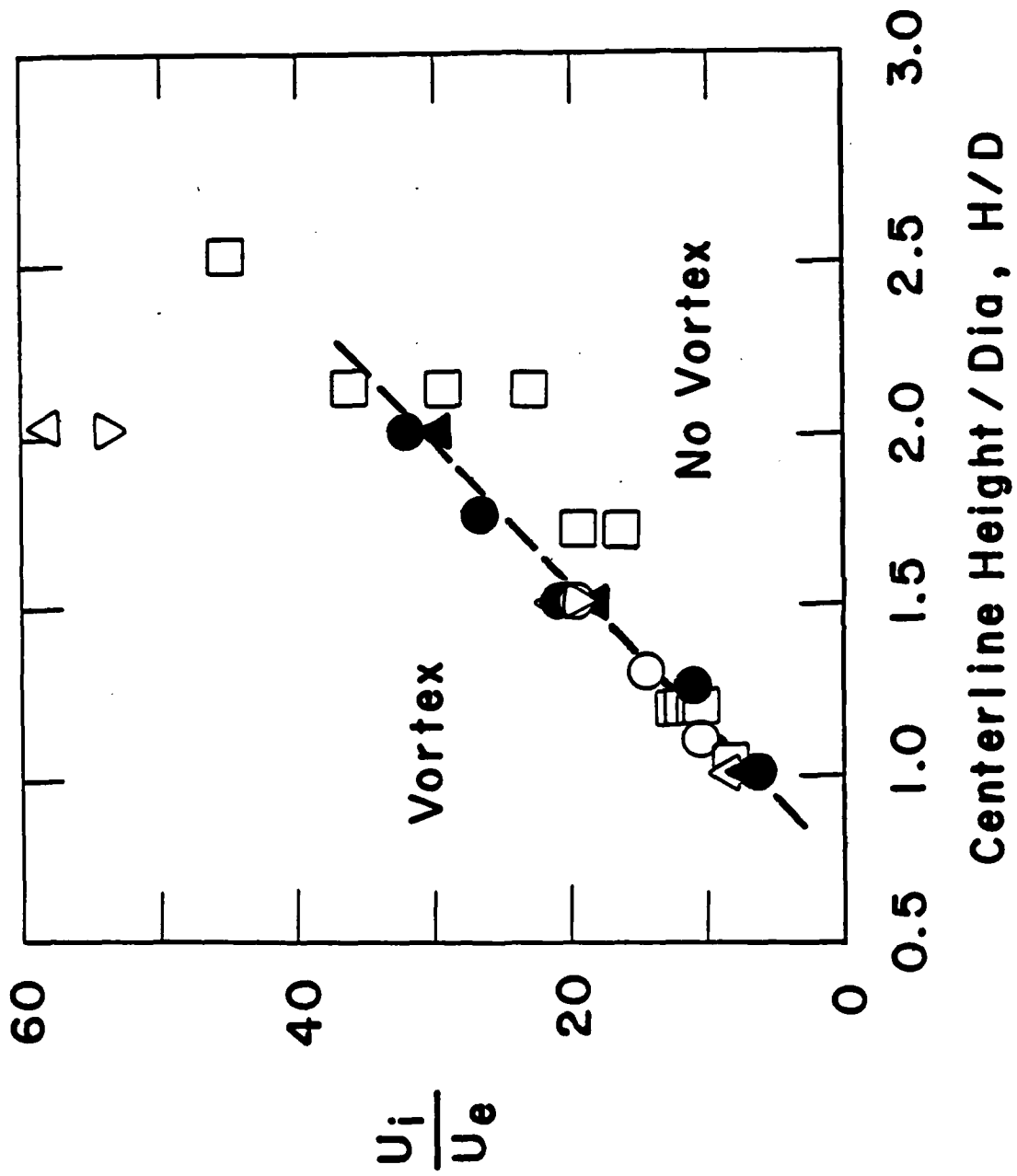
Figure 5: Traverse System for Trailing Vortex Measurement

Figure 6: Boundaries Between Vortex and No Vortex Flow Regimes
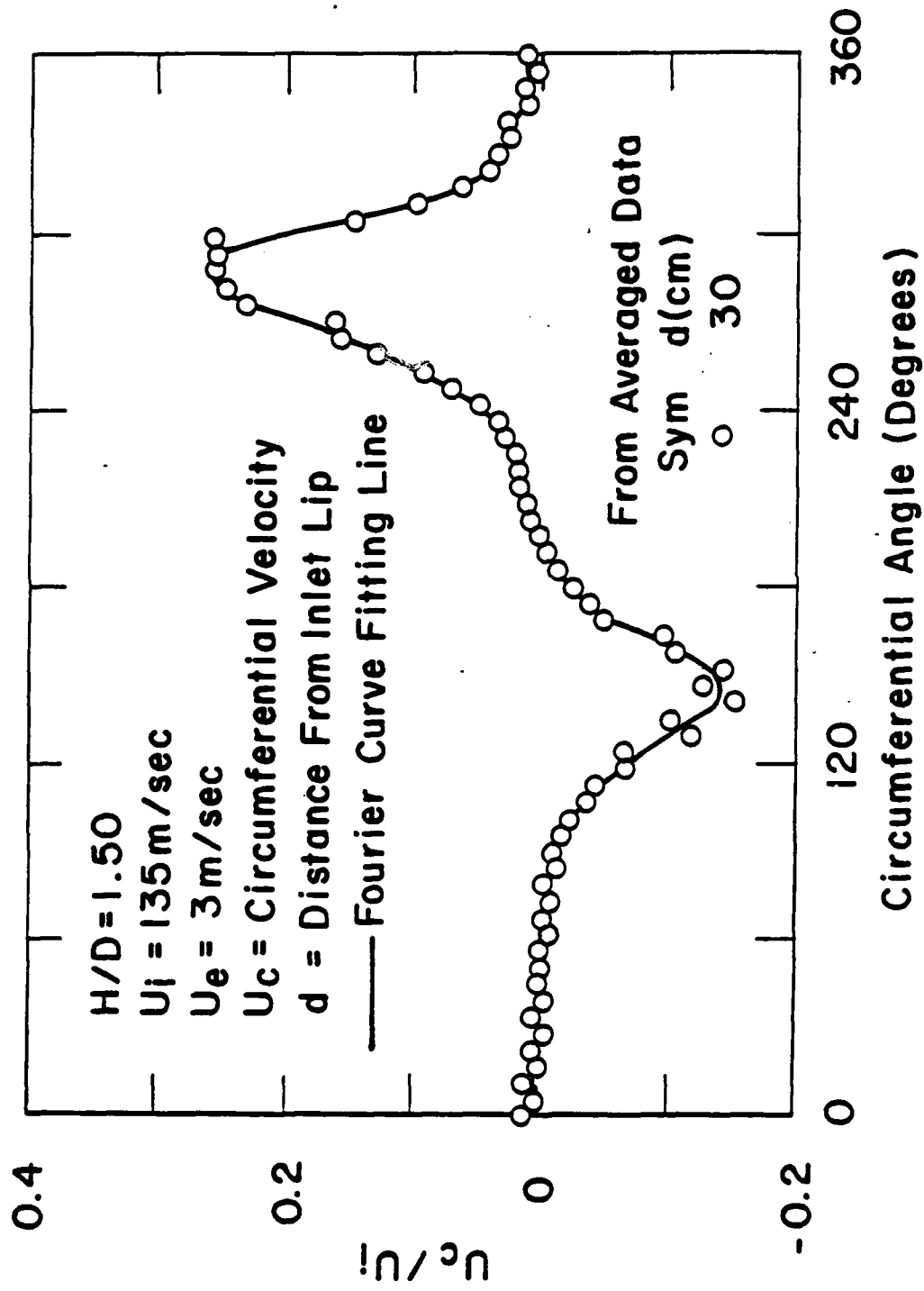(for key refer to Table I)

69

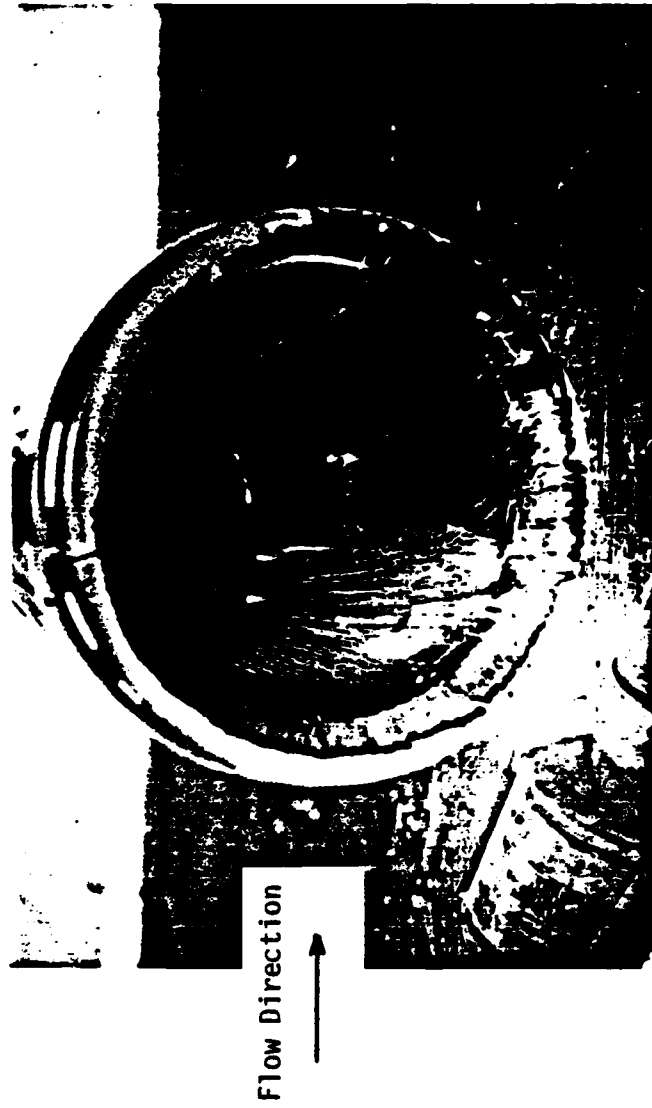Figure 7: Circumferential Velocity Distribution Inside Inlet

Inlet Lip

(a) Flow pattern at 0 deg. inside inlet.

Inlet Lip

(b) Flow pattern at 180 deg. inside inlet.

Figure 8: Lampblack Flow Pattern Inside Inlet

Flow Direction

(c) Flow pattern looking into inlet

Figure 8 (cont.): Lampblack Flow Pattern Inside Inlet

3 Hole Pitot Tube No. 1, 2
And 5 Hole Cross For Meas.
0.6cm From Wall, 30cm
From Inlet Lip.

H/D = 1.50
U_i = 135 m/sec
U_e = 3 m/sec

Vector Scale;
12 m/sec
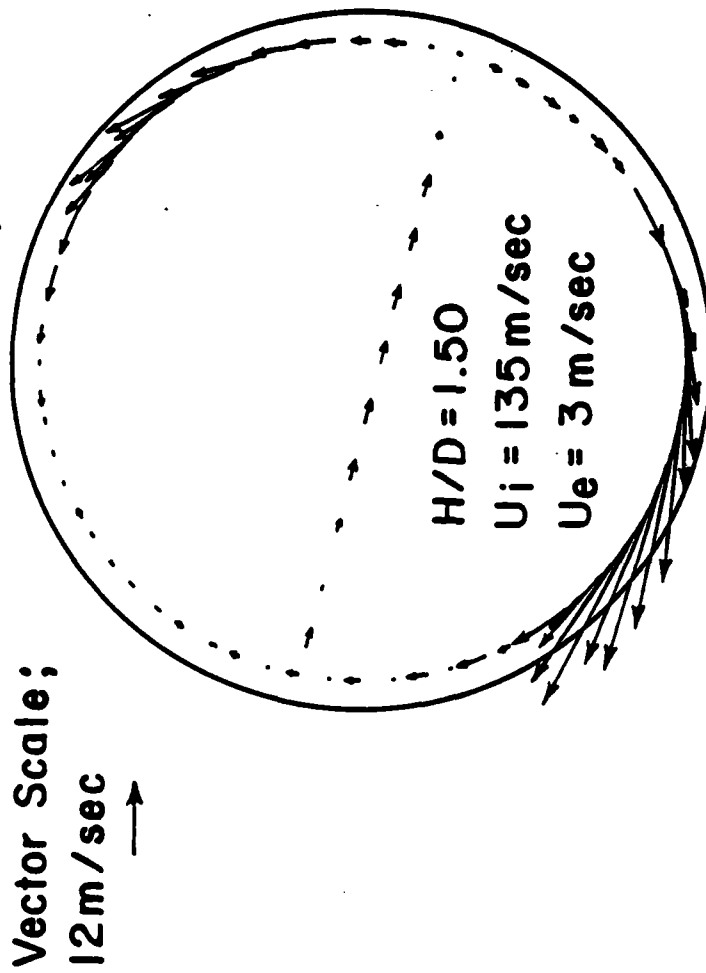
Figure 9: Cross Flow Velocity Vectors Along Path Used for Circulation Measurement
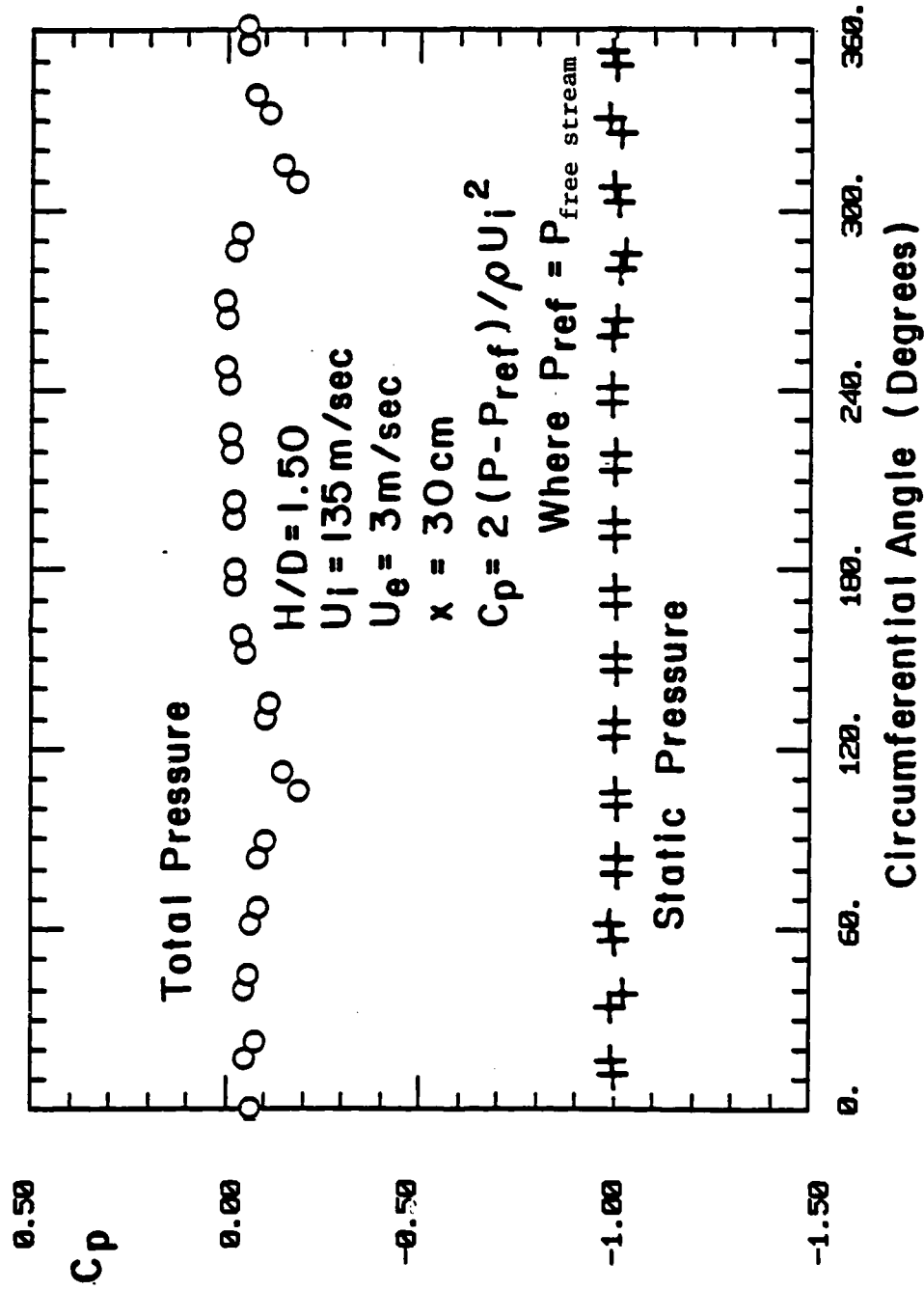
Figure 10: Total and Static Pressure Distributions at Vortex Measurement Station
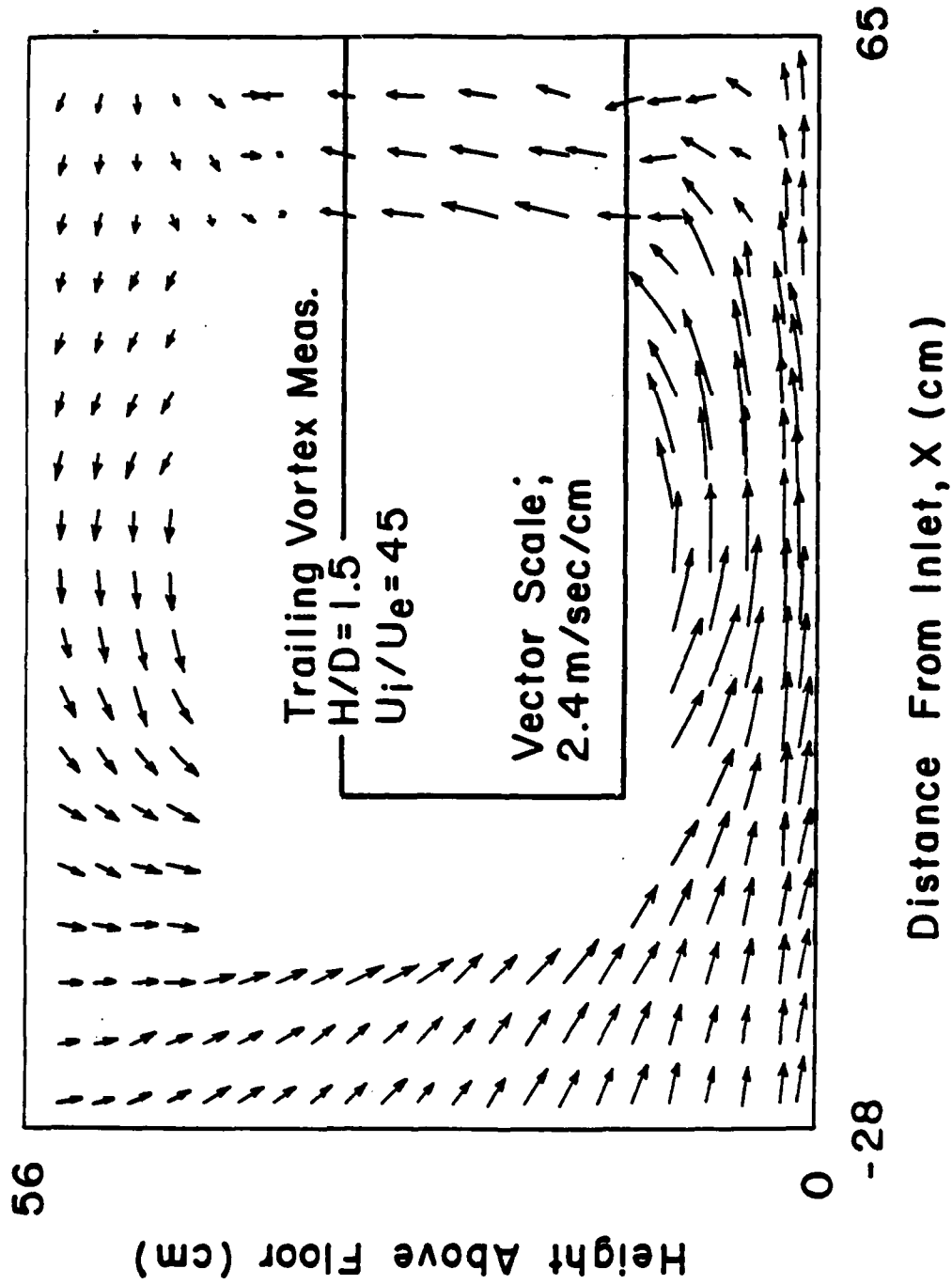
Figure 11: Cross Flow Velocity Vectors in Trailing Vortex Flow Field
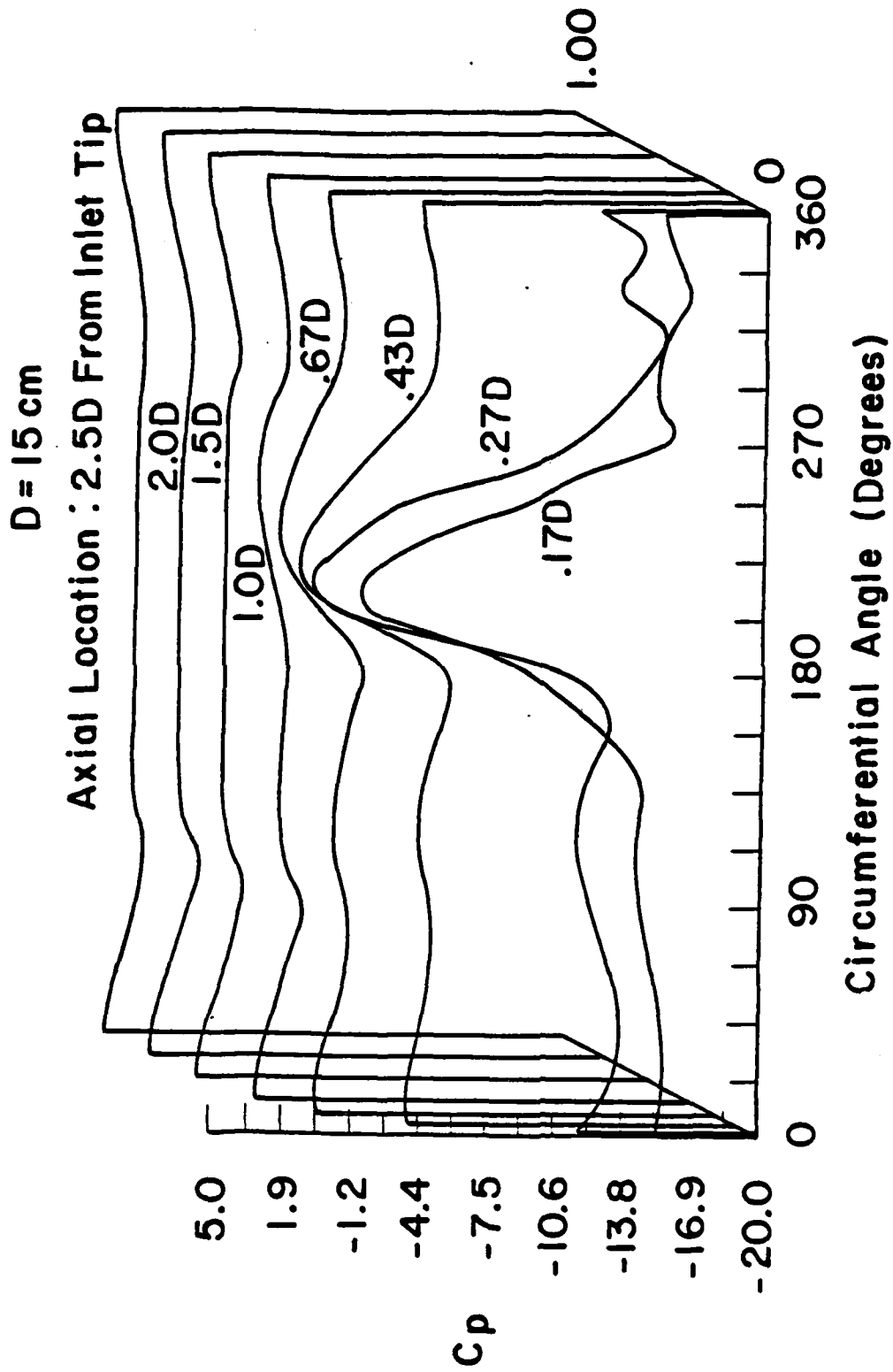
Figure 12: Static Pressure Distributions on Inlet Surface
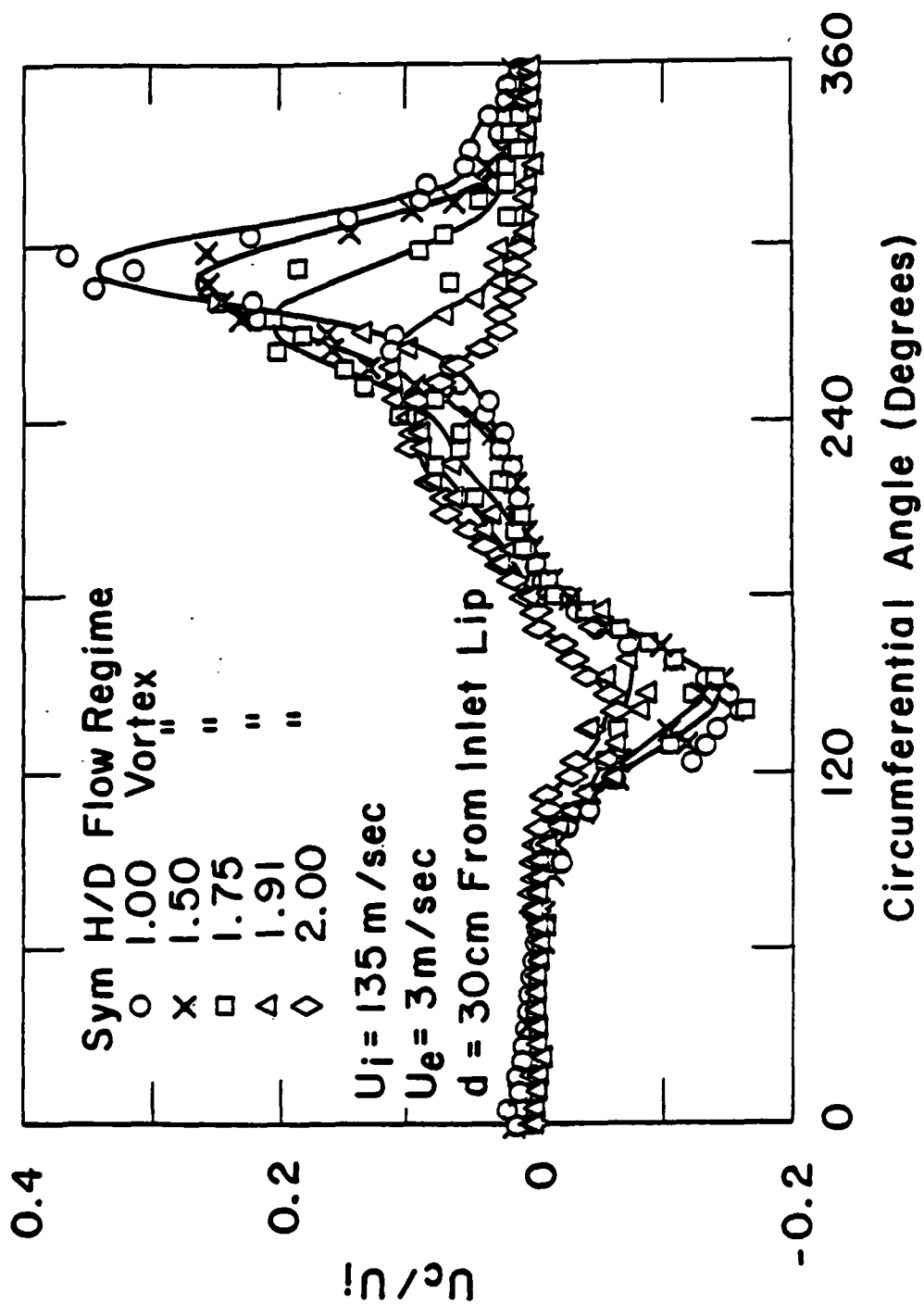
Figure 13: Dependence of Circumferential Velocity Distribution on Height to Diameter Ratio, H/D
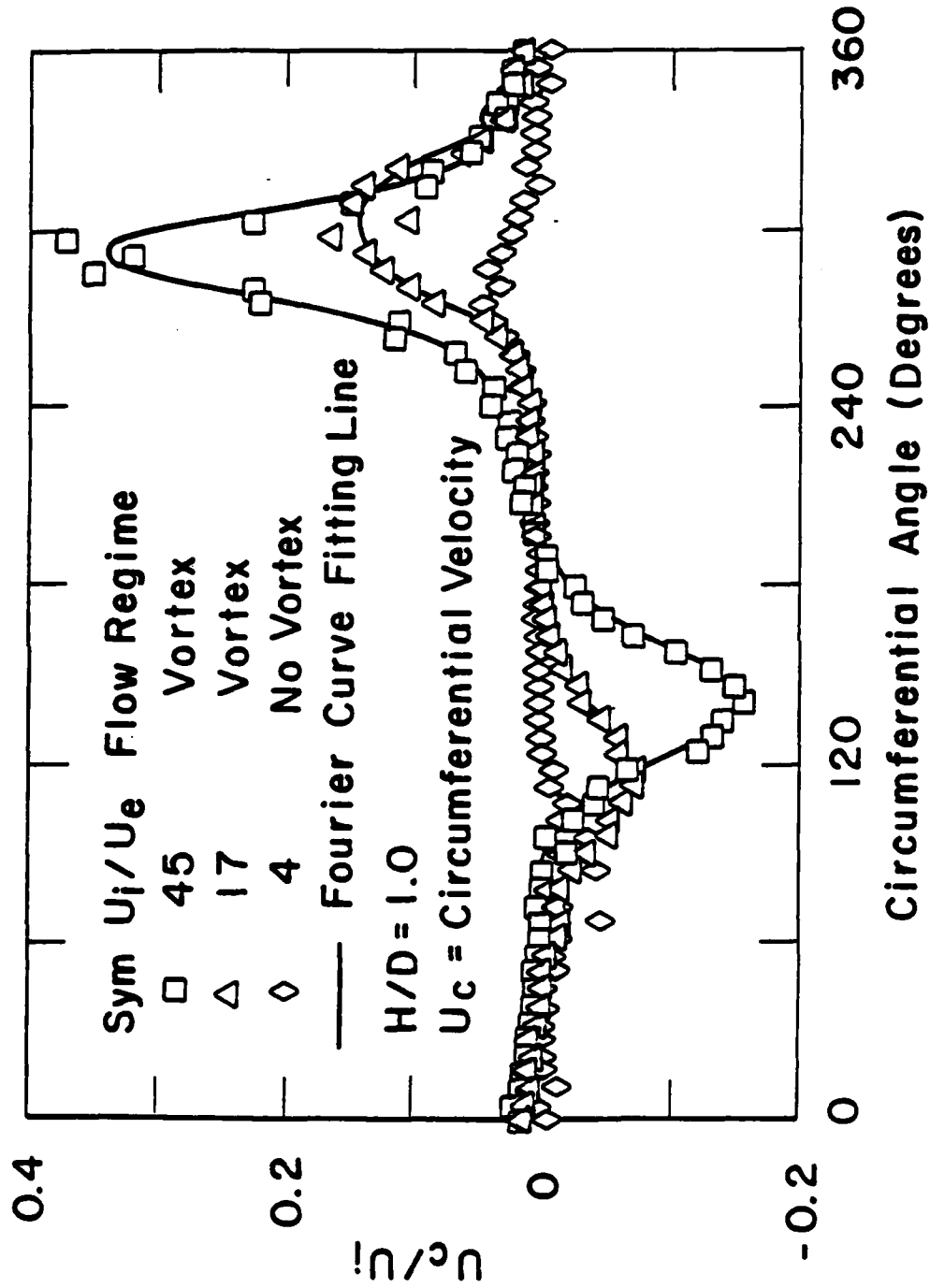
Figure 14: Dependence of Circumferential Velocity Distribution on Velocity Ratio, U_i/U_e
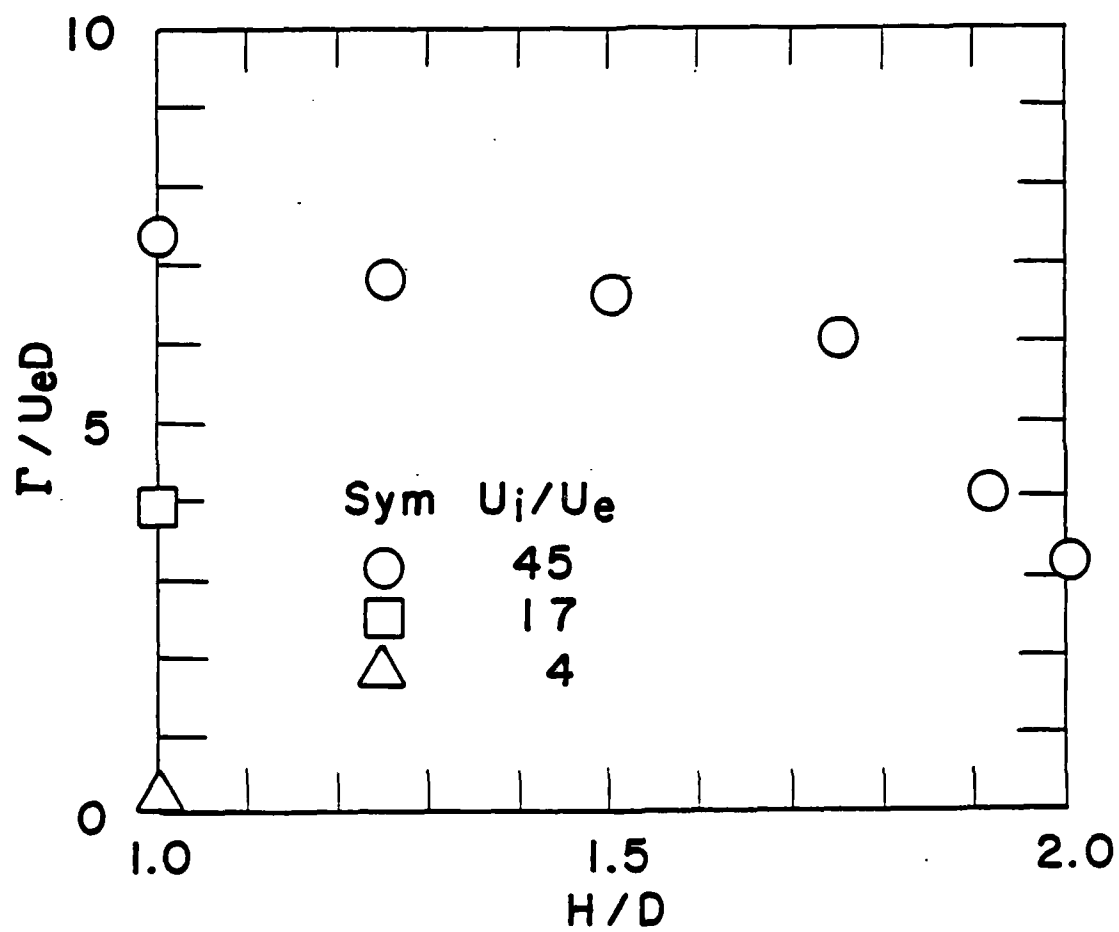
Figure 15: Non-Dimensional Inlet Vortex Strength

Sym	H/D	U_i/U_e	d/R
○	2.0	45	**0.3**
△	1.5	45	**0.2**
□	1.25	45	**0.3**
⬡	1.0	45	**0.2**
▽	1.0	1.7	**0.4**
◇	1.0	4	—

Where d is "Core Size"
R = 7.5cm
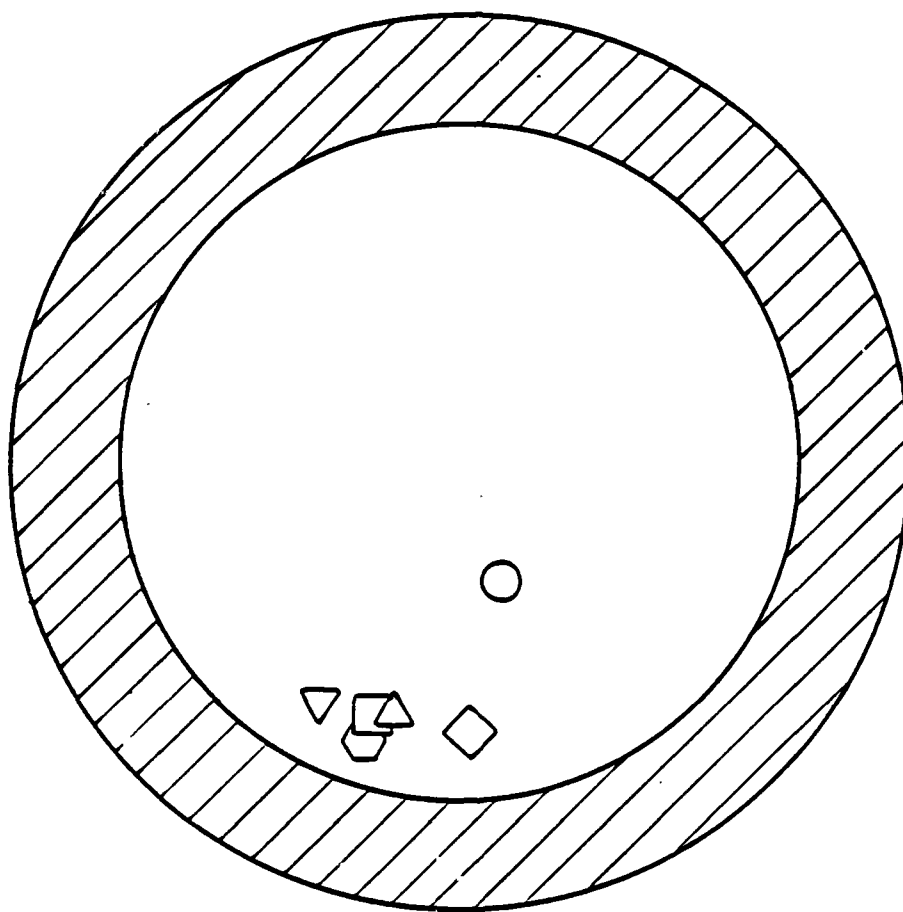
Figure 16: Vortex Position at Measurement Station
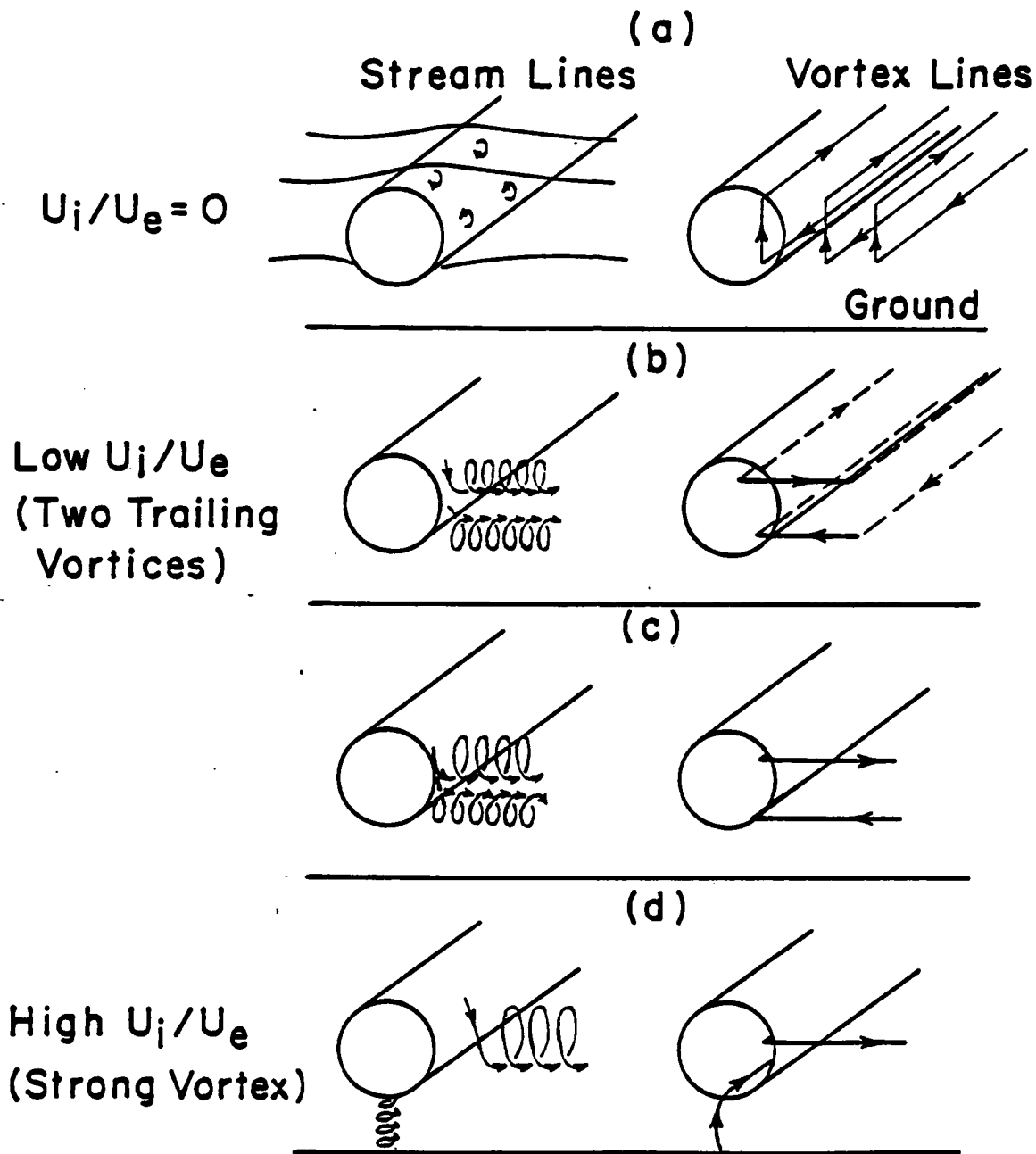
Figure 17: Changes in Vortex Field Structure as a Function of Velocity Ratio
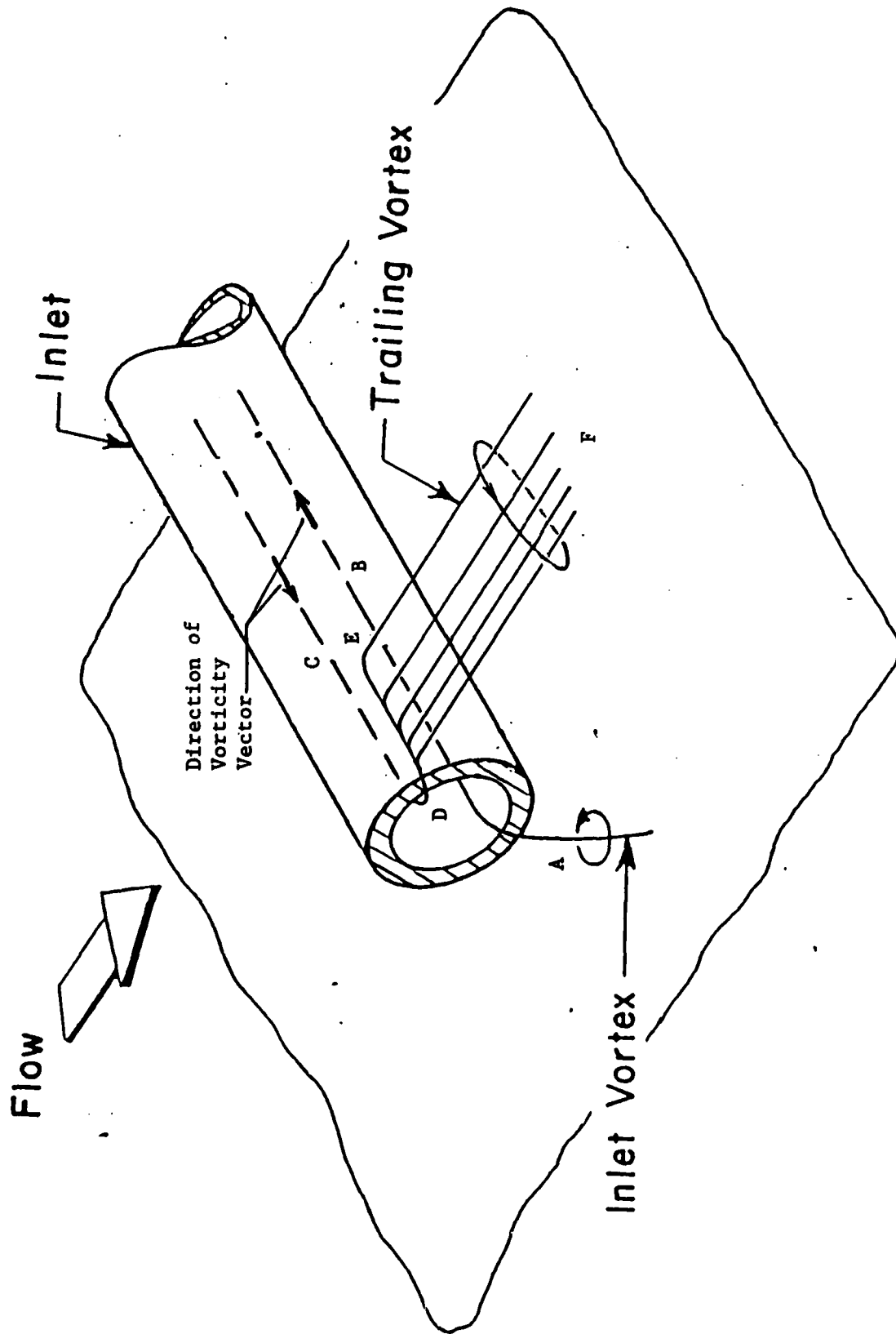
Figure 18: Sketch of Inlet and Trailing Vortex System Showing Connection
Between Vortex Lines Inside of and Outside of the Inlet

TASK IV: INVESTIGATION OF DISCRETE-BLADE AND THREE-DIMENSIONAL FLOWS

IN HIGHLY LOADED TURBOMACHINES

A.   3D FLOW AND DESIGN METHODS IN HIGHLY-LOADED TURBOMACHINES

Considerable progress has been made in the development of a blade design technique for a 3D highly-loaded cascade subjected to sheared inlet flow. The goal is an a priori blade design allowing for the effects of secondary flow. To date the treatment is limited to inviscid, incompressible flow in the limit of very thin blades.

The method used combines the best features of two alternative 3D rotational flow descriptions: the "two-stream function" description, and the Clebsch transformation technique. (In the former, the constants of the motion are displayed best; in the latter, many of the field equations are more convenient.) The requirement that the two descriptions yield identical results provides useful computational information.

In both descriptions, the "smoothing technique" (4.1),(4.2), developed under this contract, is applied for cascades of large blade numbers (small spacing). The result is a neat, closed theory (4.3) which allows us to determine cascade blade shapes required to produce a specified result in terms of cascade performance at high loading. Numerical examples are being prepared to illustrate "good" and "bad" cases. A computer graphics presentation is being developed to display the flow and blade results in a manner to make them more understandable.

The method developed can also be used for analysis (performance) calculations.

B. NUMERICAL STUDIES OF SECONDARY FLOW IN A BEND USING SPECTRAL METHODS

Introduction

Two items will be described in this progress report: (1) the computer

code for the simulation of viscous flow in a bend of rectangular cross-

section using a mixed spectral finite-difference scheme; and (2) the formu-

lation of spectral element technique for the solution of the Navier-Stokes

equation in the bend with three elements: namely, an upstream element, a

bend element, and a downstream element.

(1) Mixed spectral finite difference code for viscous flow in a bend of

rectangular cross-section

This code has been designed in modular form. Each module performs a

particular task or computes a desired quantity. The strategy followed is

that we first compute a basic flow with $V_{or} = 0$, $V_{o\theta} = V_{o\theta}(r,z)$,

$V_{oz} = 0$ satisfying the non-slip boundary condition at the inner wall $r =$

r_i and the outer wall $r = r_o$ as well as the continuity and momentum

equations. This basic flow $V_o(r,z)$ is time-independent. The time

dependent part and the three-dimensional part are contained in v so that

the resulting velocity field is described by $V = V_o(r,z) + v(r,\theta,z,t)$.

Likewise, the pressure field may be similarly described. This is done for

convenience and is a procedure commonly used by research workers who

simulate turbulence and investigate transitional phenomena in fluid flows

(Refs. 4.4 and 4.5). Note that no approximation is implied by such a

description. Because we have assumed the flow to be incompressible,

therefore a staggered finite difference grid system has to be used in the direction of the bend so that the continuity condition can be satisfied in consistence with the pressure field. Thus we would compute the tangential velocity v_θ at points $j_s = 0,1,2,...J$ (the point $j_s = 0$ would correspond to the inflow boundary while the point $j_s = J$ corresponds to the outflow boundary). However, for consistency we would compute the velocity components v_r, v_z, and the total pressure field p_t at the finite difference grid points j lying halfway between two consecutive j_s.

The code consists of two essential parts:

(A) The preprocessing stage. Here the resolution of the simulation, the geometrical parameters (i.e., the extent of the bend, the inner and outer radii measured in units of half the bend height), the Reynolds number, the inlet shear profile and the time step sizes are chosen. The main program PREPRO3 would call on:

(i)   BASIC to compute the basic flow.

(ii)   PREPRO to preprocess the first fractional step (the non-linear convective step) by performing a LU decomposition of the tridiagonal matrix operator for advancing each of the velocity components forward in time.

(iii) PSNPRS to do the preprocessing necessary for the implementation of the Poisson solver for the intermediate pressure field p_t in the pressure correction step. To achieve this, PSNPRS would in turn call on:

   (a) PMEV to diagonalise the pressure Poisson operator in the θ-direction (i.e., the bend direction) with Dirichlet boundary condition

at $\theta = 0$ and the boundary condition pertaining to the second derivative with respect to θ at $\theta = \theta_o$.

(b) ZNEV to diagonalise the pressure Poisson operator in the z-direction with Neumann boundary conditions at $z = \pm 1$.

(c) COLRTH to compute the radial collocation operator resulting from completion of (a) and (b) above. It is subsequently diagonalised incorporating the Neumann boundary condition at $r = r_i$ and $r = r_o$.

(iv) PSNVEL to perform the preprocessing necessary for the Poisson solvers that implement the viscous correction step. This PSNVEL would in turn call on:

(a) PMEVEL to diagnonalise the velocity Poisson operator in the θ-direction with Dirichlet boundary condition at $\theta = 0$ (inflow boundary) and Neumann boundary condition at $\theta = \theta_o$ (outflow boundary).

(b) ZNEVEL to diagonalise the velocity Poisson operator in the z-direction with Dirichlet boundary conditions at the walls $z = \pm 1$.

(c) COLRVR to compute the radial collocation operator that results from the completion of (a) and (b) above for the radial velocity.

(d) COLRVT to compute the radial collocation operator that results from the completion of (a) and (b) above for the tangential velocity.

(e) COLRVZ to compute the radial collocation operator that results from the completion of (a) and (b) above for the axial velocity.

The collocation operators of (c), (d) and (e) are each subsequently diagonalised incorporating the Dirichlet boundary condition at the walls

$r = r_i$ and $r = r_o$. Note that (c), (d) and (e) have to be done separately because the radial part of the Poisson operators for the radial, the tangential and the axial velocities are different due to the curvature term in the equation of motion.

The results from this preprocessing stage are stored in data files for use in the simulation stage to be described next.

(B) <u>Simulation Stage</u>. The main program BEND would call on:

(i)   DATAIN to read in data (including the initial condition on velocity field) in files created during the preprocessing stage into the core memory.

(ii)   EULER which uses a simple Euler time-stepping scheme (the time-step size for this step is much smaller compared to that specified for the fractional stepping) to establish the values of velocity at two initial time levels necessary for starting the fractional time stepping of the Navier-Stokes equation. It also establishes the initial vorticity field and the initial M-vector ($= V \times \nabla \times V$) field.

(iii)   PRESRE computes the intermediate pressure field p_t that imposes the continuity condition.

(iv)   VISCOS implements the viscous correction step that imposes the non-slip boundary conditions at the walls.

(v)   MOVVEL to keep two time levels of velocity components at any instant. This is necessary for the two-time-level scheme used here as well as for checking the approach to steady state solution if it exists.

(vi)   VOTICY to compute the vorticity field in the flow.

(vii)   MOVMVT to keep two time levels of M-vector at any instance as

required by a two-time-level scheme.

(viii) MVECTR to compute the latest value of M-vector field.

(ix)   DV1NTN to compute the tangential derivative of the velocity compon-
       ents which will be used by SOURC1 to calculate the RHS vector of the
       operator equation that implements the convective step. The sub-
       routine module MOVDTN would perform a similar function to MOVVEL and
       MOVMVT by keeping two time levels of the tangential derivative of
       velocity components at any one instant.

(x)   (a) CONVEC to implement the nonlinear convective step.

       (b) PRESRE to implement the pressure correction step.

       (c) VISCOS to implement the viscous correction step.

The PRESRE would call on PRSSLN which would in turn invoke BDYPSR,
PSPHIZ, PSTMTN and SOLPSN for the solution at the pressure step.

Similarly, VISCOS would call on:

(a)   VRDSLN which would in turn invoke BDYVRD, VRPHIZ, VRTMIN and SOLVRD
       to obtain the radial velocity field.

(b)   VTDSLN which would in turn invoke BDYVTN, VTPHIZ, VTTMTN and SOLVTN
       to obtain the tangential velocity field.

(c)   VZDSLN which would in turn invoke BDYVZ, VZPHIZ, VZTMTN and SOLVZ to
       obtain the axial velocity field.

Note that the tangential velocity corresponds to the velocity in the
direction of the bend while the radial and axial velocity constitute the
flow on the cross-sectional plane of the bend. Steps (v) to (x) would be
repeated for advancing the flow forward in time.

At the moment, the subroutine module PRESRE (for the pressure

correction step) has not been performing well in terms of accuracy as one
would expect. Currently work is directed at ascertaining the cause for the
loss in accuracy in PRESRE and a way of correcting that.

The inflow boundary conditions are specified while the outflow
boundary conditions assume either the first derivative or the second
derivative in the tangential direction vanishes.

(2) Formulation of Spectral Element Method

Work has begun on the formulation of spectral element technique for
the simulation of three-dimensional viscous flow. The formulation
described here was carried out while this co-investigator was at Whittle
Laboratory for a period of 5 weeks. For the flow in a bend, three macro-
elements are used: the element upstream of the bend, the bend element, and
the element downstream of the bend. Flow variables are expanded in a
triple Chebyshev series (i.e., the Chebyshev series is used as a high order
Lagrangian interpolant). Unwanted high resolution at the inflow and
outflow boundaries are eliminated via the introduction of multiple elements
in the flow direction. A Cartesian co-ordinate system is used in the
upstream and the downstream element while a cylindrical co-ordinate system
is used in the bend element. Initial effort is focused on the solution of
Poisson and Helmholtz equations (as required for the pressure and viscous
steps in the solution of Navier-Stokes equation) in the multielements
domain. Each elemental domain is transformed to a standard domain in which
the boundaries of the domain are at -1 or +1. Diagonalisation of the
Poisson and the Helmholtz operators is performed in two orthogonal
directions on the cross-sectional plane. This reduces the original three-

dimensional equation into a one-dimensional one in the direction of the bend. A variational principle in the bend-direction (or θ-direction) is then invoked for building the elemental matrices. These elemental matrices are then synthesized into a global matrix that satisfies the specified inflow and outflow boundary conditions and preserves the continuity of function at the elemental interfaces. It is hoped that in the future we would be able to continue on this work so that an executable formulation and analysis could be used to simulate viscous internal flow.

C. THREE-DIMENSIONAL BLADE DESIGN FOR LARGE DEFLECTION

Since publishing the work on the Cambridge design method (reference 4.7), we can report some progress both on the application of the method and on its improvement. The method has been applied in a simpler, but the same fundamental, form to the design of a radial flow turbine by an industrial firm. The results were very encouraging. Work is in progress on the preparation of more rigorous methods for design in turbomachines of arbitrary geometry, but with restriction to incompressible, irrotational flow through the blades.

In our solution method (reference 4.8) we have divided the flow velocity into a mean velocity, averaged in the pitchwise or tangential direction, and a periodic velocity. This periodic velocity is then expressed as a Fourier series in the θ or tangential direction. In the computation, the Fourier series was truncated after some fifteen terms. The errors due to this truncation have been examined for the two-dimensional cascade and found to arise from a term in the Fourier series which varies as $1/n^2$ where n is the harmonic. This term has been identified and a relatively simple method of correcting the largest part of the truncation error is now proposed. When applied to the two-dimensional cascade for which the Biot Savart method gives the result of taking an infinite number of terms, it is found that using 10 terms plus the truncation error correction gives a more accurate answer than using 60 terms without truncation error correction. The method has been extended to the full three-dimensional case and similar results have been obtained. A report is in preparation.

Some numerical work has been done to examine in detail the blade

shapes obtained at and near the wall. It has been found that the behavior of the inclination of the blade surface to the radial direction is singular owing to its reflection in the wall.

Some progress has also been made on the analytical part of this work. In particular, a theoretical expression was obtained for the pressure jump (or more appropriately the enthalpy jump in the case of irrotational compressible flow) across a blade of finite thickness represented by two vortex sheets (fig. 1): one pertains to the suction surface defined by $\alpha^- = \theta - f^-(r,z) =$ constant while the other pertains to the pressure surface defined by $\alpha^+ = \theta - f^+(r,z) =$ constant. With the thickness angle of the blade given by $\tau = \alpha^+ - \alpha^- = f^- - f^+$, the enthalpy jump $(h^+ - h^-)$ across the blade is derived as

$$h^+ - h^- = \frac{2\pi}{B} \; \frac{1}{2} \, (\underline{W}^+ + \underline{W}^-) \cdot \nabla r\overline{V}_0 + \frac{1}{2} \; \frac{\nabla\alpha^+ \cdot \nabla(r\overline{V}_\theta)^+}{|\nabla\alpha^+|^2} \, \underline{W}^-$$

$$+ \; \frac{\nabla\alpha^- \cdot \nabla(r\overline{V}_\theta)^-}{|\nabla\alpha^-|^2} \, \underline{W}^+ \; \cdot \; \nabla\tau \tag{1}$$

where B is the number of blades, $\underline{W}$ is the relative velocity as seen from a frame fixed to the blade row and $r\overline{V}_\theta = (r\overline{V}_\theta)^+ + (r\overline{V}_\theta)^-$. The $(r\overline{V}_\theta)^\pm$ are related to the $W^\pm$ and $\alpha^\pm$ as follows:

$$\underline{W}^+ = \frac{2\pi}{B} \; \frac{\nabla\alpha^+ \cdot \nabla(r\overline{V}_\theta)^+}{|\nabla\alpha^+|^2} \, \nabla\alpha^+ - \nabla(r\overline{V}_\theta)^+ \tag{2a}$$

and

$$-\underset{\sim}{W}^- = \frac{2\pi}{B} \frac{\nabla\alpha^- \cdot \nabla(r\bar{V}_\theta)^-}{|\nabla\alpha^-|^2} \nabla\alpha^- - \nabla(r\bar{V}_\theta)^- \tag{2b}$$

(see Ref. 4.4)

It should be pointed out that the expression given in Eq. (1) does not pertain to a point but rather to a fixed z on the r-θ plane (here we have assumed that a right-handed cylindrical co-ordinate system is used). By letting τ→0, we obtain the limit of infinitely thin blades where the enthalpy jump $(h^+ - h^-)$ across the blade is given by

$$(h^+ - h^-) = \frac{2\pi}{B} \underset{\sim}{W}_{bl} \cdot \nabla r\bar{V}_\theta \tag{3}$$

where $W_{bl} = 1/2(W^+ + W^-)$. This agrees with the result obtained in Ref. 4.4. Following this, we can thus argue that the second term in the expression in Eq. (1) is a correction term due to the fact that the blade has a finite thickness. At this stage, we have not as yet adressed in rigor the question of whether Eq. (1) is valid when the flow upstream of the blade row is rotational. It should be kept in mind that the above results have been arrived at based on the assumptions that the flow is inviscid, homentropic and the rothalpy is uniform far upstream.

From the above analytical results, one would notice the slight increase in complexity with the introduction of thickness into the blade. In the case of infinitely thin blades, specification of the swirl schedule $(r\bar{V}_\theta)$ in the blade region is sufficient for the determination of the blade shape. However, for the case of blades with finite thickness, specification of only one of $(r\bar{V}_\theta)$, $(r\bar{V}_\theta)^+$ or $(r\bar{V}_\theta)^-$ is not sufficient. Some exploration

of the possibilities has been done for the example of two-dimensional cascades. Strut profiles have been computed using the Biot Savart method and various distributions of $(r\overline{V}_\theta)^+$ (note for the case of the strut $(r\overline{V}_\theta)^+ = (r\overline{V}_\theta)^-$). For cambered blades it may be better to specify $r\overline{V}_\theta$ and τ. For instance, one could conceive of the design calculation as follows:

(1) Specify $r\overline{V}_\theta [=(r\overline{V}_\theta)^+ + (r\overline{V}_\theta)^-]$ and the thickness angle τ

(2) Guess an initial α^- (hence α^+)

(3) Determine $(r\overline{V}_\theta)^-$ (hence $(r\overline{V}_\theta)^+$) approximately from Eq. (2b) assuming a value of W^- from an approximate mean flow calculation

(4 Compute the flow field with the knowledge of α^+, α^-, $(r\overline{V}_\theta)^+$ and $(r\overline{V}_\theta)^-$

(5) Update α^- using the boundary condition on the suction surface that $W^- \cdot \nabla \alpha^- = 0$

(6) Update $(r\overline{V}_\theta)^+$ using Eq. (2a) hence $(r\overline{V}_\theta)^-$ or $W^+ \cdot \nabla \alpha^+ = 0$

(7) Repeat steps (3) to (6) until convergence is obtained

Notice that in the above procedure, we have allowed $(r\overline{V}_\theta)^+$ and $(r\overline{V}_\theta)^-$ to float in such a way that their sum agrees with the specified $(r\overline{V}_\theta)$. A different procedure from the above could have been followed by specifying $(r\overline{V}_\theta)^-$ and τ but allowing $(r\overline{V}_\theta)$ and $(r\overline{V}_\theta)^+$ to float such that their difference is $(r\overline{V}_\theta)^-$. Alternatively, there may be the possibility of specifying the enthalpy distribution and thickness angle τ. We believe these many design procedures could be arrived at using the above analytical results. We have not examined in detail the implications of devising such a design procedure.

No effort has been expended on developing numerical techniques and designing a computer code to implement any numerical calculations based on the above extension of the theory.

References:

4.1 McCune, J.E., and Dang, T.Q., "Periodic Internal Flows," presented at the Symposium on "Computation of Internal Flows: Methods and Applications," February 11-17, 1984, New Orleans.

4.2 Dang, T.Q., and McCune, J.E., "Design Method for Highly-Loaded Blades with Blockage in Cascade," presented at the Symposium on "Computation of Internal Flows: Methods and Applications," February 11-17, 1984, New Orleans.

4.3 Dang, T.Q., and McCune, J.E., "A 3D Blade Design Method in Rotational Flow," to be presented at the "International Conference on Inverse Design Concepts in Engineering Sciences (ICIDES)," October 17-18, 1984, University of Texas at Austin.

4.4 S. Orszag and L. Kells, "Transition to turbulence in plane poiseuille and plane couette flow," JFM (1980), Vol. 96, Pt. 1.

4.5 A. Patera and S. Orszag, "Finite-amplitude stability of axisymmetric pipe flow," JFM (1981), Vol. 112.

4.6 Previous Multi-Investigator Progress Reports.

4.7 C.S. Tan, et al., "Three-dimensional blade design for large deflections using an analytical theory," GTL Report No. 118, and CUED/A-Turbo/TR115, 1982.

4.8 Hawthorne, W.R., Tan, C.S., et al., "Theory of Blade Design for Large Deflections, Part I - Two-Dimensional Cascades, and Part II - Annular Cascades," ASME J. Eng. for Gas Turbines and Power, 106, pp. 346-365, April 1984.

GENERAL PROGRESS ON AFRAPT

The Air Force OSR sponsored educational program, called Air Force
Research in Aeronautical Propulsion Technology (AFRAPT), steering
committee consists of:

Dr. Michael Salkind	AFOSR, Chairman
Mr. Walter Schrader	AVCO Lycoming
Dr. Lynn Snyder	DDA
Mr. Elmer Wheeler	Garrett Aerospace Corp.
Dr. Fred Erich	GE Lynn
Dr. David Wisler	GE Evendale
Mr. Tom Hampton	Pratt & Whitney (GPD)
Professor Sandford Fleeter	Purdue University
Professor Peter Jenkins	Texas A&M University

and

Professor Eugene E. Covert	Massachusetts Institute of Technology, Secretary

In the past year this group has met twice. The annual brochure has
been prepared and is being distributed. The primary business is that of
trying to establish procedures to meet the needs and schedules of all
participants.

The Steering Committee has met, reviewed the program and accepted
modified procedures with the goal of balancing the number of vacancies in
the program between the industry and the university.

3. PUBLICATIONS

Cheng, P., Prell, M.E., Greitzer, E.M., Tan, C.S., "Effects of Compressor Hub Treatment on Stator Stall and Pressure Rise," J. Aircraft, 21, pp. 469-475, July 1984.

Hawthorne, W.R., Wang, C., Tan, C.S., and McCune, J.E., "Theory of Blade Design for Large Deflections, Part I: Two-Dimensional Cascades," ASME Journal for Engineering for Power, 106, pp. 346-354, April 1984.

Tan, C.S., Hawthorne, W.R. McCune, J.E., and Wang, C., "Theory of Blade Design for Large Deflections, Part II: Annular Cascades," ASME Journal for Engineering for Power, 106, pp. 354-366, April 1984.

Liu, W., Greitzer, E.M., and Tan, C.S., "Surface Static Pressures in an Inlet Vortex Flow Field," (presented at 1984 ASME Gas Turbine Conference), to be published in ASME J. Engineering for Power.

Ng, W.F., and Epstein, A.H., "High Frequency Temperature Probe for Unsteady Compressible Flows," Review of Scientific Instruments, 54, pp. 1678-1683, December 1983.

Ng, W.F. and Epstein, A.H., "Unsteady Losses in Transonic Compressors," (presented at 1984 ASME Gas Turbine Conference), accepted for publication in ASME J. Engineering for Power.

Tan, C.S. and Greitzer, E.M., "Non-Axisymmetric Compressible Swirling Flow in Turbomachine Annuli," to be submitted to AIAA Journal.

4. PROGRAM PERSONNEL

Principal Investigators:

Jack L. Kerrebrock
R.C. Maclaurin Professor
and Department Head
Aeronautics and Astronautics

Edward M. Greitzer
Professor of Aeronautics and Astronautics
Director, Gas Turbine Laboratory

William T. Thompkins, Jr.
Associate Professor of Aeronautics and Astronautics

James E. McCune
Professor of Aeronautics and Astronautics

Co-Investigators:

Alan H. Epstein
Associate Professor of Aeronautics and Astronautics
Associate Director, Gas Turbine & Plasma Dynamics Laboratory

Choon S. Tan
Research Associate

Collaborating Investigators:

Eugene E. Covert
Professor of Aeronautics and Astronautics
Director, Center for Aerodynamic Studies

Sir William R. Hawthorne
Senior Lecturer

Wai K. Cheng
Soderberg Assistant Professor of Mechanical Engineering

Hyoun-Woo Shin
Post-Doctoral Associate

Robert Haimes
Research Associate

Current Graduate Research Assistants:

9/83 - Present	Mark Johnson (AFRAPT Student)
9/81 - Present	Thong Dang*
9/80 - 12/83	Wing-Fai Ng**
9/83 - Present	Petros Kotidis
9/82 - 3/84	Cheryl Shippee*
9/82 - 12/83nt	Gilles Thevenet*
9/79 - 6/84	Siu Shing Tong**

* S.M. Degree Completed
**Ph.D Thesis Completed

5. INTERACTIONS

Presentations

E.M. Greitzer, "Mechanisms of Inlet Vortex Formation," Cambridge University, November 1983, and British Aerospace Corporation, February 1984.

E.M. Greitzer, "The Stability of Pumping Systems," Rolls-Royce Limited, Derby, England, December 1983.

E.M. Greitzer, "Stability Enhancement Using Casing/Hub Treatment," Cambridge University, December 1983.

E.M. Greitzer, "Introduction to Unsteady Flows in Turbomahcines" and "Flow Instabilities in Turbomachines and Gas Turbine Engines," lectures presented at Von Karman Institute, course on Unsteady Flows in Turbo- machines, February 1984.

E.M. Greitzer, "MIT Research on Stall Recovery," a progress report pre- sented to Pratt & Whitney Aircraft, Government Products Division, March 1984.

C.S. Tan, "Spectral Method Computations of Internal Flows," Cambridge University, April 1984.

Dang, T.Q. and McCune, J.E., "Periodic Internal Flows," presented at ASME Symposium on "Computation of Internal Flows: Methods and Applications," Feb. 11-17, 1984, New Orleans.

Dang, T.Q., McCune, J.E., "Design Method for Highly-Loaded Blades with Blockage in Cascade," presented at ASME Symposium on "Computation of Internal Flows: Methods and Applications," Feb. 11-17, 1984.

As described in previous reports, there are strong interactions between the Gas Turbine Laboratory and the aircraft engine industry, as well as Air Force and other government laboratories. We also have an active seminar program to bring speakers from industry and/or government to MIT. During the past six months these have included:

Dr. Robert Dring, Manager, Gas Turbine Technology,
United Technologies Research Center,
"An Overview of Axial Compressor Aerodynamics"

Mr. Michael Pierzga, Research Engineer
U.S. Army Propulsion Laboratory
"Investigation of the Three-Dimensional Flow Field Within a
Transonic Fan Rotor - Experiment and Analysis"

Dr. S. Srinivasan, Manager of Applied Mechanics Research
United Technologies Research Center
"Aerodynamically Excited Vibrations of a Part Span Shrouded Fan"

Dr. Arthur J. Wennerstrom
Air Force Aeropropulsion Laboratory
"Design Techniques for High Performance Fans and Compressors"

6.   DISCOVERIES, INVENTIONS, AND SCIENTIFIC APPLICATIONS

During the present contract period, there have been no inventions.

7. CONCLUSIONS

As we have stated previously, although the emphasis in work done varies from project to project, we do appear to be making continued progress in all of the efforts. One further aspect deserves mention. This past year we had our first AFRAPT student, Mr. M. Johnson. Our involvement in the program has now expanded and Mr. D. Fink (associated with General Electric) and Ms. J. Koo (AVCO), who are currently students at MIT, will also be starting in this program this summer.

END

FILMED

11-84

DTIC